Bioinspired Structure Tailoring of Tin Oxide based Materials for high Capacity Electrodes

Von der Fakultät Chemie der Universität Stuttgart
zur Erlangung der Würde eines Doktors der
Naturwissenschaft (Dr. rer. nat) genehmigte Abhandlung

vorgelegt von

Timotheus Hieronymus Jahnke
aus Herdecke

Hauptberichter:	Prof. Dr. Joachim Bill
Mitberichter:	Prof. Dr. Siegfried Schmauder
Prüfungsvorsitzender:	Prof. Dr. Thomas Schleid
Tag der mündlichen Prüfung:	23.07.2021

Universität Stuttgart

Institut für Materialwissenschaft der Universität Stuttgart
2021

To Agnese, Alexander and Isabel

Outline

Declaration of Authorship i
Publication of Individual Chapters in Scientific Journals iii
Further Non-related Publications v
List of Abbreviations and Symbols vii
1. Introduction 1
1.1 Lithium Ion Batteries 1
1.1.1 Free-Standing and flexible electrodes 13
1.2 Multivalent Ion Batteries 15
1.3 Bioinspired assembly and structuring techniques 19
1.3.1 Nacre 20
1.3.2 Calcareous Sponges – Clathrina Clathrus 23
1.3.3. Ice-templating technique 25
1.4 Relevance and outcome of this thesis 29
1.5 Discussion 31
1.5.1 Tailoring the morphology and structure of the active material 33
1.5.2 Embedding the active material into a graphene-based 2D structure for Lithium-Ion-Batteries 35
1.5.3 Embedding the active material into a 3D ultra-porous foam structure for Aluminium Ion Batteries 38
1.5.4 Outlook 41
1.6 References 43
2. Bioinspired Synthesis of SnO Crosses as Backbone in Artificial Sponges 57
2.1 Introduction 57
2.2 Controlling the Hydrothermal Synthesis 60
2.3 Ice-templating Artificial Sponges 67
2.4 Conclusion 68
2.5 Experimental Set-up 69
2.6 Acknowledgements 70
2.7 References 70
2.8 Supporting Information 73
3. Coalescence in Hybrid Materials – The Key to High Capacity Electrodes 78
3.1 Introduction 79
3.2 Results & Discussion 81

3.3 Conclusions 90
3.4 Materials and Methods 91
3.5 Acknowledgments 93
3.6 References 93
3.7 Supporting Information 97
4. Highly Porous Free-standing rGO/SnO_2 Pseudocapacitive Cathodes for High-Rate and Long-Cycling Al-Ion Batteries 103
4.1 Introduction 104
4.2 Materials and Methods 106
4.3 Results and Discussion 108
4.4 Conclusion 120
4.5 Acknowledgments 121
4.6 References 121
4.7 Supplementary Materials 125
Summary 134
Zusammenfassung 135
Danksagung 137

Declaration of Authorship

I hereby certify that the dissertation entitled

“Bioinspired Structure Tailoring of Tin Oxide based Materials for High Capacity Electrodes”

is entirely my own work except where otherwise indicated. Passages and ideas from other sources have been clearly indicated and referenced.

Name _____

Signature _____

Date _____

Publication of Individual Chapters in Scientific Journals

The present thesis has a cumulative structure. The chapters are the following three papers which have been published in scientific journals:

Chapter 2: Bioinspired Synthesis of SnO Crosses as Backbone in Artificial Sponges

Jahnke, Timotheus; Kilper, Stefan; Knöller, Andrea; Brümmer, Franz; Widenmeyer, Marc; Rothenstein, Dirk; Burghard, Zaklina; Bill, Joachim. (2019), Phil. Trans. R. Soc. A 377: 20190130. DOI: 10.1098/rsta.2019.0130

(Conceptualization, T.J., Z.B. and S.K.; validation, T.J., S.K., M.W., Z.B. and D.R.; methodology, T.J., S.K. and Z.B.; investigation, T.J. and M.W.; original draft preparation, T.J.; manuscript editing, T.J., A.K., Z.B., M.W., F.B. and J.B.; supervision, J.B., Z.B. and D.R.; project administration, S.K. and T.J.; funding acquisition, S.K. and T.J.)

Chapter 3: Coalescence in Hybrid Materials: The Key to High-Capacity Electrodes

Jahnke, Timotheus; Knöller, Andrea; Kilper, Stefan; Rothenstein, Dirk; Widenmeyer, Marc; Burghard, Zaklina; Bill, Joachim. (2018), ACS Applied Energy Materials *1* (12), 7085-7092, DOI: 10.1021/acsaem.8b01495

(Conceptualization, T.J., A.K. and Z.B.; validation, T.J., M.W., Z.B. and D.R.; methodology, T.J., A.K. and Z.B.; investigation, T.J.; original draft preparation, T.J.; manuscript editing, T.J., A.K., Z.B., M.W., S.K. D.R. and J.B.; supervision, J.B., Z.B; project administration, Z.B.)

Chapter 4: Highly Porous Free-standing rGO/SnO_2 Pseudocapacitive Cathodes for High-Rate and Long-Cycling Al-Ion Batteries

Jahnke, Timotheus; Raafat, Leila; Knöller, Andrea; Hotz, Daniel; Diem, Achim Max; Bill, Joachim; Burghard, Zaklina. (2020). Nanomaterials 10, 10, DOI: 10.3390/nano10102024

(Conceptualization, T.J, Z.B. L.R..; methodology, T.J.; investigation, T.J., D.H.; writing—original draft preparation, T.J.; writing—review and editing T.J., A.K., L.R., Z.B. A.D.; supervision, Z.B. J.B.)

Further Non-related Publications

Kilper, Stefan; Jahnke, Timotheus; Wiegers, Katharina; Grohe, Vera; Burghard, Zaklina; Bill, Joachim; Rothenstein, Dirk. (2019). *Peptide Controlled Shaping of Biomineralized Tin(II) Oxide into Flower-Like Particles*. Materials. 12. 904. DOI: 10.3390/ma12060904.

Kilper, Stefan; Jahnke, Timotheus; Aulich, Marc; Burghard, Zaklina; Rothenstein, Dirk; Bill, Joachim. (2019). *Genetically Induced In Situ-Poling for Piezo-Active Biohybrid Nanowires.* Advanced Materials. 31. 1805597. DOI:10.1002/adma.201805597.

Singh, Ajay; Jahnke, Timotheus; Wang, Shuo; Xiao, Yang; Alapan, Yunus; Kharratian, Soheila; Onbasli, M; Kozielski, Kristen; David, Hilda; Richter, Gunther; Bill, Joachim; Laux, Peter; Luch, Andreas; Sitti, Metin. (2018). *Anisotropic Gold Nanostructures: Optimization via In-Silico Modeling for Hyperthermia.* ACS Applied Nano Materials. 1. DOI: 10.1021/acsanm.8b01406.

Singh, Ajay; Alapan, Yunus; Jahnke, Timotheus; Laux, Peter; Luch, Andreas; Aghkahani, Amirreza; Kharratian, Soheila; Onbasli, M; Bill, Joachim; Sitti, Metin. (2018). *Seed-mediated synthesis of plasmonic gold nanoribbons using cancer cells for hyperthermia applications.* Journal of Materials Chemistry B. 6. DOI: 10.1039/C8TB02239A.

Qawasmi, Yara; Atanasova, Petia; Jahnke, Timotheus; Burghard, Z; Müller, A; Grassberger, L; Strey, Reinhard; Bill, Joachim; Sottmann, Thomas. (2018). *Synthesis of nanoporous organic/inorganic hybrid materials with adjustable pore size.* Colloid and Polymer Science. 296. DOI: 10.1007/s00396-018-4402-z.

Singh, Ajay; Gemmati, Donato; Kanase, Anurag; Pandey, Ishan; Misra, Vatsala; Kishore, Vimal; Jahnke, Timotheus; Bill, Joachim; (2018). *Nanobiomaterials for vascular biology and wound management: A review.* Veins and Lymphatics. 7. DOI: 10.4081/vl.2018.7196.

Singh, Ajay; Jahnke, Timotheus; Kishore, Vimal; Park, Byung-Wook; Batuwangala, Madu; Bill, Joachim; Sitti, Metin. (2018). *Cancer cells biomineralize ionic gold into nanoparticles-microplates via secreting defense proteins with specific gold-binding peptides*. Acta Biomaterialia. 71. DOI: 10.1016/j.actbio.2018.02.022.

Raafat, Leila; Wicklein, Bernd; Majer, Günter; Jahnke, Timotheus; Diem, Achim M.; Bill, Joachim; Burghard, Zaklina. (2020). *Shape-conformable, Eco-Friendly Cellulose Aerogels as High-Performance Battery Separators*, ACS Applied Energy Materials, DOI: 10.1021/acsaem.0c02612

Spatz, Joachim; Micoulet, Alexandre; Hackner, Maximilian; Burghard, Zaklina; Jahnke, Timotheus. A network of metal fibers, method for producing a network of metal fibers, a resulting electrode and battery, EPA, WO2020016240

List of Abbreviations and Symbols

AFM	Atomic force microscopy
AIB	Aluminium Ion Batteries
BET	Brunauer-Emmett-Teller
$CaCO_3$	Calcium carbonate
CV	Cyclic voltammetry
CMC	Carboxymethyl cellulose
EC:DMC	Ethylene carbonate/ Dimethyl carbonate
EDX	Energy dispersive x-ray spectroscopy
EES	Electrical energy storage
EIS	Electrical impedance spectroscopy
FTIR	Fourier-Transform infrared spectroscopy
FWHM	Full Width at half maximum
GO	Graphene oxide
HBr	Hydrobromic acid
ICP-OES	Inductive coupled plasma – optical emission spectroscopy
LIB	Lithium Ion Battery
NMC	Lithium nickel manganese oxide
PVP	Polyvinylpyrrolidone
PXRD	Powder X-Ray Diffraction
rGO	Reduced Graphene oxide
SEI	Solid electrolyte interface
SEM	Scanning electron microscopy
SHE	Standard Hydrogen electrode
$SnCl_2$	Tin chloride
SnO	Tin oxide
SnO_2	Tin dioxide
TEM	Transmission electron microscopy
TGA	Thermogravimetric analysis
XRD	X-Ray Diffraction
C	Charging rate unit (1 C = applied current to fully charge in 1 h)
θ	Angle between sample lane and incoming x-Ray beam during a XRD or PXRD measurement
P	Porosity
ρ	Density
v	Scanning rate

1. Introduction

1.1 Lithium Ion Batteries

Nowadays, the demand for electrical energy storage (EES) devices has been constantly increasing.[1] Specifically, the automotive industry and other mobile applications require EES systems that provide high energy and power densities.[2,3] As displayed in **Figure 1a**, the required power and capacity of a battery depends on its function, ranging from small scale gadgets, like phones to grid scale energy storage systems. One of the key requirements which all of such systems have in common is the reversible energy storage, i.e. the application of rechargeable batteries.[4] Such batteries are able to undergo charging and discharging with a high efficiency of up to 99 %. The oldest of these electrochemical energy storage systems is the lead acid battery, using Pb and PbO_2 as active materials and sulfuric acid as the electrolyte. Their application as starter-battery in cars is related to their inherent ability to provide high currents for a short time.[5] The nominal cell voltage is around 2 V, however, due to the high density of Pb (11.3 g cm^{-3}) the gravimetric capacity is limited to 30 – 40 mAh g^{-1}. As displayed in **Figure 1b**, the relatively low energy density, their toxicity and large weight, hinders their application as rechargeable energy storage system for mobile applications.

In comparison with lead acid batteries and other rechargeable energy storage systems like Nickel-Cadmium, Nickel-Metal-Hydride batteries or supercapacitor (**Figure 1b**), Lithium Ion Batteries (LIB) are much more suitable for mobile applications, due to their comparatively large energy density of up to 250 W h kg^{-1} and 650 W h L^{-1}, high charging rate of 1 C and expected lifetime of about 5 years.[6,7]

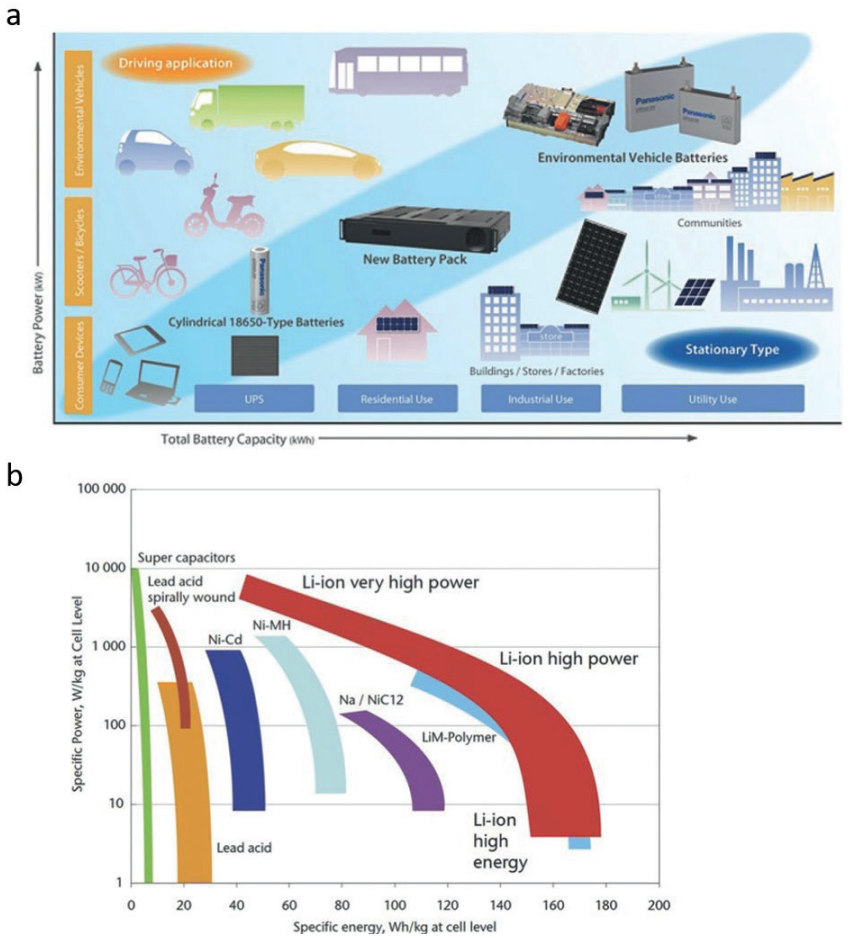

Figure 1. Application requirements for battery of high power and capacity. (b) Comparison of the state-of-the-art energy storage technologies.[8] Reproduced with permission of John Wiley and Sons (© 2015 WILEY-VCH Verlag GmbH & Co. KGaA, Weinheim)

A LIB in general comprises several components contributing to its performance: electrodes (cathode and anode) as well as electrochemically active and inactive components, like the electrolyte and separator, respectively. The lithium-based electrochemical systems are highly favorable, since the involved lithium ions are small and as such can be hosted by various materials, as displayed in **Figure 2**. Furthermore, early research of lithium ion batteries involved the application of metallic lithium as anode material. However, its application was critical due

to the high reactivity of metallic lithium resulting in the formation of dendrites upon electrochemical deposition of Li metal. In order to overcome this limitation, graphite as substitute became a possible candidate, which is evident from its electrochemical performance compared to the state-of-the-art anode materials (**Figure 2a**). Graphite is highly abundant in the earth crust, which leads to a cost-efficient use of the material. From an electrochemical standpoint, graphite allows the intercalation of lithium at a low potential *vs* Li (0.1 V *vs* Li/Li^+) with a theoretical capacity of 372 mAh g^{-1}, as shown and patented in 1985 by Yoshino Akira.[9] The Li^+ ions are thereby intercalated into the graphite, to form lithium graphite (C_6Li) at a fully charged state. The chemically strong bonding between the carbon – carbon atoms provides an excellent reversibility[10] (99 % coulombic efficiency) and life cycle stability[7] (up to 1500 cycles) of graphite as active material. In recent years, researchers have found a large number of additional anode materials, like Sn, Ge, or Si, (see **Figure 2a**) which drawbacks will be discussed in a later section.

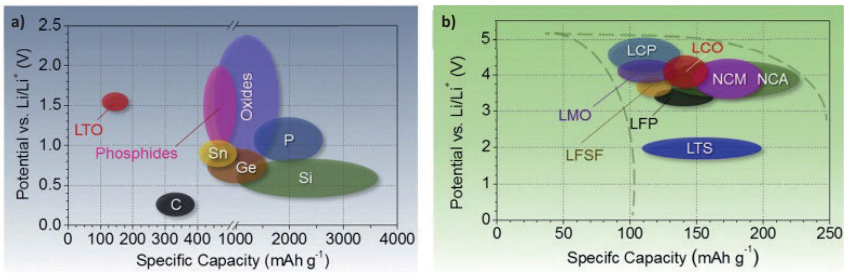

Figure 2. a) different anode materials used in lithium ion batteries at their different specific potential and capacity (LTO stands for lithium titanium oxide) and b) their cathodic counterparts.[11] LMO stands for lithium manganese oxide, LFSF for lithium iron fluorosulfate, LCP for lithium cobalt phosphate, LCO for lithium cobalt oxide, LFP for lithium iron phosphate, LTS for lithium titanium sulphide and NCA for nickel cobalt aluminium oxide. Adapted and reproduced with permission of Elsevier Ltd. (Copyright © 2014 The Authors. Published by Elsevier Ltd.)

On the other hand, a material which displays a high potential *vs* Li/Li^+ is $LiCoO_2$ from a material class called layered metal oxides (see **Figure 2b**). The crystal structure of the $LiCoO_2$ is a layered trigonal structure (Space group $R\bar{3}m$) at temperatures above 750 °C.[12] HR-TEM studies have shown, that the lithium is embedded between CoO_2 slabs, which facilitates ion intercalation and the diffusion in the solid active material.[13] In comparison with the comparatively low temperature configuration (350 °C) of LCO in the cubic spinel structure, the layered trigonal $LiCoO_2$ shows a superior capacity (**Figure 2b**).[12] Therefore it has been widely applied as cathode material in LIBs with a potential of 3.7 V *vs* Li/Li^+ a capacity of 135 - 140 mAh g^{-1}.[12,14] The

Co^{3+}/Co^{4+} redox couple compensates the removal of a Li ion from the layered structure resulting in $Li_{1-x}CoO_2$. Upon removal of more than 50 % of the lithium from the compound, the crystal structure changes irreversibly from the hexagonal to the monoclinic phase, rendering the electrochemical reaction irreversible as well.[12] Currently, researchers are aiming to increase the capacity and electrochemical stability by partially substituting the cobalt with nickel and manganese, allowing for an increase in capacity up to 200 mAh g^{-1}.[12] The resulting material Nickel Cobalt Manganese Oxide (NCM) is nowadays the most used cathode material in LIBs, specifically in hybrid electric vehicles.[15] Both materials, graphite and the corresponding NMC, show an excellent coulombic efficiency of 99 % making their application in LIBs possible. However, with the increasing demand for higher gravimetric and volumetric energy densities, the demand for high capacity electrode materials on the anode side and high voltage active materials on the cathode side is of great importance. Thereby, the currently most promising candidates are on the anode side silicon (due to its high capacity) and tin (due to its relative stability), whereas on the cathode side spinel oxides (*e.g.* $LiNi_{0.5}Mn_{1.5}O_4$) and polyanionic compounds (*e.g.* $LiVPO_4F$) are considered promising to increase the potential of the electrochemical cell.[16]

In general, an active material is usually synthesized in the form of a nano- to micrometer sized powder and for its application as electrode, additives for mechanical stability and electrical conductivity need to be added. Along this line, the active material is mixed in a solvent (water or n-methylpyrrolidone)[15,17] with a polymeric binder, such as polyvinylidenefluoride (PVDF) or Carboxymethylcellulose (CMC) and carbon black (Super P) with the aim to obtain a mechanically stable, porous active material with the required electrical conductivity.[18] The dispersed additives and active material form a slurry, which is coated onto a metallic current collector foil, usually composed of copper on the anode side and aluminum on the cathode side, as displayed in **Figure 3**. A scraper or a doctor blade is used to homogeneously distribute the slurry with a distinct thickness of top of the current collector.

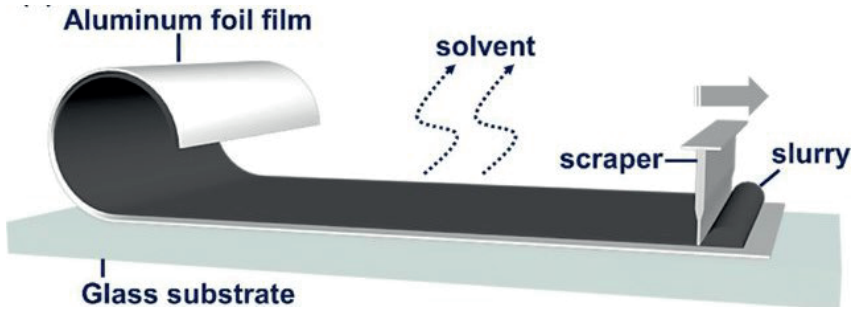

Figure 3. Exemplary fabrication of a state-of-the-art industrial electrode.[19] Adapted and reproduced under the creative commons CC BY licence. (© 2020 Wiley-VCH Verlag GmbH & Co. KGaA, Weinheim)

The obtained active material layer needs to have a porosity of 20 % – 30 %, that allows the required continuous ion transport through the electrode's active material. Specifically, this porosity if required to achieve a high contact area between the electrolyte and the individual active material particles, which enables the ion diffusion. The copper foil on the anode side is used due to the tendency of lithium to form alloys with a large variety of metals at a low potential *vs* Li/Li^+. As counter electrode current collector metallic aluminum foil is used, which is highly stable against the large voltage present on the cathode side (up to 4.3 V for NMC) in lithium ion batteries. Hereby, the formation of both Al_2O_3 and AlF_3 when in contact with the electrolyte and during the first cycles, protects the surface of the aluminum current collector foil, leading to stability of the foil up to 5 V.[20]

The electrolyte is usually a solution of a lithium salt (*e.g.* $LiPF_6$) in compatible solvents, such as ethylene- and dimethyl-, diethyl- and ethylmethylcarbonates or mixtures of these. These alkyl carbonates have a high stability against the large voltages present in lithium ion cells and show little decomposition upon the reversible charging/discharging processes.[21] They provide a sufficiently high diffusivity of 0.7 to 2.2 * 10^{-10} m^2 s at a temperature of 20 °C for the lithium ions and guarantee the long range lithium ion transport through the whole cell, that is the separator and the different active material layers.[22]

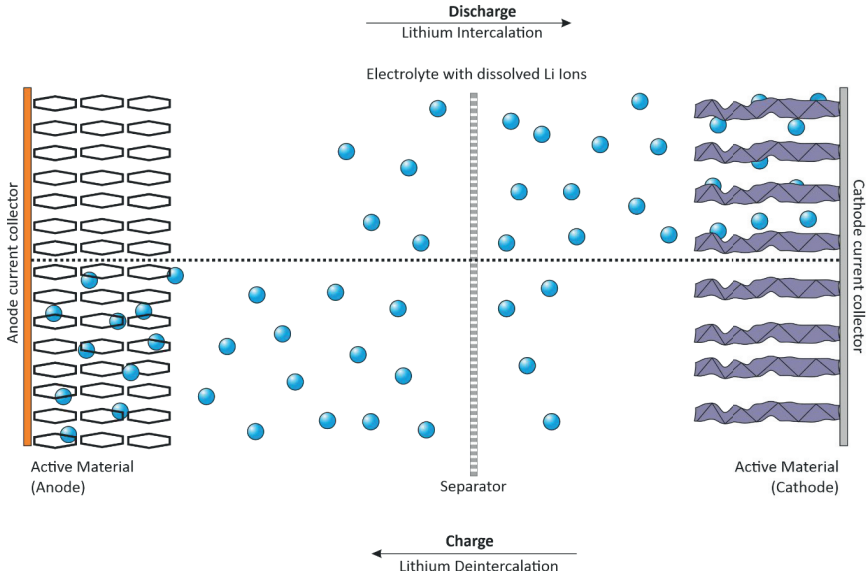

Figure 4. A schematic description of a lithium ion cell. Upon charging the cell, the lithium ions are intercalated into the anode structure and deintercalated from the cathode structure. The honeycomb structure of the graphite and the trigonal structure of the layered metal oxide is exemplary shown.

During the charging process, lithium ions are deintercalated from an active material (cathode) and diffuse inside the electrolyte through the separator towards the opposing active material (anode), where they are intercalated (schematically presented in **Figure 4**). Upon discharging, this process is reversed. The number of lithium ions, which can be stored in the active material determines the energy density of the electrodes, whereas the speed, at which intercalation and deintercalation occurs, correlates with the power density. Enabling the alteration of the charging/discharging speed, is a promising approach to enhance the deliverable power density, and has been therefore of great interest to researchers in recent years.[23]

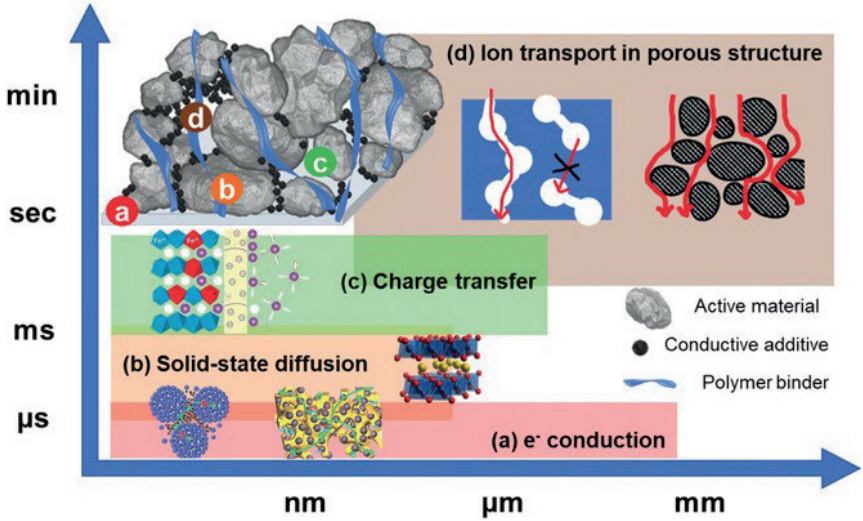

Figure 5. Effects and processes governing the energy storage in a lithium ion battery. In detail, both electronic conductivity (a) and charge transfer (c) from the Li ion need to be large enough for the intercalation reaction to function. Additionally, a sufficient supply of lithium ions needs to be present, in the solid active material (b) as well as the liquid electrolyte (d).[24] Adapted and reproduced with permission of John Wiley and Sons. (© 2020 WILEY-VCH Verlag GmbH & Co. KGaA, Weinheim)

To accomplish an intercalation reaction, a sufficiently large electronic conductivity needs to be established in the active material to allow electron transport from the intercalation site to the current collector, as shown in **Figure 5a**. Additionally, the charge transfer resistance (**Figure 5c**), *i.e.* the lithium ions transition from a solvated state in the electrolyte to an intercalated state in the active materials crystal structure, needs to be minimized. Furthermore, the ion diffusion in the solid active material as well as the long-range ion transport in the liquid electrolyte both contribute in the kinetic limitations of the charging/discharging processes (**Figure 5b** and **Figure 5d**).[24] Along this line, researchers have improved the electrical conductivity of the active material by additives, such as carbon nanotubes[23] or graphene[25], and lowered the charge transfer resistance by maximizing the active material surface. However, the kinetically limited transport of lithium ions in both solid (active material) and liquid phase (electrolyte) remain challenging. Several groups have addressed this challenge by the introduction of orthogonal channels or voids in the electrodes' structure. They were able to show, that the decreased tortuosity of the electrode layer has a beneficial effect on the charging rate and diffusivity of the Li^+ ions.[26–29] Summarizing, the limited capacity of the active material and the sluggish

diffusion processes need to be resolved in order to meet the future needs of EES devices,[18] which often require high energy densities coupled with fast charging. Therefore, intensive research for novel battery components as well as novel electrochemical systems needs to be conducted.

Along this line, research has been focusing on developing novel electrode materials, which are able to accommodate a higher number of lithium ions (more than one) in order to increase the capacity. Promising candidates for high capacity anodes in lithium ion based electrochemical cells are tin and silicon as well as their respective oxides,[30,31] as they provide a higher theoretical capacity compared to the capacity of graphite. However, upon ion intercalation they suffer from a drastic volume expansion, leading to their fracture and subsequently severe capacity fading.[32,33] This volume expansion is least pronounced in case of the tin oxide, reaching 200 % of its original volume, instead of 400 % observed for silicon.[34–36] Tin oxide, present in nature in the mineral casserite, has been studied for its application as gas sensors[37], solar cells[38] and in the form of indium-tin oxide as a transparent conductive layer and as anode material in lithium ion batteries.[39,40] SnO_2 is usually present in a rutile crystal structure with the space group $P4_2nmn$[41,42] with typical ceramic properties, like high melting point (>1900 °C) and a high Mohs Hardness of 6.5.[42]

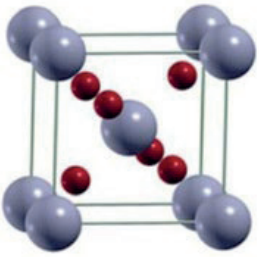

Figure 6. Rutile crystal structure of SnO_2. The grey balls corresponds to tin atoms, whereas the red balls corresponds to oxygen atoms.[43] Adapted and reproduced under the creative commons CC BY licence. (Published by The Royal Society of Chemistry)

It's mechanical properties under compressive stress, with nearly no plastic deformation, a yield strength of 803 MPa and a Youngs Modulus of 373 MPa, typical for ceramics.[44] Recently, it has been studied intensely as active material for lithium ion batteries with a high capacity of up to 1150 mAh g^{-1}.[45] At a charging rate of 1C a reversible performance of around 800 mAh g^{-1} was

obtained, with a decrease roughly up to 600 mAh g^{-1} after 150 cycles due to the volume expansion of the SnO_2 particles. Its specific intercalation reactions and irreversible side reactions are shown in **Figure 7**. The intercalation of a Li ion into Sn or SnO_2 is both based on the charge of valence state from divalent to four-valent tin during the delithiation and *vice versa* during the lithiation. However, additional side reactions like the decomposition or formation of Li_2CO_3 (with the electrolyte) or direct electrolyte (or its respective $LiPF_6$ salt) reduction or decomposition occurs, as shown in **Figure 7**.

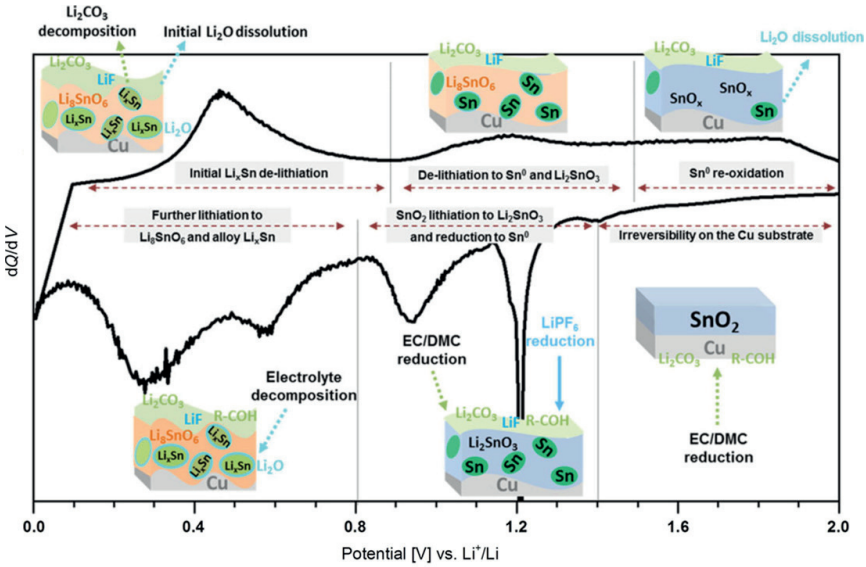

Figure 7. A cyclic voltammogram of a SnO_2 model electrode with the present Intercalation reactions during each specific state.[46] Adapted and reproduced under the creative commons CC BY licence. (© 2020 Wiley-VCH Verlag GmbH & Co. KGaA, Weinheim)

These side reactions are up to a certain point also desired, for the formation of the SEI mostly composed of Li_2CO_3 and decomposed electrolyte, which protects the anode surface. However, due to the large volume expansion of tin, this protecting surface layer is damaged upon charging, leading to additional side reactions, increasing the electrolyte consumption. In order to overcome this effect of the volume expansion, recently the combination with graphene has been discussed as a possible approach.[47,48] Graphene, a monolayer of hexagonally bonded carbon atoms, has become one of the most promising candidates for electrical and electrochemical storage in the recent years.[49–51] The direct preparation of graphene can be

roughly separated into two different routes. Either a top down approach, breaking graphite into the graphene monolayers, or a bottom up approach to physically or chemically grow the graphene.[50,51]

However, both approaches are not suitable to fabricate large amounts of graphene, thereby a chemical oxidation route of graphite was proposed by Hummers *et al*..[52] He and his coworkers were able to partly oxidize graphite using potassium permanganate, sulfuric acid and hydrogen peroxide. Subsequently, oxidized graphene, in a 2D hexagonal structure, is obtained by soft sonication. In order to reduce the graphene oxide, mild temperature treatment in vacuum or a protective atmosphere[53], chemical treatment with hydrazine[54](see **Figure 8**) or a variety of other techniques can be applied.[55,56]

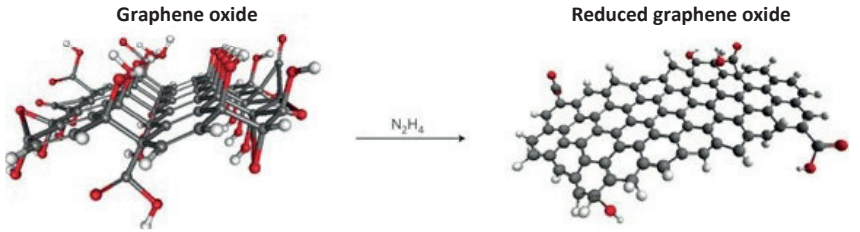

Figure 8. The fabrication of graphene via hydrazine reduction of graphene oxide[57], adapted and reprinted with permission of Springer Nature (Copyright © 2008, Nature Publishing Group)

Its good conductivity along the hexagonal plane is caused by hexagonal bonding structure of the tetravalent carbon atoms. Hereby, the carbon atoms are bonded with each of their three neighbors by a σ-bond, whereas the π-bond is oriented orthogonal to the plane. These π-bonds of the carbon atoms form a π-band, leading to the superior conductivity of graphene.[50] Coupled with its extremely good mechanical properties, a Youngs Modulus of 1000 GPa and a intrinsic strength of 130 GPa and its inherent flexibility,[58] the application as mechanical support for electrochemical storage became feasible.

With regards to its electrochemical properties, it was found, that graphene is also able to host lithium ions. Since graphene sheets will align in parallel during their assembly, lithium ions are intercalated between the single graphene monolayers, delivering a higher capacity of up to 1264 mAh g^{-1}, about three times higher compared to its graphite counterpart.[59] The 2D morphology, proving short diffusion paths and especially its electronic structure have a large influence on the electrochemical performance. For instance, a large increase in charging speed

has been achieved via doping of graphene sheets by nitrogen. This doping results in significantly better conductivity due to the distorted surface morphology and heteroatomic defects.[60] Summarizing, graphene as a 2-dimensional material with outstanding electronic, electrochemical and mechanical properties is a highly interesting material for LIBs. It's application as either a support for high-capacity active material, or directly as intercalation host for lithium ions is favorable.

Going beyond the fabrication of graphene-based composite, several approaches have been proposed to improve and optimize the active material itself. This includes (i) the reduction of the particle dimensions,[6] (ii) the fabrication of composite materials,[61] (iii) the fabrication of high aspect ratio particles[32] and (iv) doping or functionalization[34] (see **Figure 9a – Figure 9d**) in order to fully access the capacity of the electrode material and avoid material degradation **(see Figure 9)**.

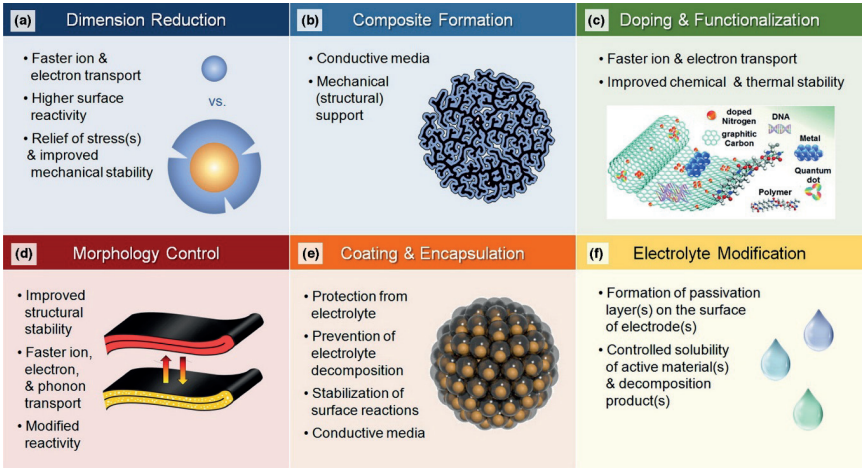

Figure 9. Schematic drawing of different mechanisms to enhance the active material structure by a) dimension reduction, b) composite formation, c) doping and functionalization, d) morphology control, e) coating and encapsulation and f) electrolyte modification.[11] Adapted and reproduced under the creative commons CC BY licence. (Copyright © 2014 The Authors. Published by Elsevier Ltd.)

The decrease in particle size leads to an increase of the accessible surface of the single active material particles for lithium ions. More in detail, the larger surface of the active material particles thereby results in a smaller charge-transfer resistance, as well as the decrease in resistance of a solvated lithium ion being transferred at the active materials surface into the state of a intercalated Li atom.[24] Furthermore, the solid diffusion path for lithium ions in the

active material particle itself is decreased, due to the smaller size. However, with regards to a well-defined intercalation potential, the additional defects associated with the larger surface lead to an overall decrease of the intercalation potential. This detrimental effect can be overcome by the fabrication of high aspect ratio particles, which unite a large surface and high crystallinity. For instance, in case of the cathode material $LiMnPO_4$ the fabrication of nanosheets and their assembly into flower like structures was resulted in a more pronounced intercalation of the ions into the electrode, without a large shift in intercalation voltage.[62] The capacity of the material however, reached only 50 mAh g^{-1}, due to the limited conductivity of the $LiMnPO_4$. The fabrication of a graphite – $LiMnPO_4$ composite enabled the full utilization of the material's potential and resulted in a high capacity of 130 mAh g^{-1} at 1 C after 100 cycles. Even increasing the charging rate tenfold (10 C), the intricate structuring of the active material and the graphitic backbone still permitted a capacity of 102 mAh g^{-1}. Since structuring of the surface morphology or the fabrication of a composite are not the only possible approaches to enhance the active material performance *via* surface stabilization, direct functionalization or doping can be utilized for the same purpose. For instance, graphene can be doped with nitrogen or boron, which leads to a large increase in mechanical stability and electrical conductivity.[60]

1.1.1 Free-Standing and flexible electrodes

The most recent discussion revolving around carbon based (graphene and CNT) current collectors is currently going into its application as free-standing and flexible electrode. Free-standing electrodes are active material layers, which require no additives or additional current collector to function, as displayed in **Figure 10**. The omission of inactive components would result in a higher energy density on a cell level, since neither current collector nor the additives are partaking in the electrochemical reaction.[63] However, current collector free electrodes require a certain mechanical stability, since no supportive metal foil or binder is used, their flexibility is a further prerequisite.[64] This flexibility has spiked the interest in the development of flexible electrodes, because the application of such electrodes in novel multitasking gadgets such as curves displays, phones or flexible wearable electronic devices would be highly beneficial.

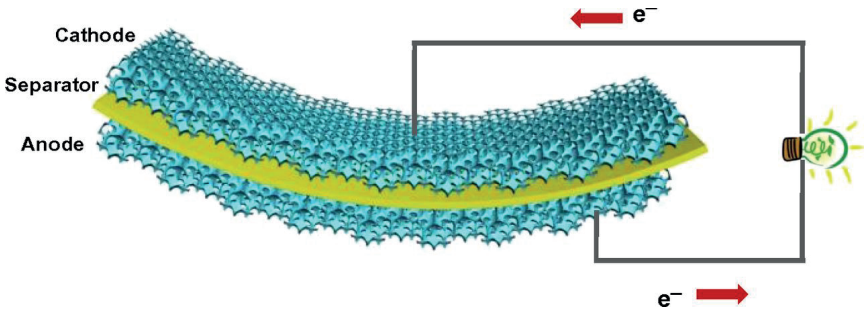

Figure 10. A flexible electrode made from porous graphene with high mechanical stability and a large capacity.[65] Adapted and reproduced with permission of PNAS. Copyright (2012) National Academy of Sciences

Carbon or carbon-composite electrodes, especially based on graphene and CNT's possess the required mechanical strength and stability as well as the conductivity to establish a long-range electron transport. As electrically conducting backbone they are able to provide a sufficient electron supply to the active material, as well as the intercalation sites, for the intercalation reaction to occur.

Furthermore, since the current collector is the mechanical support of the brittle active material layer, a free-standing electrode needs to provide not only the required conductivity, but also the necessary mechanical stability. Hereby, graphene and graphene oxide-based composites are known to form upon self-assembly a 2-dimensional layer of parallelly aligned graphene or

graphene oxide sheets. The mechanical stability and ability of the graphene oxide sheets to align in parallel stems from the hydrogen bonding between epoxy and hydroxy groups at their surface.[66] For instance, in order to augment the cycle life of silicon based electrodes, Wang *et al.* have investigated a flexible silicon reduced graphene oxide composite, in which the silicon nanoparticles have been embedded within the graphene sheets. They were able to show, that the capacity of a free-standing graphene composite was increased from 304 mAh g^{-1} for pure graphene films to 708 mAh g^{-1} for the composite.[67]

The silicon nanoparticles were hereby encapsulated between the graphene sheets in order to preserve their volume expansion, which contributes to the better electrochemical performance of the composite electrode. Other work features respectively graphene based electrodes in which SnO_2[68], TiO_2[69] and CuO[70] nanoparticles are incorporated. With regards to the mechanical enhancement of graphene films, it has been shown, that for instance the addition of 1 wt% PMMA to a graphene dispersion resulted in a significant boost of the mechanical strength of the resulting graphene film by 80 %, due to the strong interactions between graphene and polymer layer.[71] However, in case of the presence of inorganic particles such as tin oxide or silicon, the capacity fading is still a serious issue for such electrodes, since only a weak bonding is established between the particles and the underlying graphene backbone.[50] Specifically, the missing covalent bonding leads to the active material disconnected from the conducting graphene backbone.[51] In order to overcome this hurdle, possible approaches include an one-step synthesis,[72] the application of a precursor[73] or reactive CVD or PVD deposition[74].

1.2 Multivalent Ion Batteries

Due to the current discussions about the availability of lithium and the high toxicity of active material in LIBs, researchers have been focusing on finding and investigating alternative batteries technologies.[75] These battery technologies need to compete with the lithium ion technology in respect of the energy and power density, whilst overcoming the limited use of lithium in these cells and their safety issues.[61] One of the more recent developments, which has sparked the interest of the metal ion battery community, is the intercalation of multivalent ions, such as Ca^{2+}, Mg^{2+}, and Al^{3+}, into different active materials.

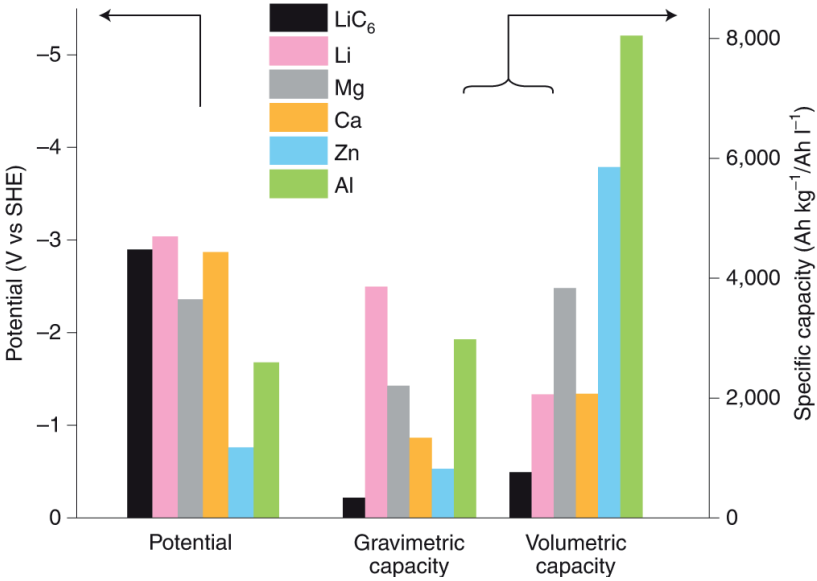

Figure 11. Key performance parameter of multivalent ion batteries.[76] Adapted and reproduced with the permission of Springer Nature. (Copyright © 2020, Springer Nature Limited)

In comparison with the monovalent ions like Li, Na and K, during the intercalation of multivalent metal ion, several electrons are transferred. This leads to a higher charging rate (same reaction rate, but a larger number of electrons is transferred) and a higher energy density.[61,76] Since the energy density of an electrochemical systems is defined by both the capacity and the intercalation potential of the active material, both factors need to be considered when multivalent ions are discussed. With respect to the potential of an electrochemical system

against the standard hydrogen electrode (SHE), multivalent ions have either a lower or similar potential compared to the Li ion, see **Figure 11**. Additionally, since multivalent ions are significantly heavier per volume fraction, *i.e.* are denser than lithium, their gravimetric energy density is lower, due to the inferior intercalation potential and larger weight fraction. However, with respect to their volumetric energy density, multivalent ions have several advantages compared to their lithium ion counterpart. Hereby, the theoretical capacity of an aluminum based EES device can achieve nearly four times the capacity of the lithium based EES.[76]

In order to fully access the capacity of the multivalent ion batteries, a suitable host for the ions is required. Thus, a large number of different active materials have been investigated and the search for new active materials is still ongoing. The active materials in question need to possess a chemical inertness against the respective metal ion, in order to impede an irreversible reaction whilst their crystal lattice needs to be able to serve as host for the metal ion. For instance a highly versatile material which has been under discussion for the storage of monovalent ions like Li, Na and K as well as the storage of multivalent ions like Ca and Al is graphite or its expanded homologue, as shown exemplary in **Figure 12**.[77,78] Hereby, the intercalation of the respective ion species occurs between the expanded graphite (along the c-axis) interlayers, whereas intercalation into the non-expanded graphite is hindered, since the interlayer distance is too small.[79] In fact, graphite or rather the graphite interlayers are large enough to host anion complexes like PF_6^- and $AlCl_4^-$, thus provide sufficient space for intercalation. However, the capacity of graphite is still limited in electrochemical systems based on different mono or multivalent ions. Hereby, the capacity of Na-intercalation into graphite is reaching values of up to 100 – 120 mAh g^{-1}, whereas the intercalation of K-ions into graphite showed a capacity of 279 mAh g^{-1}.[77]

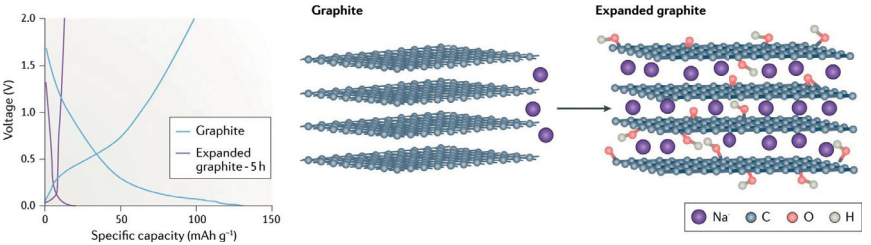

Figure 12. Intercalation of Na into graphite and expanded graphite structures with its respective charging/discharging profiles.[79] Reproduced with permission of Springer Nature (Copyright © 2020, Springer Nature)

A possible substitute for graphite which has been under investigation for high capacity electrodes in lithium ion batteries and is discussed for other monovalent and multivalent ion applications, is SnO_2. It has shown the ability to accommodate Na ion with a capacity of 667 mAh g^{-1} [80] and K ion with a capacity of *ca.* 350 mAh g^{-1} [81,82], and recently has been investigated as intercalation host for Al ions.[83] Similar results have been observed by Lu *et al*., specifically a SnO_2/C composite which displayed a discharge capacity of 370 mAh g^{-1}, with a highly stable capacity of 72 mAh g^{-1} after 20000 cycles.[83] Other possible candidates for multivalent ion intercalation are Sn[84], Sb[85], and Bi[86] for magnesiation and Te[87], SnO_2[83] and VS_4[88] for aluminisation are under investigation. Aside from the search for novel active materials, one of the major challenges is the diffusion of these multivalent ions trough the solid electrolyte interface (SEI) and the formation of dendrite upon deposition.[79] In case of the lithium ion based system, the SEI is formed during the first charging cycles, its nature is electrically insulating, whereas it remains ionically conductive. However, upon cycling multivalent ion electrodes (*e.g.* Al^{3+}, Mg^{2+} and Ca^{2+}) a passivation layer is formed, which is not ionically conductive.[79] Accordingly, finding electrolytes which form a SEI that permits the conduction of multivalent ions remains still a challenge. The most suitable intercalation ion, which has a high potential to substitute lithium, is aluminum, due to the high volumetric energy density.[79] However, due to the high reactivity of aluminum ions, a novel electrolyte is required, which allows the presence of aluminum ions, supplies sufficient ion transport and chemically inert against the applied potentials. Hereby, the novel class of imidazole based ionic liquids has emerged as possible candidate for aluminum ion batteries, which are able to withstand thousands of cycles and supports the multivalent ion transport.[89] The application of this electrolyte, in which $AlCl_3$ salt is dissolved, has proven beneficial in the application of aluminum batteries, in which carbon based materials were investigated as electrode material.[90] These carbon based electrodes, such as graphite[91] and graphene[92] deliver a capacity of up to 2.25 V *vs* Al/Al^{3+} and are applied as cathode material as presented in **Figure 13a** and **Figure 13b**. For instance, Lin *et al*. were able to show, that intercalation of a negatively charged $AlCl^{4-}$ ion occurs within the honeycomb layers of graphite (see **Figure 13a**). Extremely high charging rates as shown in **Figure 13c** could be achieved by using an intricate architecture, namely a graphitic foam structure, which provides good accessibility to the $AlCl^{4-}$ complexes and short ion diffusion paths.

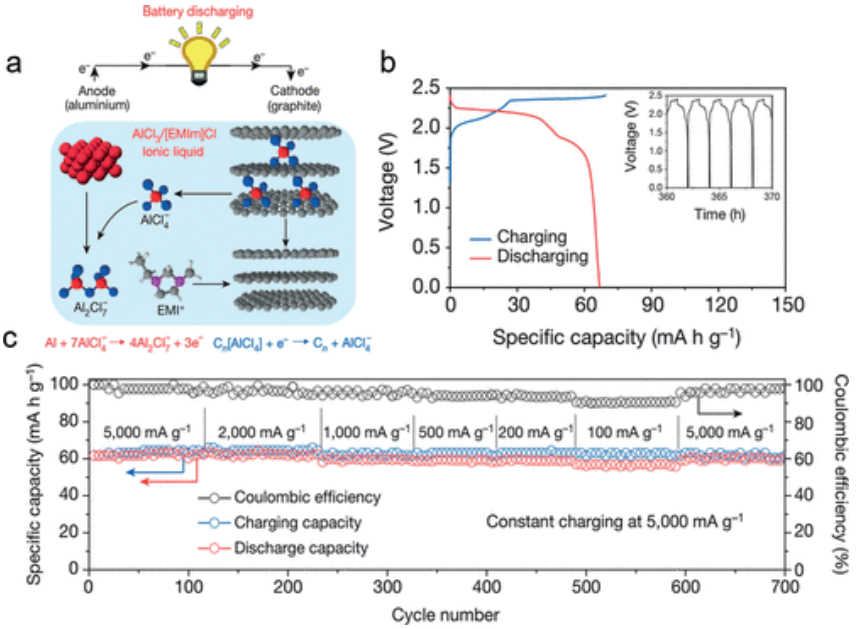

Figure 13 A ultra-fast charging aluminium based graphite battery.[93] Reproduced with permission of Springer Nature (Copyright © 2015, Nature Publishing Group, a division of Macmillan Publishers Limited. All Rights Reserved.)

As corresponding counter electrode pure aluminum metal foil was investigated[93] and no dendrite growth, as well as no SEI formation occurred, due to the use of an imidazole based electrolyte.[90,93,94] From a structural point of view, *i.e.* ion diffusion paths and morphology, the design principles of active materials can be transferred from monovalent ion-based- to multivalent ion-based systems.

1.3 Bioinspired assembly and structuring techniques

An approach to design and tailor the structure of the active material with key parameters for the application as electrode in mind, is a bioinspired or biomimetic approach. Bioinspiration is the observation of a phenomenon in a biological system and its transfer to an application[95], whereas biomimetics is not merely taking the inspiration, but a direct copy of a biological design principle and its application in an artificial system.[96] Since both principles are based on a deep insight into the structure-functionality relation of a biological system, in order to transfer its main functionality (biomimetics) or construct an artificial system inspired on the main design principles (bioinspiration), intensive research of diverse biological systems has been done. The main advantage of these approaches is that nature had millions of years to design and tailor a biological system with the help of natural selection and as such has achieved an astonishing degree of miniaturization and organization.[96] Usually nature is able to achieve this astonishing goal by the hierarchical assembly of miniaturized components, such as it is observed for instance

in nacre[97] and calcareous sponge structures[98]. Hereby, the components are assembled in such way, that a macroscopic structure is formed by the assembly of nanometer sized components. This hierarchical assembly leads to an exceptional combination of mechanical properties like hardness and stiffness, which has not been observed for their monolithic counterparts.

1.3.1 Nacre

Nacre is on organic-inorganic composite biomaterial produced by a mollusk-type organism, which is formed for protection, buoyancy and even elaborate hunting techniques.[99,100] The red abalone (*Haliotis Rufescens*)[101,102] is an organism which is able to form such an iridescent layer on the inside of its shell. Nacre constitutes of 95 wt % brittle ceramic material ($CaCO_3$) and only 5 wt % organic matrix material.[101,103]

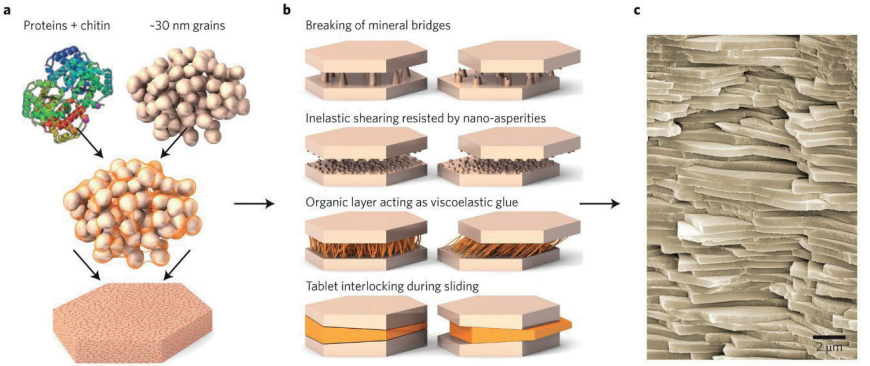

Figure 14. The formation of the mesocrystalline aragonite platelets (a), the hierarchical effects leading to energy dissipation in a nacre structure (b) and c) a SEM micrograph of nacre brick-and-mortar structure.[104] Adapted and reproduced with the permission of Springer Nature. (Copyright © 2014, Nature Publishing Group, a division of Macmillan Publishers Limited. All Rights Reserved.)

Nacre itself has viscoelastic properties, due to the intricate layering of the aragonite platelets **(Figure 14a)**, the biopolymeric interlayers and interconnecting mineral bridges, as shown in **Figure 14b**. The composite is assembled in "brick-and-mortar" structure (see **Figure 14c**), with aligned mesocrystalline aragonite platelets, with a thickness of up to 500 nm forming the "bricks" and the interconnecting organic layer comprised of β-chitin forming the "mortar".[103,105]

This highly organized structure is the main reason for the 2-fold increase of the strength of nacre compared to its monolithic, brittle $CaCO_3$ counterpart.[106,107] Furthermore, the fracture toughness of nacre in higher by a factor of 8 due to crack deflection on the aragonite platelets.[106] Upon crack formation, crack is not propagating through the aragonite platelets, but around them, which leads to additional energy dissipation. Conversely, the Youngs modulus is maintained and is similar to that of the monolithic $CaCO_3$, due to a small amount of organic material present between the aragonite platelets. Beyond the layered microstructure of nacre, additional architectural features, like nanoasperites[103] on the platelets, mineral bridges[97] and

the intricate structuring of the aragonite platelets themselves[99] further enhance the mechanical stability of nacre, as displayed in detail in **Figure 14b**. Furthermore, the sub micrometer sized aragonite platelets are composed of nanosized particles with an average diameter of about 30 nm,[99] which are displaced when they are exposed to stress, contributing further to the energy dissipation in the material.[97]

As shown in **Figure 15**, the intricate structuring of otherwise mechanically weaker components, significantly contributes to the extraordinary mechanical stability of nacre. According to Wegst *et al*., a similar improvement has been also observed in bone, which has a different architecture as well as in nacre-mimicking alumina/PMMA composite.[104]

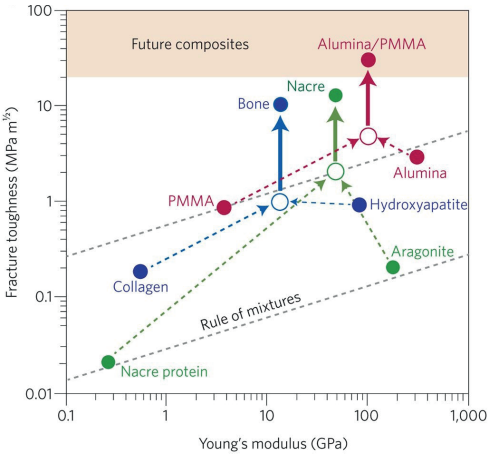

Figure 15. The mechanical improvements achieved by intricate structuring, for example in bone and nacre. These design principles can be transferred to artificial material, which consequently possess highly improved mechanical properties (exemplary shown for an Alumina/PMMA composite).[104] Adapted and reproduced with the permission of the Nature Publishing Group. (Copyright © 2014, Nature Publishing Group, a division of Macmillan Publishers Limited. All Rights Reserved.)

In order to transfer such an intricate structure to an artificial system, a large number of different experimental techniques, like freeze-casting, hot-press assisted slip casting and self-assembly processes have been proposed.[108] Especially the self-assembly technique has spiked the interest of researchers in the field, since the approach is a green method, and does not require high temperatures or pressures to work, but instead is based on particle – substrate interactions.[108] These interactions are mostly governed by electrostatic or van-der-Waals forces, which lead to an ordered assembly of molecules or particles on the substrate. Continued growth of the layers

can be ensured by the surface chemistry (*i.e.* the strength of the respective interactions) of the particles or molecules and can be achieved via dip coating.

For instance, in the work of Burghard *et al.*[109] positively charged polyelectrolyte and the negatively charged surface of TiO_2 was used to alternatingly deposit a soft polymer and hard ceramic layer. They were able to observe a 16 % increase in hardness and a 7.5 % increase in the Youngs Modulus for the nacre-like multilayer sample compared to the pure TiO_2 counterpart.[109] A similar technique is adopted by Jahnke *et al.*[110], using the hydroxyl surface groups of graphene oxide and their associated hydrogen bonds to self-assembly SnO_2 nanoparticles from an aqueous dispersion. The variation of the graphene oxide to tin oxide ratio enabled the control over the surface-surface interaction and thus an ordered layered assembly of the composite material.

1.3.2 Calcareous Sponges – Clathrina Clathrus

Nature design principles for cellular biological materials, such as sponges, can be adapted to fabricate a porous, yet mechanically stable structure. For instance, the sponge *Clathrina Clathrus* (*Clathrinidae*, *Calcarea, Porifera*),[98] first discovered on the British Isles in 1818 is an interesting example of a highly porous organism comprising of organic tubes which are stabilized with a ceramic backbone, as shown in **Figure 16a**.[111] The organic tubes are highly flexible as can be observed from **Figure 16b** and are used to filter micro plankton from sea water. On the inside of these channels, Flagellate cells are actively able to generate a water currents and as such provide the sponge with a stable food supply.[112]

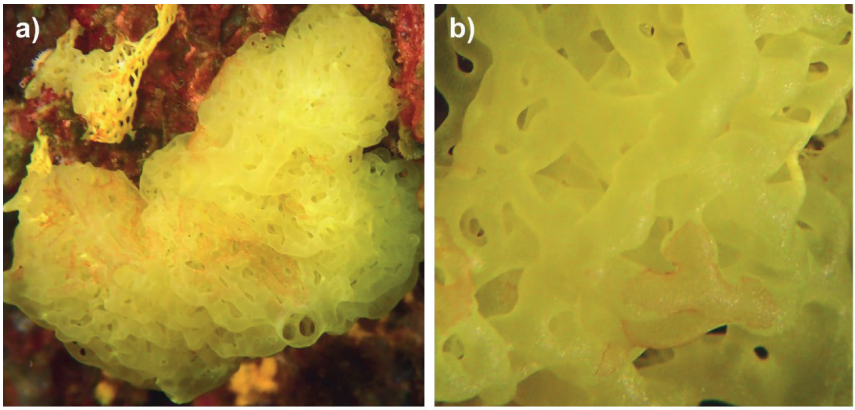

Figure 16. The sponge clatrina clathrus in its natural habitat as a complete organism (a) and is channel-like structure in (b).[113] Reprinted and adapted with permission of the Royal Society of Chemistry. (Copyright © 2019 The Author(s) Published by the Royal Society.)

Their skeleton is entirely composed of independent calcite triactines, displayed in **Figure 17c** and **Figure 17d**, serving as the mechanical support and backbone for the channel-like, tubular superstructure of the sponge.[111] The triactines are composed to 99.9 wt% calcite ($CaCO_3$) and only around 0.1 wt% proteinaceous organic matter.[114] The spicules are characterized by their trigonal symmetry with an angle of 120 ° between them. They have a width of 8 µm – 13 µm and a length of up to 200 µm with tips on the outer ends.[98] From a crystallographic point of view they appear to be single crystalline, with a trigonal symmetry in the space group $R\bar{3}c$.

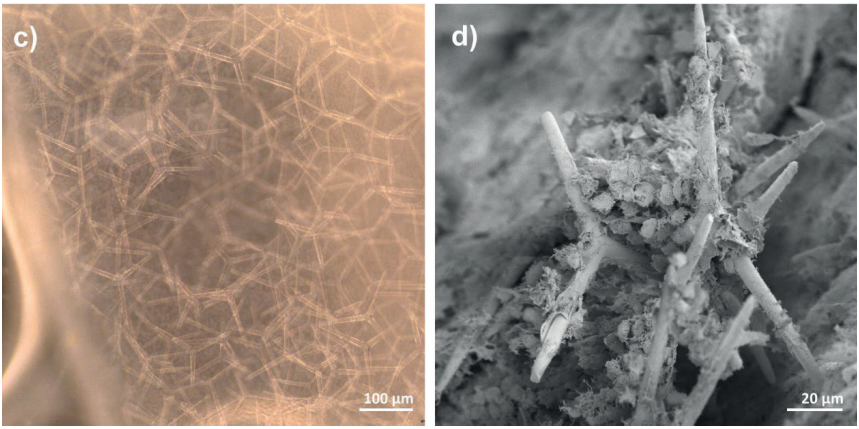

Figure 17. Triactines of the clatrina clathrus sponge in the light microscope (c)) and in the SEM (d).[113] Reprinted and adapted with permission of the Royal Society of Chemistry. (Copyright © 2019 The Author(s) Published by the Royal Society)

Travis *et al.* [115] revealed using high-resolution TEM techniques, that the macroscopic triactines were indeed composed of highly ordered $CaCO_3$ crystals in the nanometer range (10 – 30 nm)[114], similar to the ordered nanocrystals observed in nacre. The crystal growth of the spicules begins in cavities where specialized cells control the crystal growth and surrounding aqueous conditions.[116] Continued oriented crystal growth and thickening of the spicule takes place along crystallographic preferred direction. The orientation of the crystals is hereby controlled by the small amount of organic protein, which interacts with specific crystal planes.[117] The oriented primary building block of highly ordered calcite crystals is assembled in a brick structure, similar to bricks in a wall. This assembly of the triactines leads to enhanced mechanical properties with crack deflection occurring between the single oriented crystals as revealed by Sethmann *et al.*[114].

The concept of such a biological system, with both a stable backbone and a large inner surface can be adapted for a technologically relevant material. As a possible approach to fabricate such an intricate channel-like structure, ice templating can be applied.

1.3.3. Ice-templating technique

The fabrication of intricate structures, especially structures which resemble natures design principles, has been pursuit by researchers over the last years. Along this line, cellular materials can be fabricated by using any kind of porous template on which a material of interest is deposited using either CVD, PVD or chemical synthesis techniques. This template can subsequently be removed either chemically or physically, yielding a free-standing cellular material. However, going through the tedious and challenging task of the template removal might impose unwanted confinements on the fabricated material. More in detail, a template structure, for instance made of polyvinylalcohole, on which a material is deposited (*e.g.* carbon) can by simply removed by its immersion in water. On the other hand, the aqueous solvent is introducing strong capillary forces due to the small pore size of the cellular material, which can lead subsequently to the collapse of the cellular materials structure.[118] In order to overcome the detrimental capillary forces, a colloidal dispersion of a solid functional material in a solvent is stabilized and frozen. To avoid strong capillary forces imposed on the material by a phase transition *via* the liquid phase, a direct transition from either solid phase to the gaseous phase is required.

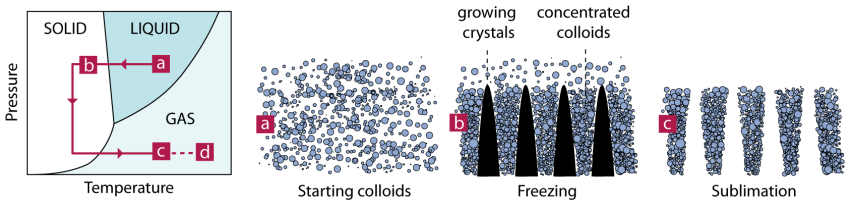

Figure 18. Schematic of an ice-templating process, starting from a) the liquid colloidal dispersion, b) the growth of ice-crystals and c) the subsequent sublimation of the solvent.[118] Adapted and reprinted with permission of Nature Springer. (Copyright © 2013, The Materials Research Society)

As possible techniques to remove the solvent, critical point drying and freeze-drying can be used to fabricate highly porous material with extremely small pore sizes (<100 µm).[118] The former is making use of the phase transition at the critical point of a solvent (e.g. water or ethanol) to directly transfer the solvent into the gaseous phase whilst intricately controlling both temperature and pressure. The latter (freeze-drying) is based on the sublimation of the solid solvent at low pressures to remove the solid crystal structure from the cellular material, without the influence of strong capillary forces, as shown in **Figure 18.**

Freeze-drying has thereby an additional advantage that the ice (*i.e.* the template) can be tailored by different additives (*e.g.* glycerin) or simple temperature gradients to control the size of the ice crystals or their growth direction to yield highly oriented structures. Since the ice is acting as a removable template in this case, the technique is called ice-templating.[118]

More in detail, the freezing process of the ice occurs according to the principles of crystal nucleation and growth. Specifically, the orientation of the ice crystals as well as the number of their nuclei determines the architecture of the cellular material, see **Figure 19b**. The formation of the ice crystals itself can occur either by a homogeneous nucleation or a heterogeneous nucleation. A homogenous nucleation is a formation of nuclei which occurs in the volume of the solvent without any preferential sites due to a (local) negative Gibbs Energy. The nuclei are defined by the local change in Gibbs Energy, which can be written as shown in **Equation 1**.

$$\Delta G = \Delta G_s + \Delta G_V \qquad [1]$$

Whereas ΔG corresponds with the free Gibbs energy, with ΔG_s and ΔG_V the volume and their surface specific term. The whole term is described by **Equation 2**, with σ the surface energy and Δg being the volumetric free energy.

$$\Delta G = \sigma 4\pi r^2 + \Delta g \frac{4}{3}\pi r^3 \qquad [2]$$

The derivation of the Gibbs free energy ΔG in **Equation 2** by the radius yields the critical radius r_c for a nucleus. Hereby, if the radius of a nucleus is smaller than r_c, the nucleus will subsequently be dissolved, whereas if the radius of the nucleus is larger than r_c, the nucleus will continue to grow.[118]

For the heterogeneous nucleation, the ice crystal formation is much more complicated since the crystal formation is induced at a surface of a template (*e.g.* bottom of a beaker), or even by the surface structure of the colloidal particles themselves. For instance, at the respective surface, *e.g.* colloid particle or template, the local free Gibbs Energy is lowered, which leads to preferred nuclei formation at the interface.

The heterogeneous nucleation in combination with a temperature gradient (i.e. a gradient in the driving force of the crystallization) can be applied to fabricate a channel-like structure (**see Figure 19a**). For instance, if a surface is cooled below the freezing point and it is immersed into a colloidal dispersion, nucleation in the solvent will occur in close proximity (or directly at the interface) of the surface. During continued cooling, the solidification front is moving in along

the temperature gradient, inducing an orientation into the obtained crystals, as shown schematically in **Figure 19b** .[119] The colloidal particles are dispelled from the solid-liquid interface and upon increased concentration are confined between single crystals.[118] In case of an aqueous solvent, a temperature gradient leads to lamellar growth of the ice crystals, thus channel-like structure can be easily obtained, as shown by Deville *et al.*.[120] They were able to show the ice crystals structure using x-ray tomography. The aqueous dispersion of alumina particles was frozen along a temperature gradient the lamellar growth of ice crystals and the subsequently obtained lamellar structure.[120] However, the growth of the ice crystals occurs in three stages (**Figure 19b**), first the nucleation or a large number of grains at the cooled interface (i), then the growth of small crystals (ii), which with increasing distance from the cooled interface form lamellas (iii).[113,120]

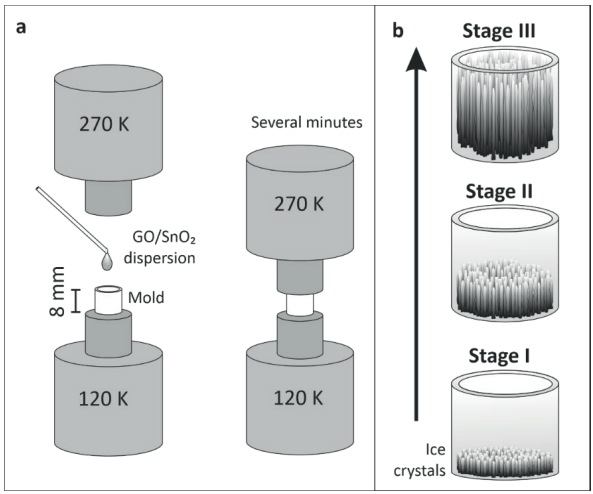

Figure 19. a) Exemplary schematic on a large temperature gradient and the fabrication of a channel-like architecture. b) the different stages during the solidification process of the liquid dispersion.[134] Adapted und Reprinted under the terms and conditions of the Creative Commons Attribution (CC BY) license from Nanomaterials MDPI. (Copyright © 2020 by the authors. Licensee MDPI, Basel, Switzerland.)

Subsequently, the ice crystals are removed by sublimation and a highly porous green body is obtained, see **Figure 18.**[121]

Summarizing, the ice-templating technique enables fabrication of a large variety of cellular materials. An intricate control over the architecture such as coral-like[122] or channel-like [123] and

core shell architectures[121] can be achieved by making use of large temperature gradients[122], additives and structured surfaces[124].

1.4 Relevance and outcome of this thesis

Inspired by the structure and properties of *Clathrina Clathrus*, the research aimed to mimick such a hierarchical structure, using technologically relevant inorganic materials such as tin oxides, which can be used, amongst others, as electrode material. In order to achieve this structure, a suitable fabrication process is essential. Therefore, a mineralization process was established, which allowed controlling the formation of the phase (SnO, SnO_2) and morphology (platelets, crosses). In a further fabrication step, SnO crosses were combined with polyvinylpyrrolidone (PVP) and co-assembled in a unidirectional ice-templating process to obtain a highly porous organic superstructure reinforced with inorganic crosses, resembling the microstructure of the *Clathrina Clathrus* sponge. Using PVP as organic phase provides mechanical elasticity, but this electrically insulating component would not contribute in the charging-/discharging process of electrodes in metal ion batteries.

However, since PVP is not electrically conductive, it was required to substitute it with a material, which unites good mechanical properties and inherent electrical conductivity with the possibility of intercalation of ion species, when being stacked.[125] Graphene is a promising candidate for the application and can be obtained from graphite *via* a chemical oxidation process, which was pioneered by W.S. Hummers.[52] This process leads to an aqueous dispersion of exfoliated graphene oxide (GO) sheets. Though not being electrically conductive in this state, the presence of oxygen-containing functional groups on its basal planes and edges prevents agglomeration of the sheets and allows various assembling techniques to fabricate different microstructures. In case of GO assemblies, the graphene oxide sheets correspond to the aragonite platelets in nacre, while the matrix is represented by an hydrogen-bond network.[126] This “brick-and-mortar” structure cause an extraordinary mechanical performance, including mechanical flexibility, which opens the possibility of fabricating binder-free, paper-like electrodes. An important task toward such electrodes is to tune the electrical conductivity of the insulating GO. After assembling, the GO can be chemically or thermally reduced, which drastically boosts the electrical conductivity by restoring the original sp^2-hybridization,[66] while its mechanical flexibility is preserved. The resulting reduced graphene oxide (rGO) electrode material exhibits a theoretical capacity larger than that of pristine graphite, due to additional intercalation sites at the edges. [11]

One way to increase the capacity, while preserving the mechanical performance, is to combine the rGO with other active materials such as SnO_2, as described in **Chapter 3**. Using a similar

hydrothermal, particles exhibiting an intermediate phase ($SnCl_x(OH)_yO_z$) were fabricated, which were added to the aqueous GO dispersion. Co-assembling by a facile drying process resulted in composite papers. They were thermally treated in a final step, yielding paper-like rGO/SnO_2 electrodes and were tested as anode in LIBs.

While the achieved capacity was approaching the theoretical capacity of tin oxide (990 mAh g^{-1})[35], the discharging rate still required some improvement. The discharging rate could be boosted by shortening the diffusion path and increasing the specific surface area. Both can be achieved by co-assembling the GO sheets and the intermediate phase of the SnO_2 particles analog to the PVP and SnO crosses. The ice-templating approach yielded highly porous, sponge-like microstructure, comparable to what can be found in nature,[122] which was also preserved after the final thermal treatment, as investigated in **Chapter 4**. The highly porous microstructure was also expected to have a positive impact on the electrochemical performance. The strongly increased surface area of the rGO/SnO_2 sponge enables the so-called pseudocapacitive effect, in addition to the conventional diffusion-controlled electrochemical storage. Ion species can thereby adsorb/desorb on the surface at a high speed. Moreover, in contrast to the ion intercalation, the adsorption is not space restricted. Therefore, also larger ion species, such as Al^{3+} or $AlCl_4^-$, can be used. Opposed to the rGO/SnO_2 anode in LIB, in Aluminum Ion Batteries (AIB) the rGO/SnO_2 is utilized as the cathode due to the different potential window of this system.

The research proves that combining both, rGO and SnO_2, in a bioinspired, hierarchically structured hybrid material opens up a novel field with a possible breakthrough in metal ion battery technology. Fast charging rates, typically observed for capacitors, and large energy densities can be simultaneously integrated into one electrode, using bioinspired design principles and integration of both flexible and brittle components.

1.5 Discussion

In the field of metal ion batteries, most research focusses on increasing the electrochemical performance of a single active material *e.g.* by downscaling the particle size[127] to compensate the drastic volume expansion of materials, such as tin oxide. To this end, Wang *et al.*[127] were able to obtain ultrathin SnO_2 platelets with a thickness of several nanometer, displaying a good electrochemical performance during Li ion intercalation with a capacity of 500 mAh g^{-1} after 50 cycles. Whereat, these small particles were being embedded in a matrix made of carbon black and binder, analog to conventional electrodes, a loss of energy density on a cell level is observed, due to the introduction of inactive additives. These additives usually contribute to the weight without being electrochemically active, whilst additionally, their interfaces induce irreversible side reactions, which leads to a capacity loss upon cycling. Recently, researchers have addressed hybrid electrodes as a possible solution, which are composed of only active material (*i.e.* without additives). They made use of the interplay of different active materials in order to obtain a mechanically stable and conducting electrode, without the need for additives and a current collector. Thus, a free-standing hybrid electrode, composed solely of active material without additives or current collector is desired. Furthermore, the integration of the active material into the electrodes overall structure is of great importance for the cycle life and performance of the electrode, since side reactions can be decreased and volume expansion, occurring for instance in Sn and Silicon can be compensated.

As example of a possible approach to obtain a hybrid electrode served the work of Cho *et al.*[40], who combined SnO and SnO_2 structures in a yolk-shell architecture, which delivered a large capacity of 600 mAh g^{-1} to 800 mAh g^{-1} at charging rates between 0.5 C to 5 C. However, this structure lacked with regards to the integration of active material into the surrounding matrix composed of binder and conductive additives of the electrode, thus having a short cycle life with 30 % capacity loss in 250 cycles. Other researchers combined SnO_2 with a second, mainly carbon based component to improve the electrical contact between active material and matrix, resulting in better electrical conductivity, charge transfer and cycle life.[128]

Accordingly, these challenges have been addressed in this thesis by assembling SnO_2 and reduced graphene oxide in a bioinspired fashion and tailoring of the active material. In detail, the active material could be tailored as platelets and crosses, whereas a bioinspired approach was used to embed the tailored active materials into the microstructure of the electrode leading to a freestanding 2D paper-like and a freestanding 3D scaffold electrode. Both electrodes were

tested in Li ion based as well as Al ion-based intercalation systems. This approach leads to a large capacity of the 2D paper-like composite of up to 700 mAh g^{-1} at a charging rate of 100 mAh for Li ion intercalation. With regards to the 3D bioinspired scaffold composite, it could be shown that intercalation of Al ions results in a capacity of 50 mAh g^{-1} and the electrode shows a stable performance even after 20000 cycles, demonstrating the good electrochemical and mechanical stability of the bioinspired electrode structure.

1.5.1 Tailoring the morphology and structure of the active material

Initially, the work “Bioinspired synthesis of SnO crosses as backbone in artificial sponges” considers a hydrothermal synthesis to obtain tin oxide particles of different phase and morphology. Foremost, systematic studies revealed that adjusting the ammonia concentration is crucial for tailoring the phase and morphology of the tin oxide particles. At low ammonia content platelet-like structures in the size of 10 nm to 100 nm can be obtained, which exhibit a different stoichiometry compared to SnO_2, depending on the amount of accessible oxygen. The tin oxide precursor ($SnCl_x(OH)_yO_z$) can be obtained by increasing the concentration of the aqueous ammonia solution from 0.45 M to 0.8 M, thus increasing the amounts of reactants in the reaction volume.

When increasing the ammonia content, cross-like structures, resembling the triactines, found in the *Clathrina Clathrus* sponge, can be obtained. These cross-like structures composed of SnO were synthesized using a larger amount of ammonia compared to the synthesis of the platelet structures. The larger amount of ammonia ($Sn(II)/NH_3$ ratio smaller 0.55) hereby hinders the oxidation of Sn(II) to Sn(IV). The preferred crystal growth leading to the cross-like structures occurs along the (1-10) and (112) planes with an intersection on the (112) axis, leading to the formation of a cross-like morphology. Furthermore, the absence of a template in the hydrothermal synthesis leads to a homogeneous formation of nuclei, resulting crosses of equal size.

Furthermore, the formation of the SnO crosses was investigated by means of a time resolved study. After a reaction time of 1h, the formation of highly crystalline SnO is observed according to PXRD studies conducted on the reaction product. Upon prolonged reaction times, no further change with regards to the crystal structure was observed. The formation of the morphology of the SnO crosses was investigated using the SEM, which revealed that first the SnO crystals are formed in a cubic shape, whilst still amorphous or nanocrystalline powders are present after a reaction time of 1h. After a reaction time of 4 hours, larger plates with an edge length of several micrometers are observed and the secondary powder phase is significantly reduced. Prolongation of the reaction time to 6 hours lead to the formation of highly crystalline and fully formed cross-like structures, with very little residual amorphous phase left. However, further prolongation of the reaction times (24h) lead to a complete reaction of the amorphous phase, but the cross-shaped structures seem to be covered by precipitation.

These 2D platelet- or cross-like structures facilitate according to literature the solid-state diffusion of lithium in the active material, since the diffusion path is significantly reduced compared to the bulk material.[24]

In order to embed the cross-like structures into a flexible backbone, analogues to the bioinspired structure of the sponge *Clathrina Clathrus*, an ice-templating technique is adapted. The sponge *Clathrina Clathrus* exhibits a hierarchical microstructure composed of a highly porous channel-like scaffold, which is reinforced with calcite triactines. These triactines are resembled by the cross like tin oxide structures, which are embedded into a suitable matrix. The matrix is able to withstand the enormous volume expansion and should correlate to the channel-like structure of the original foam microstructure. In order to generate a comparable organic matrix, the ice-templating as structuring technique allowed fabrication of highly porous, oriented microstructures. As a proof of concept to fabricate this bioinspired structure with an active material, a combination of the electrochemically active SnO crosses with PVP was investigated. Hereby, the cross like SnO structures were embedded into a flexible matrix with strong mechanical connection to the backbone (*i.e.* PVP) and short ion diffusion paths, which can be obtained by a channel-like microstructure induced by a large temperature gradient during ice-templating. However, as PVP is a poor electrically conductive, the embedded crosses were isolated, not being able to contribute in any electrochemical process. The crosses where however well embedded into the channel-like matrix, as was the aim of this work.

Thus, combining an active material with a flexible matrix enables the fabrication of a stable, bioinspired structure. Different strategies to utilize the PVP in the fabrication process of electrode materials is presented by Hwang *et al*.. [4] He and his coworkers electrospun fibers composed of a tin oxide precursor and PVP. In a subsequent thermal treatment, the fibers were pyrolyzed, yielding porous SnO_2 fibers. However, in order to apply these fibers in an electrochemical cell, the fibers were mixed with carbon black and binder and the resulting slurry was coated onto the metallic current collector in order to obtain the electrodes. Thus, the advantage of the bioinspired structuring is lost.

In the research conducted on SnO crosses, the advantages of a sponge-like structure for designing novel, free-standing electrodes are presented. Hereby, the active material in the form of crosses can be freely accessed by Li ions and is tightly connected to the supporting backbone, which enables excellent electron transport.

1.5.2 Embedding the active material into a graphene-based 2D structure for Lithium-Ion-Batteries

The work "Coalescence in hybrid material: The key to high-capacity electrode" demonstrates the potential of bioinspired microstructures. It is presented, that a bioinspired microstructure allows the fabrication of self-supporting, binder-free electrodes, when PVP is replaced by graphene, respectively GO. In order to obtain a free-standing 2D electrode structure based on a bioinspired approach, the SnO_2 precursor particles were synthesized using a hydrothermal approach.

Similar to the work of Hwang *et al*.[35], a tin oxide precursor ($SnCl_x(OH)_yO_z$), obtained by adjusting the hydrothermal approach with a lower amount of ammonia (($Sn(II)/NH_3$ ratio larger 0.55) as compared to the cross-like shapes was utilized and mixed with GO instead of PVP before co-assembling. Subsequently, the dispersion containing the GO and SnO_2 precursor in a 2:1 weight ratio, underwent a bioinspired self-assembly process. The water from the aqueous dispersion was slowly evaporated to enable a structured co-assembly of the SnO_2 precursor and the GO sheets to fabricate a paper-like electrode, as schematically illustrated in **Figure 20a**.

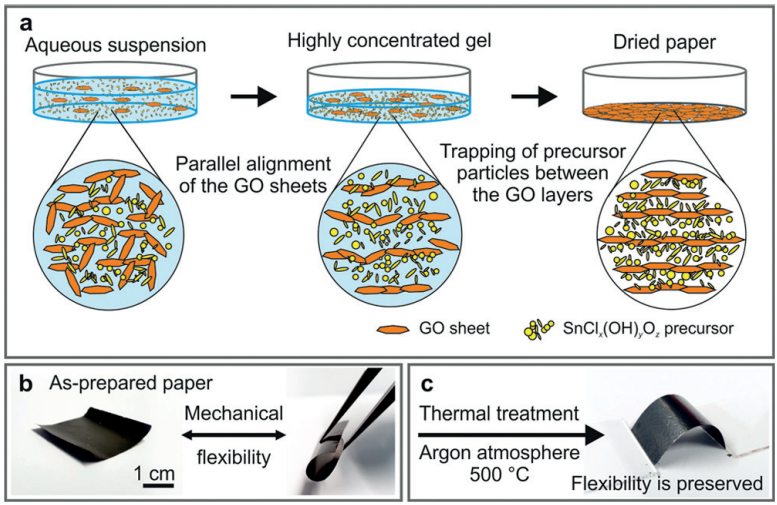

Figure 20. A) A schematic of the bioinspired co-assembly of the SnO_2 precursor material and b) the obtained flexible paper-like composite material before annealing and (c) after annealing.[110] Copyright © 2018, American Chemical Society. Reprinted with permission of the American Chemical Society.

During the evaporation process, the hydroxy- and epoxy- surface groups of graphene oxide form a network in which the SnO_2 precursor material is embedded. However, the precursor is not

strongly bonded to the supporting GO backbone and the graphene oxide is not electrically conductive. In order to tackle both issues, the composite paper-like electrode was annealed at 500 °C with a slow heating rate of 4 K min^{-1}, with the aim to enhance the stability of both components and improve the electrical conductivity. The annealing process lead to a reduction of the graphene oxide, yielding reduced graphene oxide (rGO) in the process, whilst simultaneously the SnO_2 precursor is oxidized to nanocrystalline, phase-pure SnO_2, as shown in **Figure 20b** and **Figure 20c**. More in detail, during annealing in an inert atmosphere, the oxygen containing surface groups bound to the GO sheets are being released, restoring the sp^2-hybridization which renders the rGO electrically conductive. The released oxygen is taken up by the $SnCl_x(OH)_yO_z$ to fully oxidize the inorganic particles, yielding SnO_2, as schematically illustrated in **Figure 21**.

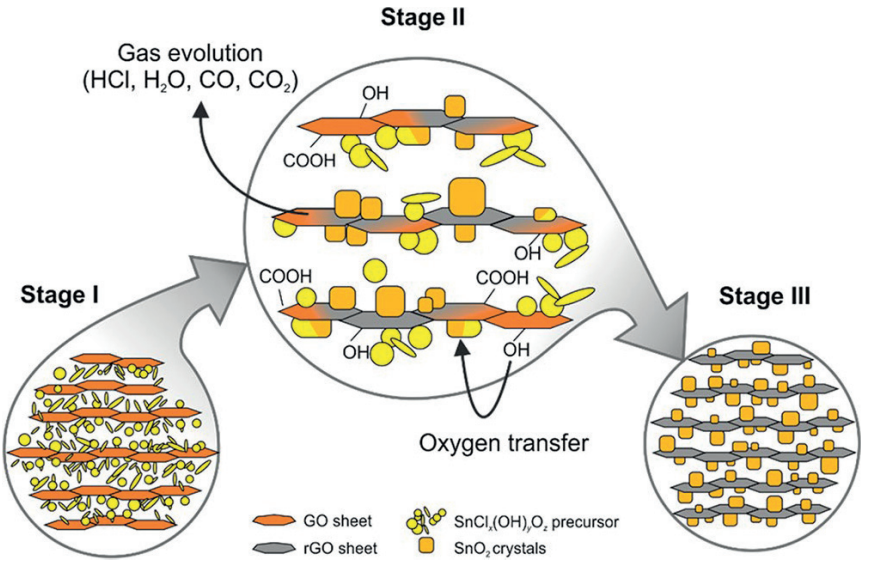

Figure 21. Schematic illustration of the annealing process, upon which a direct oxygen transfer from the graphene oxide to the $SnCl_x(OH)_yO_z$ precursor occurs.[110] Copyright © 2018, American Chemical Society. Reprinted with permission of the American Chemical Society.

This oxygen transfer does not only change the phase of both components, but also leads to mechanical anchoring of the SnO_2 onto the rGO sheets, providing good contact and additional intercalation sites for ideal electrochemical performance. Using HRTEM and PXRD it was found, that the SnO_2 nanocrystals exhibit a textured growth in the direction of the (110) – planes, which

is hypothesized to be caused by the anchoring on the rGO sheets. This thermal treatment yielded the desired self-supporting, binder-free rGO/SnO_2 electrodes, which exhibit a layered microstructure comparable to natural nacre.

Consequently, these paper-like electrodes were tested as anode material in LIBs. It was found, that a capacity of up to 700 mAh g^{-1} at a discharging rate of 100 mA g^{-1} is achieved. In comparison to literature, SnO_2 nanorods[48,129], as well as flower-like SnO_2 structures[36] in combination with graphene yielded capacities around 700 mAh g^{-1}, which is in good accordance to values obtained for 2D paper-like electrode. However, the direct application of the paper-like electrode as anode in a lithium cell enabled the omission of additives in the fabrication process. Furthermore, the paper-like electrodes showed superior performance with a capacity of *ca.* 100 mAh g^{-1} at a high charging rate of 1000 mAh g^{-1} over 300 cycles.

1.5.3 Embedding the active material into a 3D ultra-porous foam structure for Aluminium Ion Batteries

While the facile room temperature self-assembly process led to a dense microstructure, the specific surface area of the rGO/SnO_2 composite could be significantly increased by applying ice-templating technique, already used with PVP, leading to the bioinspired sponge-like superstructure. A schematic of the fabrication technique and construction as an electrochemical cell is shown in **Figure 22**.

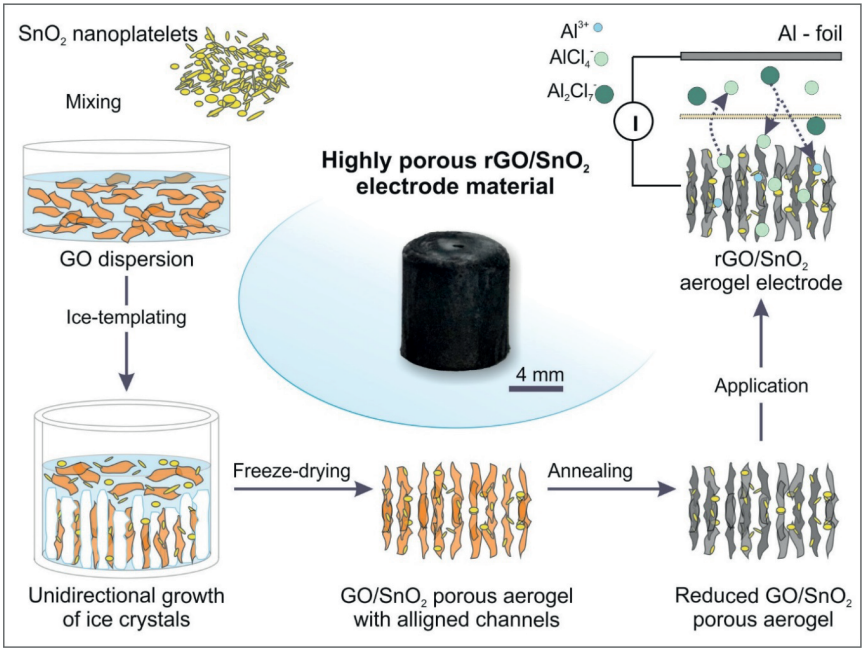

Figure 22. Schematic illustration of the fabrication process of the highly porous, free-standing electrode composed of SnO_2 and rGO.[134] Reproduced under the conditions of the Creative Commons Attribution (CC BY), Copyright © 2020 by the authors. Licensee MDPI, Basel, Switzerland

Similar to the fabrication of the SnO - crosses – PVP composite, the ice-templating technique leads to the formation of vertical channels along the applied temperature gradient (18 K mm^{-1}). During the growth of the unidirectional ice crystals, i.e. the movement of the crystallization front, the dispersed particles and GO sheets are located at the grain boundaries between the crystals. Thus, a negative of the ice crystals structure is obtained upon sublimation of the ice. In order to enhance the conductivity of graphene oxide, an annealing process analogous to the work done on paper like SnO_2/rGO composites[110] was conducted. As shown in **Figure 23**, a highly

porous structure with directed channels and a porosity estimated as 99.9 % was obtained in both the case of graphene and composite material. Thus, it could be proven, that the addition of SnO_2 particles do not have any influence on the microscopic structure of the porous composite. However, on a nanoscale, it becomes apparent, that the SnO_2 particles are embedded between rGO sheets and not grown on them, since no precursor but fully crystalline SnO_2 particles were used, compared to the work done on paper-like electrode.[110]

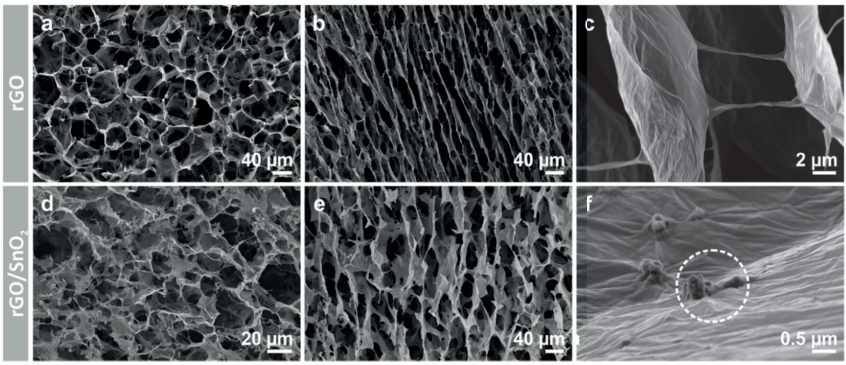

Figure 23. a) top-view on the channels in rGO and rGO/SnO_2 aerogels, b) a cross sections long the channel direction and c) a high magnification micrograph of the walls of the porous microstructure.[134] Reproduced under the conditions of the Creative Commons Attribution (CC BY), Copyright © 2020 by the authors. Licensee MDPI, Basel, Switzerland

This ice-templating technique has been applied to decrease the ion diffusion path and as such the tortuosity of the electrode by Ju *et al.*.[130] He and his coworkers were able to notably improve the electrode performance. The intricate structuring of VPO_4 nanosheets with conductive additive (Super P) and Binder (Carboxymethylcellulose-sodium) using ice-templating resulted in aligned channels, which enabled charging rates up to 10C and stable cyclic performance over 500 cycles with less than 20 % capacity for a Li ion based chemistry.

Similar to the natural sponges, the rGO/SnO_2 scaffold with a sponge-like structure exhibits an extraordinary mechanical performance with a full recovery after 75 % compression. A full recovery has been found as well in other graphene-based aerogels as shown by Zhu *et al.*[131] using a 3D printed graphene aerogel micro-lattice and Yang *et al.*[132] using a biomimetic aerogel obtained by bidirectional freeze drying. However, a compression and a full recovery after a 75 % compression as shown in case of the rGO and rGO composite in this case is exceptional, since both Zhu *et al.* and Yang *et al.* only were able to show a full recovery after a compression to 50 %. A detailed study on the deformation mechanism during compression shows, that the

collapse of the porous structure occurs not linearly, but small domains of the aerogel collapse sequentially.

In order to investigate a novel electrochemical system, the highly porous composite was tested as freestanding electrode in an aluminum-based half-cell. The intercalation of aluminum and aluminum chlorate ions requires large surfaces and high electronic conductivity.[90] Thus, to electrochemically test these electrodes as cathode in AIBs, the cells were assembled by directly soaking the electrodes in an ionic electrolyte containing Al^{3+} and $AlCl_4^-$. In comparison with denser, more common 2D electrodes,[133] the ion diffusion was enhanced and the diffusion path is highly shortened, which led to a direct adsorption or intercalation at the material's surface, due to the favorable porous microstructure. It could be shown that the hybrid electrodes exhibit electrochemical as well pseudocapacitive contributions, being beneficial for high capacities and fast charging coupled with good cycling stability. A cyclic voltammetry measurement showed, that both components, *i.e.* SnO_2 and rGO are electrochemically active and intercalation/adsorption occurs. Due to the synergy between pseudocapacitive effect (caused by the rGO) and intercalation (caused by the SnO_2), the aluminum ion-based chemistry coupled with the porous microstructure enables charging rates up to 20 C, which is compared to lithium ion-based systems (0.3 to 3 C) a significant enhancement.[11] At the current state-of-the-art anode material for Al Ion cells, no free-standing electrode containing SnO_2 has been tested with such success before. Wang *et al.*[83] was able to apply SnO_2 in an aluminum-based cell, however a slurry with a large amount of binder (10 wt%), carbon black (20 wt%) and inherent carbon coating of the SnO_2 particles (42.5 wt% carbon) lead to a large amount of inactive material, which is additionally coated onto pure Molybdenum foil. Thus, the applied slurry only (with inactive components included) has a capacity of roughly 55 mAh g^{-1}, which is similar to the capacity obtained for the highly porous aerogel. Taking the weight fraction of the molybdenum foil into account, the rGO/SnO_2 aerogel is far superior to the coated slurry presented in the work of Lu et al..[83]

1.5.4 Outlook

In conclusion, the aim of this thesis was the development of composite electrodes based on nature's design principles by uniting the extraordinary mechanical performance of biological microstructures with the electrochemical functionality of active materials used for ion intercalation. This could be achieved by developing binder-free electrodes composed of rGO and SnO_2, *i.e.* dense 2D paper-like electrode and 3D porous scaffolds, allowing to adjust the energy density as well as power density according to the intended application. It was shown, that the tailoring of the SnO_2 platelets and crosses can be easily achieved by means of changing the ammonia concentration in a hydrothermal synthesis. While the tailoring of the active materials phase and morphology provides new insights into the correlations between the inherent intercalation properties of a materials phase and the size and morphology of the particles itself, further experimental and simulation studies are needed to reveal the detailed effects on nano- and microscale.

Finally, these anisotropic active material particles where combined or embedded into a flexible backbone structure, mimicking the structure of nacre and sponges. Hereby, the advantages of such structures, such as the short ion diffusion path due to the large porosity and the mechanically stable backbone, become apparent. The mechanical stability of the developed bioinspired electrodes composed of SnO/SnO_2 and GO was achieved by following a bioinspired design principle and enabled their direct application as a free-standing electrode, without the addition of any binder or current collector. Moreover, these electrodes can be applied in different electrochemical systems, such as lithium and aluminum-based chemistries. This shows, that the application of such electrodes mimicking natures design is not solely limited to common lithium-based chemistry, but its principles can simply be adapted for multivalent metal ion batteries. However, further effort is required in the search for novel electrode materials, which support the intercalation of multivalent ions. Specifically, the embedding of such materials in a stable backbone structure and taking advantage of synergistic effects as shown in case of the highly porous SnO_2/rGO composite requires additional experimental studies. In order to increase the understanding of nanoscale effect and the interplay between active material and backbone structure, simulation of the structure and the intercalation kinetics might be a suitable tool.

1.6 References

1. Armand, M. & Tarascon, J.-M. Building better batteries. *Nature* **451**, 652–657 (2008).
2. Lu, L., Han, X., Li, J., Hua, J. & Ouyang, M. A review on the key issues for lithium-ion battery management in electric vehicles. *Journal of Power Sources* **226**, 272–288 (2013).
3. Marom, R., Francis Amalraj, S., Leifer, N., Jacob, D. & Aurbach, D. A review of advanced and practical lithium battery materials. *Journal of Materials Chemistry* **21**, 9938–9954 (2011).
4. *Handbuch Lithium-Ionen-Batterien*. (Springer Vieweg, 2013). doi:10.1007/978-3-642-30653-2.
5. May, G. J., Davidson, A. & Monahov, B. Lead batteries for utility energy storage: A review. *Journal of Energy Storage* **15**, 145–157 (2018).
6. Sun, H. *et al.* Hierarchical 3D electrodes for electrochemical energy storage. *Nature Reviews Materials* **4**, 45–60 (2019).
7. Manthiram, A. An Outlook on Lithium Ion Battery Technology. *ACS Cent. Sci.* **3**, 1063–1069 (2017).
8. Vlad, A., Singh, N., Galande, C. & Ajayan, P. M. Design Considerations for Unconventional Electrochemical Energy Storage Architectures. *Advanced Energy Materials* **5**, 1402115 (2015).
9. Yoshino, A., Sanechika, K. & Nakajima, T. Secondary battery. (1987).
10. Wang, C., Kakwan, I., Appleby, A. J. & Little, F. E. In situ investigation of electrochemical lithium intercalation into graphite powder. *Journal of Electroanalytical Chemistry* **489**, 55–67 (2000).
11. Nitta, N., Wu, F., Lee, J. T. & Yushin, G. Li-ion battery materials: present and future. *Materials Today* **18**, 252–264 (2015).

12. Daniel, C., Mohanty, D., Li, J. & Wood, D. L. Cathode materials review. *AIP Conference Proceedings* **1597**, 26–43 (2014).
13. Shao-Horn, Y., Croguennec, L., Delmas, C., Nelson, E. C. & O'Keefe, M. A. Atomic resolution of lithium ions in LiCoO 2. *Nature Materials* **2**, 464–467 (2003).
14. Xu, J., Dou, S., Liu, H. & Dai, L. Cathode materials for next generation lithium ion batteries. *Nano Energy* **2**, 439–442 (2013).
15. Belharouak, I., Sun, Y.-K., Liu, J. & Amine, K. Li(Ni1/3Co1/3Mn1/3)O2 as a suitable cathode for high power applications. *Journal of Power Sources* **123**, 247–252 (2003).
16. Li, W., Song, B. & Manthiram, A. High-voltage positive electrode materials for lithium-ion batteries. *Chem. Soc. Rev.* **46**, 3006–3059 (2017).
17. Shi, H. Coke vs. graphite as anodes for lithium-ion batteries. *Journal of Power Sources* **75**, 64–72 (1998).
18. Tomaszewska, A. *et al.* Lithium-ion battery fast charging: A review. *eTransportation* **1**, 100011 (2019).
19. Yuan, H. *et al.* Slurry-Coated Sulfur/Sulfide Cathode with Li Metal Anode for All-Solid-State Lithium-Sulfur Pouch Cells. *Batteries & Supercaps* **3**, 596–603 (2020).
20. Myung, S.-T., Hitoshi, Y. & Sun, Y.-K. Electrochemical behavior and passivation of current collectors in lithium-ion batteries. *Journal of Materials Chemistry* **21**, 9891–9911 (2011).
21. Aurbach, D. *et al.* Design of electrolyte solutions for Li and Li-ion batteries: a review. *Electrochimica Acta* **50**, 247–254 (2004).
22. Hayamizu, K. Temperature Dependence of Self-Diffusion Coefficients of Ions and Solvents in Ethylene Carbonate, Propylene Carbonate, and Diethyl Carbonate Single Solutions and Ethylene Carbonate + Diethyl Carbonate Binary Solutions of LiPF6 Studied by NMR. *J. Chem. Eng. Data* **57**, 2012–2017 (2012).

23. Evanoff, K. *et al.* Towards Ultrathick Battery Electrodes: Aligned Carbon Nanotube – Enabled Architecture. *Advanced Materials* **24**, 533–537 (2012).
24. Zhang, X. *et al.* Multiscale Understanding and Architecture Design of High Energy/Power Lithium-Ion Battery Electrodes. *Advanced Energy Materials* **11**, 2000808 (2021).
25. Fu, K. *et al.* Graphene Oxide-Based Electrode Inks for 3D-Printed Lithium-Ion Batteries. *Advanced Materials* **28**, 2587–2594 (2016).
26. Ma, F., Dai, X., Jin, J., Tie, N. & Dai, Y. Hierarchical core-shell hollow CoMoS4@Ni–Co–S nanotubes hybrid arrays as advanced electrode material for supercapacitors. *Electrochimica Acta* **331**, 135459 (2020).
27. Xia, X. *et al.* Generic Synthesis of Carbon Nanotube Branches on Metal Oxide Arrays Exhibiting Stable High-Rate and Long-Cycle Sodium-Ion Storage. *Small* **12**, 3048–3058 (2016).
28. Lee, J. H., Oh, S. H., Jeong, S. Y., Kang, Y. C. & Cho, J. S. Rattle-type porous Sn/C composite fibers with uniformly distributed nanovoids containing metallic Sn nanoparticles for high-performance anode materials in lithium-ion batteries. *Nanoscale* **10**, 21483–21491 (2018).
29. Cao, F.-F. *et al.* Cu-Si Nanocable Arrays as High-Rate Anode Materials for Lithium-Ion Batteries. *Advanced Materials* **23**, 4415–4420 (2011).
30. Wang, G. X. *et al.* Graphite–Tin composites as anode materials for lithium-ion batteries. *Journal of Power Sources* **97–98**, 211–215 (2001).
31. Zuo, X., Zhu, J., Müller-Buschbaum, P. & Cheng, Y.-J. Silicon based lithium-ion battery anodes: A chronicle perspective review. *Nano Energy* **31**, 113–143 (2017).
32. Hendricks, C., Williard, N., Mathew, S. & Pecht, M. A failure modes, mechanisms, and effects analysis (FMMEA) of lithium-ion batteries. *Journal of Power Sources* **297**, 113–120 (2015).

33. Arora, P., White, R. E. & Doyle, M. Capacity Fade Mechanisms and Side Reactions in Lithium-Ion Batteries. *J. Electrochem. Soc.* **145**, 3647 (1998).
34. Su, X. *et al.* Silicon-Based Nanomaterials for Lithium-Ion Batteries: A Review. *Advanced Energy Materials* **4**, 1300882 (2014).
35. Hwang, S. M. *et al.* A case study on fibrous porous SnO2 anode for robust, high-capacity lithium-ion batteries. *Nano Energy* **10**, 53–62 (2014).
36. Liu, H. *et al.* Flower-like SnO2/graphene composite for high-capacity lithium storage. *Applied Surface Science* **258**, 4917–4921 (2012).
37. Watson, J. The tin oxide gas sensor and its applications. *Sensors and Actuators* **5**, 29–42 (1984).
38. Lee, S.-C., Lee, J.-H., Oh, T.-S. & Kim, Y.-H. Fabrication of tin oxide film by sol–gel method for photovoltaic solar cell system. *Solar Energy Materials and Solar Cells* **75**, 481–487 (2003).
39. Mizuhashi, M. Electrical properties of vacuum-deposited indium oxide and indium tin oxide films. *Thin Solid Films* **70**, 91–100 (1980).
40. Cho, J. S. & Kang, Y. C. Nanofibers Comprising Yolk–Shell Sn@void@SnO/SnO2 and Hollow SnO/SnO2 and SnO2 Nanospheres via the Kirkendall Diffusion Effect and Their Electrochemical Properties. *Small* **11**, 4673–4681 (2015).
41. Baur, W. H. Über die Verfeinerung der Kristallstrukturbestimmung einiger Vertreter des Rutiltyps: TiO2, SnO2, GeO2 und MgF2. *Acta Cryst* **9**, 515–520 (1956).
42. Batzill, M. & Diebold, U. The surface and materials science of tin oxide. *Progress in Surface Science* **79**, 47–154 (2005).
43. Cheng, Y., Nie, A., Gan, L.-Y., Zhang, Q. & Schwingenschlögl, U. A global view of the phase transitions of SnO2 in rechargeable batteries based on results of high throughput calculations. *J. Mater. Chem. A* **3**, 19483–19489 (2015).

44. Nam, K. *et al.* Study on the mechanical properties of porous tin oxide. *Ceramics International* **43**, 10913–10918 (2017).

45. Heubner, C. *et al.* Scalable Fabrication of Nanostructured Tin Oxide Anodes for High-Energy Lithium-Ion Batteries. *ACS Appl. Mater. Interfaces* **10**, 27019–27029 (2018).

46. Zoller, F., Böhm, D., Bein, T. & Fattakhova-Rohlfing, D. Tin Oxide Based Nanomaterials and Their Application as Anodes in Lithium-Ion Batteries and Beyond. *ChemSusChem* **12**, 4140–4159 (2019).

47. Zhu, J., Yang, D., Yin, Z., Yan, Q. & Zhang, H. Graphene and Graphene-Based Materials for Energy Storage Applications. *Small* **10**, 3480–3498 (2014).

48. Xu, C., Sun, J. & Gao, L. Direct growth of monodisperse SnO2 nanorods on graphene as high capacity anode materials for lithium ion batteries. *J. Mater. Chem.* **22**, 975–979 (2011).

49. Allen, M. J., Tung, V. C. & Kaner, R. B. Honeycomb Carbon: A Review of Graphene. *Chem. Rev.* **110**, 132–145 (2010).

50. Choi, W., Lahiri, I., Seelaboyina, R. & Kang, Y. S. Synthesis of Graphene and Its Applications: A Review. *Critical Reviews in Solid State and Materials Sciences* **35**, 52–71 (2010).

51. Young, R. J., Kinloch, I. A., Gong, L. & Novoselov, K. S. The mechanics of graphene nanocomposites: A review. *Composites Science and Technology* **72**, 1459–1476 (2012).

52. William S., H. & Richard E., O. Preparation of Graphitic Oxide | Journal of the American Chemical Society. https://pubs.acs.org/doi/abs/10.1021/ja01539a017 (1957).

53. Sengupta, I., Chakraborty, S., Talukdar, M., Pal, S. K. & Chakraborty, S. Thermal reduction of graphene oxide: How temperature influences purity. *Journal of Materials Research* **33**, 4113–4122 (2018).

54. Park, S. *et al.* Hydrazine-reduction of graphite- and graphene oxide. *Carbon* **49**, 3019–3023 (2011).

55. Agarwal, V. & Zetterlund, P. B. Strategies for reduction of graphene oxide – A comprehensive review. *Chemical Engineering Journal* **405**, 127018 (2021).

56. Tarcan, R. *et al.* Reduced graphene oxide today. *J. Mater. Chem. C* **8**, 1198–1224 (2020).

57. Tung, V. C., Allen, M. J., Yang, Y. & Kaner, R. B. High-throughput solution processing of large-scale graphene. *Nature Nanotechnology* **4**, 25–29 (2009).

58. Lee, C., Wei, X., Kysar, J. W. & Hone, J. Measurement of the Elastic Properties and Intrinsic Strength of Monolayer Graphene. *Science* **321**, 385–388 (2008).

59. Yoo, E. *et al.* Large Reversible Li Storage of Graphene Nanosheet Families for Use in Rechargeable Lithium Ion Batteries. *Nano Lett.* **8**, 2277–2282 (2008).

60. Wu, Z.-S., Ren, W., Xu, L., Li, F. & Cheng, H.-M. Doped Graphene Sheets As Anode Materials with Superhigh Rate and Large Capacity for Lithium Ion Batteries. *ACS Nano* **5**, 5463–5471 (2011).

61. Ponrouch, A. *et al.* Multivalent rechargeable batteries. *Energy Storage Materials* **20**, 253–262 (2019).

62. Nie, P. *et al.* Flower-like LiMnPO 4 hierarchical microstructures assembled from single-crystalline nanosheets for lithium-ion batteries. *CrystEngComm* **14**, 4284–4288 (2012).

63. Gao, H. *et al.* Revealing the Rate-Limiting Li-Ion Diffusion Pathway in Ultrathick Electrodes for Li-Ion Batteries. *J. Phys. Chem. Lett.* **9**, 5100–5104 (2018).

64. Jin, S., Jiang, Y., Ji, H. & Yu, Y. Advanced 3D Current Collectors for Lithium-Based Batteries. *Advanced Materials* **30**, 1802014 (2018).

65. Li, N., Chen, Z., Ren, W., Li, F. & Cheng, H.-M. Flexible graphene-based lithium ion batteries with ultrafast charge and discharge rates. *PNAS* **109**, 17360–17365 (2012).

66. Acik, M. *et al.* The Role of Oxygen during Thermal Reduction of Graphene Oxide Studied by Infrared Absorption Spectroscopy. *J. Phys. Chem. C* **115**, 19761–19781 (2011).
67. Wang, J.-Z., Zhong, C., Chou, S.-L. & Liu, H.-K. Flexible free-standing graphene-silicon composite film for lithium-ion batteries. *Electrochemistry Communications* **12**, 1467–1470 (2010).
68. Liang, J., Zhao, Y., Guo, L. & Li, L. Flexible Free-Standing Graphene/SnO2 Nanocomposites Paper for Li-Ion Battery. *ACS Appl. Mater. Interfaces* **4**, 5742–5748 (2012).
69. Hu, T. *et al.* Flexible free-standing graphene–TiO2 hybrid paper for use as lithium ion battery anode materials. *Carbon* **51**, 322–326 (2013).
70. Liu, Y., Cai, X. & Shi, W. Free-standing graphene/carbon nanotubes/CuO aerogel paper anode for lithium ion batteries. *Materials Letters* **172**, 72–75 (2016).
71. Ramanathan, T. *et al.* Functionalized graphene sheets for polymer nanocomposites. *Nature Nanotechnology* **3**, 327–331 (2008).
72. Bouibed, A., Doufnoune, R. & Ponçot, M. An easy and innovative one-step *in situ* synthesis strategy of silica nanoparticles decorated by graphene oxide particles through covalent linkages. *Mater. Res. Express* (2020) doi:10.1088/2053-1591/ab6800.
73. Haldorai, Y. *et al.* Facile synthesis of α-MnO2 nanorod/graphene nanocomposite paper electrodes using a 3D precursor for supercapacitors and sensing platform to detect 4-nitrophenol. *Electrochimica Acta* **222**, 717–727 (2016).
74. Bai, S. & Shen, X. Graphene –inorganic nanocomposites. *RSC Advances* **2**, 64–98 (2012).
75. *Behaviour of Lithium-Ion Batteries in Electric Vehicles: Battery Health, Performance, Safety, and Cost*. (Springer International Publishing, 2018). doi:10.1007/978-3-319-69950-9.
76. Liang, Y., Dong, H., Aurbach, D. & Yao, Y. Current status and future directions of multivalent metal-ion batteries. *Nature Energy* **5**, 646–656 (2020).

77. Li, Y., Lu, Y., Adelhelm, P., Titirici, M.-M. & Hu, Y.-S. Intercalation chemistry of graphite: alkali metal ions and beyond. *Chemical Society Reviews* **48**, 4655–4687 (2019).
78. Park, J. *et al.* Stable and High-Power Calcium-Ion Batteries Enabled by Calcium Intercalation into Graphite. *Advanced Materials* **32**, 1904411 (2020).
79. Li, M. *et al.* Design strategies for nonaqueous multivalent-ion and monovalent-ion battery anodes. *Nature Reviews Materials* **5**, 276–294 (2020).
80. Xu, Y., Zhu, Y., Liu, Y. & Wang, C. Electrochemical Performance of Porous Carbon/Tin Composite Anodes for Sodium-Ion and Lithium-Ion Batteries. *Advanced Energy Materials* **3**, 128–133 (2013).
81. Li, D. *et al.* Amorphous carbon coated SnO2 nanohseets on hard carbon hollow spheres to boost potassium storage with high surface capacitive contributions. *Journal of Colloid and Interface Science* **574**, 174–181 (2020).
82. Suo, G. *et al.* SnO2 nanosheets grown on stainless steel mesh as a binder free anode for potassium ion batteries. *Journal of Electroanalytical Chemistry* **833**, 113–118 (2019).
83. Lu, H. *et al.* A high performance SnO2/C nanocomposite cathode for aluminum-ion batteries. *J. Mater. Chem. A* **7**, 7213–7220 (2019).
84. Singh, N., S. Arthur, T., Ling, C., Matsui, M. & Mizuno, F. A high energy-density tin anode for rechargeable magnesium-ion batteries. *Chemical Communications* **49**, 149–151 (2013).
85. Arthur, T. S., Singh, N. & Matsui, M. Electrodeposited Bi, Sb and Bi1-xSbx alloys as anodes for Mg-ion batteries. *Electrochemistry Communications* **16**, 103–106 (2012).
86. Tan, Y.-H. *et al.* High Voltage Magnesium-ion Battery Enabled by Nanocluster Mg3Bi2 Alloy Anode in Noncorrosive Electrolyte. *ACS Nano* **12**, 5856–5865 (2018).
87. Zhang, X. *et al.* Rechargeable ultrahigh-capacity tellurium–aluminum batteries. *Energy & Environmental Science* **12**, 1918–1927 (2019).

88. Zhang, X. *et al.* Flower-like Vanadium Suflide/Reduced Graphene Oxide Composite: An Energy Storage Material for Aluminum-Ion Batteries. *ChemSusChem* **11**, 709–715 (2018).
89. Li, Z., Liu, J., Niu, B., Li, J. & Kang, F. A Novel Graphite–Graphite Dual Ion Battery Using an AlCl3–[EMIm]Cl Liquid Electrolyte. *Small* **14**, 1800745 (2018).
90. Elia, G. A. *et al.* An Overview and Future Perspectives of Aluminum Batteries. *Advanced Materials* **28**, 7564–7579 (2016).
91. Wang, D.-Y. *et al.* Advanced rechargeable aluminium ion battery with a high-quality natural graphite cathode. *Nat Commun* **8**, 1–7 (2017).
92. Zhang, Q. *et al.* Low-temperature synthesis of edge-rich graphene paper for high-performance aluminum batteries. *Energy Storage Materials* **15**, 361–367 (2018).
93. Lin, M.-C. *et al.* An ultrafast rechargeable aluminium-ion battery. *Nature* **520**, 324–328 (2015).
94. Leisegang, T. *et al.* The Aluminum-Ion Battery: A Sustainable and Seminal Concept? *Front. Chem.* **7**, (2019).
95. Whitesides, G. M. Bioinspiration: something for everyone. *Interface Focus* **5**, 20150031 (2015).
96. Lepora, N. F., Verschure, P. & Prescott, T. J. The state of the art in biomimetics. *Bioinspir. Biomim.* **8**, 013001 (2013).
97. Sun, J. & Bhushan, B. Hierarchical structure and mechanical properties of nacre: a review. *RSC Advances* **2**, 7617–7632 (2012).
98. Klautau, M. & Valentine, C. Revision of the genus Clathrina (Porifera, Calcarea). *Zool J Linn Soc* **139**, 1–62 (2003).
99. Nudelman, F. Nacre biomineralisation: A review on the mechanisms of crystal nucleation. *Seminars in Cell & Developmental Biology* **46**, 2–10 (2015).

100. Lowenstam, H. A., Lowenstam, P. E. D. of G. and P. S. H. a, Weiner, S. & Weiner, A. P. I. D. S. *On Biomineralization*. (Oxford University Press, 1989).

101. Schiel, D. R. & Welden, B. C. Responses to predators of cultured and wild red abalone, Haliotis rufescens, in laboratory experiments. *Aquaculture* **60**, 173–188 (1987).

102. Garcia-Esquivel, Z. & Felbeck, H. Activity of digestive enzymes along the gut of juvenile red abalone, Haliotis rufescens, fed natural and balanced diets. *Aquaculture* **261**, 615–625 (2006).

103. Gilbert, P. U. P. A. *et al.* Gradual Ordering in Red Abalone Nacre. *J. Am. Chem. Soc.* **130**, 17519–17527 (2008).

104. Wegst, U. G. K., Bai, H., Saiz, E., Tomsia, A. P. & Ritchie, R. O. Bioinspired structural materials. *Nature Materials* **14**, 23–36 (2015).

105. Levi-Kalisman, Y., Falini, G., Addadi, L. & Weiner, S. Structure of the nacreous organic matrix of a bivalve mollusk shell examined in the hydrated state using cryo-TEM. *J Struct Biol* **135**, 8–17 (2001).

106. Meyers, M. A., Lin, A. Y.-M., Chen, P.-Y. & Muyco, J. Mechanical strength of abalone nacre: Role of the soft organic layer. *Journal of the Mechanical Behavior of Biomedical Materials* **1**, 76–85 (2008).

107. Sarikaya, M. An introduction to biomimetics: A structural viewpoint. *Microscopy Research and Technique* **27**, 360–375 (1994).

108. Corni, I. *et al.* A review of experimental techniques to produce a nacre-like structure. *Bioinspir. Biomim.* **7**, 031001 (2012).

109. Burghard, Z. *et al.* Nanomechanical Properties of Bioinspired Organic–Inorganic Composite Films. *Advanced Materials* **19**, 970–974 (2007).

110. Jahnke, T. *et al.* Coalescence in Hybrid Materials: The Key to High-Capacity Electrodes. *ACS Appl. Energy Mater.* **1**, 7085–7092 (2018).

111. Soest, R. W. M. V. *et al.* Global Diversity of Sponges (Porifera). *PLOS ONE* **7**, e35105 (2012).

112. Sethmann, I. & Wörheide, G. Structure and composition of calcareous sponge spicules: A review and comparison to structurally related biominerals. *Micron* **39**, 209–228 (2008).

113. Jahnke, T. *et al.* Bioinspired synthesis of SnO crosses as backbone in artificial sponges. *Philosophical Transactions of the Royal Society A: Mathematical, Physical and Engineering Sciences* **377**, 20190130 (2019).

114. Sethmann, I., Hinrichs, R., Wörheide, G. & Putnis, A. Nano-cluster composite structure of calcitic sponge spicules—A case study of basic characteristics of biominerals. *Journal of Inorganic Biochemistry* **100**, 88–96 (2006).

115. Travis, D. F. The Comparative Ultrastructure and Organization of Five Calcified Tissues. in *Biological Calcification: Cellular and Molecular Aspects* (ed. Schraer, H.) 203–311 (Springer US, 1970). doi:10.1007/978-1-4684-8485-4_5.

116. Aizenberg, J., Ilan, M., Weiner, S. & Addadi, L. Intracrystalline Macromolecules are Involved in the Morphogenesis of Calcitic Sponge Spicules. *Connective Tissue Research* **34**, 255–261 (1996).

117. Ledger, P. W. & Jones, W. C. Spicule formation in the calcareous sponge Sycon ciliatum. *Cell Tissue Res.* **181**, 553–567 (1977).

118. Deville, S. Ice-Templating and Freeze-Casting: Control of the Processes, Microstructures, and Architectures. in *Freezing Colloids: Observations, Principles, Control, and Use: Applications in Materials Science, Life Science, Earth Science, Food Science, and Engineering* (ed. Deville, S.) 351–438 (Springer International Publishing, 2017). doi:10.1007/978-3-319-50515-2_6.

119. Zhang, H. *Ice Templating and Freeze-Drying for Porous Materials and Their Applications*. (John Wiley & Sons, 2018).

120. Deville, S. *et al.* In Situ X-Ray Radiography and Tomography Observations of the Solidification of Aqueous Alumina Particle Suspensions—Part I: Initial Instants. *Journal of the American Ceramic Society* **92**, 2489–2496 (2009).

121. Deville, S. Ice-templating, freeze casting: Beyond materials processing. *Journal of Materials Research* **28**, 2202–2219 (2013).

122. Huang, C. & S. Grant, P. Coral-like directional porosity lithium ion battery cathodes by ice templating. *Journal of Materials Chemistry A* **6**, 14689–14699 (2018).

123. Zhao, Z. *et al.* Sandwich, Vertical-Channeled Thick Electrodes with High Rate and Cycle Performance. *Advanced Functional Materials* **29**, 1809196 (2019).

124. Estevez, L., Kelarakis, A., Gong, Q., Da'as, E. H. & Giannelis, E. P. Multifunctional Graphene/Platinum/Nafion Hybrids via Ice Templating. *J. Am. Chem. Soc.* **133**, 6122–6125 (2011).

125. Bhauriyal, P., Bhattacharyya, G., Rawat, K. S. & Pathak, B. Graphene/hBN Heterostructures as High-Capacity Cathodes with High Voltage for Next-Generation Aluminum Batteries. *J. Phys. Chem. C* **123**, 3959–3967 (2019).

126. Medhekar, N. V., Ramasubramaniam, A., Ruoff, R. S. & Shenoy, V. B. Hydrogen Bond Networks in Graphene Oxide Composite Paper: Structure and Mechanical Properties. *ACS Nano* **4**, 2300–2306 (2010).

127. Wang, C. *et al.* Ultrathin SnO2 Nanosheets: Oriented Attachment Mechanism, Nonstoichiometric Defects, and Enhanced Lithium-Ion Battery Performances. *J. Phys. Chem. C* **116**, 4000–4011 (2012).

128. Cai, T. *et al.* Stable CoSe2/carbon nanodice@reduced graphene oxide composites for high-performance rechargeable aluminum-ion batteries. *Energy Environ. Sci.* **11**, 2341–2347 (2018).

129. Zhao, Y. *et al.* Significant impact of 2D graphene nanosheets on large volume change tin-based anodes in lithium-ion batteries: A review. *Journal of Power Sources* **274**, 869–884 (2015).

130. Ju, Z. *et al.* Understanding Thickness-Dependent Transport Kinetics in Nanosheet-Based Battery Electrodes. *Chem. Mater.* **32**, 1684–1692 (2020).

131. Zhu, C. *et al.* Highly compressible 3D periodic graphene aerogel microlattices. *Nat Commun* **6**, 1–8 (2015).

132. Yang, M. *et al.* Biomimetic Architectured Graphene Aerogel with Exceptional Strength and Resilience. *ACS Nano* **11**, 6817–6824 (2017).

133. Wang, S. *et al.* A Novel Aluminum-Ion Battery: Al/AlCl3-[EMIm]Cl/Ni3S2@Graphene. *Advanced Energy Materials* **6**, 1600137 (2016).

134. Jahnke, T. et al, Highly Porous Free-standing rGO/SnO2 Pseudocapacitive Cathodes for High-Rate and Long-Cycling Al-ion Batteries, Nanomaterials 10, 10,

2. Bioinspired Synthesis of SnO Crosses as Backbone in Artificial Sponges

(Reprinted with permission of the Royal Society.)

Timotheus Jahnke, Stefan Kilper, Andrea Knöller, Franz Brümmer, Marc Widenmeyer, Dirk Rothenstein, Zaklina Burghard, Joachim Bill*

Abstract

The distinct electronic properties, including p-type semiconducting and a wide optical band gap, renders SnO suitable for applications such as semiconductors, gas sensors or electrodes. However, the synthesis of SnO is rather challenging due to the instability of the oxide, which is usually obtained as a byproduct of the SnO_2 fabrication. In this work, we developed a bioinspired synthesis, based on a hydrothermal approach, for direct production of SnO nanoparticles. In this case, the amount of mineralizer was identified, which supports a template-free formation of the nanosized SnO particles at low temperature and mild chemical conditions. Moreover, the SnO nanoparticles exhibit a form of unique 3D crosses similar to the calcite crosses present in the calcerous sponge. We demonstrated that SnO crosses can be evenly distributed and embedded in an organic scaffold by an ice-templating approach in this way closely mimic the structure of calcerous sponge. Such scaffolds, reinforced by an active material, here SnO, could be used as filters, sensors or electrodes, where a high surface area and good accessibility are essential.

2.1 Introduction

Binary metal oxides, such as tin oxide (SnO), are widely used as semiconductors and gas sensors, due to their distinct electronic properties.[1–4] For example, it can be used as a leakage sensor

for inflammable gases.[5,6] Furthermore, SnO is suitable for applications as p-type semiconductor, such as microelectronic devices.[1,7]

Recently, researchers have shown an increased interest in SnO as anode material for novel metal ion batteries[8,9] due to its large gravimetric capacity.[8,10] For all these applications, a high surface area plays a crucial role,[11–13] which can be achieved by fabricating nanosized SnO of various shapes, such as flowers,[14] plates[15] or thin films. However, a major drawback of using such small structures with a high surface area is that they often tend to uncontrollable agglomerate *via* strong van der Waals interactions. To cope with this issue, one plausible approach would be 3D nanostructuring of the oxide particles, which is a rather challenging task. Furthermore, for their applications, like sensor or filters, it is important to make them independently available. The use of a highly porous scaffolds as matrix, where such particles are separated and evenly distributed would be one option, however, another challenging task.

Some biological organisms already mastered such challenging tasks by controlling the formation, structure and morphology of the inorganic materials they are composed.[30] For example, calcium carbonate ($CaCO_3$) exists in the shape of aragonite fibers in cuttlebone[16] or platelets in nacre[17] as well as in the shape of calcite or aragonite cross-like spicules in calcareous sponges.[18] Such variety is the result of utilizing different structuring agents,[18,19] which selectively guide the mineralization of the $CaCO_3$ into the desired shapes. In particular, the calcareous sponge (**Figure 1a,b**) consists of a calcite network structure (**Figure 1c),** in which cross-like spicules are uniformly distributed as displayed in high magnification scanning electron microscope (SEM) micrograph (**Figure 1d**). The species shown, *Clathrina clathrus* (Clathrinidae, Calcarea, Porifera) is a common species in the Mediterranean and Adriatic Seas and is found attached to rocky substrates. Colour in vivo is yellow, a “beautiful sulphur yellow colour”.[20] The clathroid corpus is composed of irregularly and loosely anastomosed tubes and large superficial water-collecting tubes were observed (**Figure 1b**). The mineral skeleton is composed entirely of calcium carbonate and composed of equiradiate and equiangular, cylindrical triactines only (**Figure 1c,d**).[20,21] These spicules serve as mechanical backbone of the channel-like superstructures, which are important for the sponge to filter micro plankton from the seawater.[22] Therefore, the sponge holds an optimized balance between mechanical stability and accessibility, which is likewise desired in the abovementioned SnO-based applications.

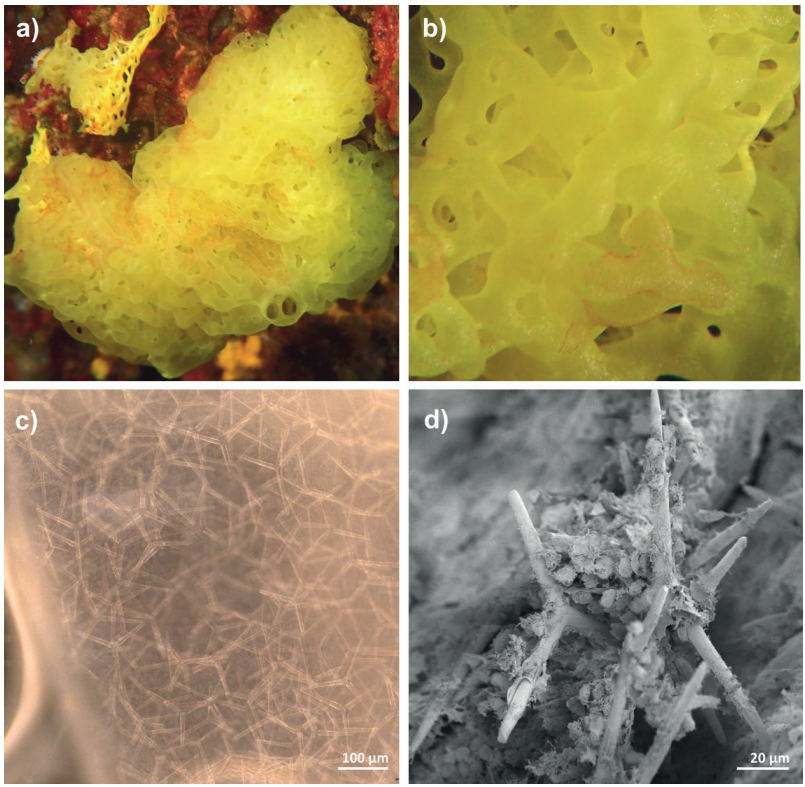

Figure 1: a) Digital image (width corresponds to 6 cm) of the sponge *Cl. Clathrus* as living organism with b) a magnification of its structure. c) Dark-field microscope image of a calcareous sponge presenting the spicules, which are randomly distributed in the organic network and d) highly magnified SEM micrograph reveals the cross-like structure of the single spicules.

While nature optimized the mineralization of $CaCO_3$ over millions of years, transferring the calcareous sponges' structural features to technologically relevant materials requires the development of a novel synthesis protocol, which involves an adequate substitute for the structuring agent, thus mineralizer. One promising bioinspired approach is based on a hydrothermal method, which has a high yield, rendering it suitable for large-scale applications. However, its reaction rate and the product are highly sensitive to a large number of parameters, including humidity, temperature and local concentration differences. Synthesizing a defined nanostructured material therefore require an exact parameter control. To date, mostly metal oxides, such as TiO_2,[23] ZnO,[24] ZrO_2,[25] have been intensively investigated, but far too little

attention has been paid to the investigation of the formation of SnO. This is because it is only used to be considered as an undesired byproduct in the synthesis of SnO_2. In this respect, Wang *et al*. investigated the fabrication of SnO_2 nanosheets, using tin chloride ($SnCl_2$) salts as precursor.[26] They found that in this process, divalent $SnCl_2$ is oxidized over several intermediate oxide states to the four valent Sn in SnO_2 and they established a corresponding mechanism, which is based on the oriented attachment of nanoparticles into nanosheets. In addition, they found that the intricate formation of SnO_2 nanosheets is a function the oxygen content in the autoclave during the oxidation. Accordingly, a lack of oxygen leads to the formation of the unwanted SnO byproduct.

This study turns the initially unwanted byproduct into desired well-defined and functional nanostructures by controlling the crucial parameters responsible for phase and morphology during the hydrothermal synthesis. We identified the parameters, which are responsible for the formation of the SnO in the form of 3D nanostructured crosses. The resulting SnO crosses can further be combined with polymers, such as polyvinylpyrrolidone (PVP) in an ice-templating approach, yielding microstructures comparable to the ones of the calcareous sponges. Such bioinspiration enable the fabrication of functional hybrid materials, which are promising for application as sensors, filters and super capacitors, which require a high surface area and accessibility paired with good mechanical stability.

2.2 Controlling the Hydrothermal Synthesis

In a common experiment, SnO_2 is synthesized by dissolving $SnCl_2 \cdot 2\ H_2O$ in a ration 1:1 water to ethanol. This mixture is supplemented by the addition of a defined amount of aqueous ammonia as a mineralizer[34] in an autoclave at room temperature. According to Wang *et al*., a partial oxidation of the tin (II) cations occurs, subsequently leading to the formation of SnO_2 *via* the hydroxylated intermediate phase $Sn_6(OH)_4O_4$, as schematically depicted in **Figure 2** (high $Sn(II)/NH_3$ ratio). Initially indicated, the oxygen content is crucial for the formation of SnO_2. When enough oxygen is accessible, the tin salt precursor ($SnCl_2 \cdot 2\ H_2O$) is fully oxidized, forming stoichiometric SnO_2. However, when reducing the amount of oxygen in the autoclave, non-stoichiometric SnO_{2-x} is obtained.[27] Therefore, in order to favor the formation of SnO, excess of oxygen in the chemical autoclave has to be eliminated.

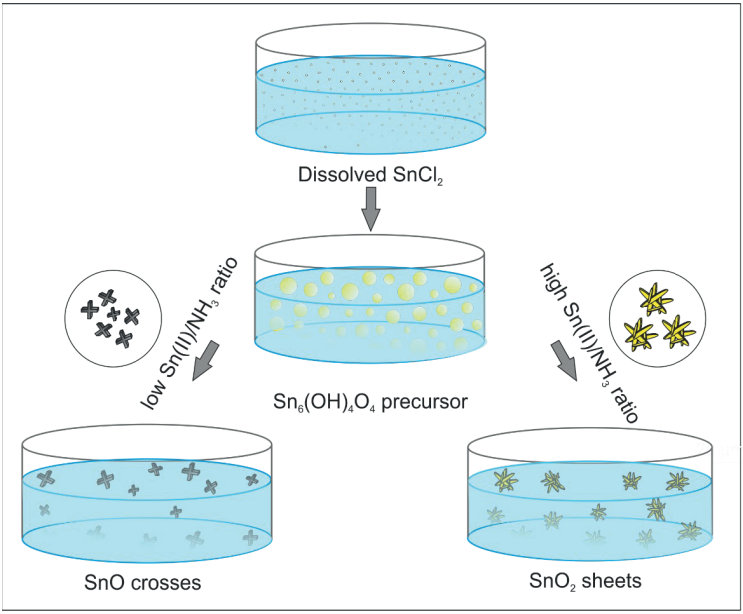

Figure 2: Schematic illustration of the preparation process of SnO_x nanostructures based on hydrothermal approach with high and low Sn(II)/NH_3 ratios.

To analyze the formation of the SnO_x nanostructures in detail, an extended systematic study of the hydrothermal process was carried out. In the first attempt, we varied the reaction time, which allowed to get a deeper insight into the crystallization mechanism of oxygen deficient SnO_{2-x}. It should be noted that the influence of atmospheric oxygen was excluded by leaving no residual atmosphere in the autoclave, displayed in **Supplementary Figure S1.** However, although the influence of atmospheric oxygen was eliminated, SnO_2 was formed *via* the hydroxylated state $Sn_6(OH)_4O_4$ as indicated in the powder X-ray diffraction (PXRD) pattern in **Figure 3a**. At a reaction time of 30 min to 1 h, under hydrothermal conditions, crystalline $Sn_6(OH)_4O_4$ was present. Furthermore, after a reaction time of 2 h, new broader reflections arose, which fit well to the simulated pattern of SnO_2 (ICSD Card Nr. 9163), whilst the reflections observed before for $Sn_6(OH)_4O_4$ disappeared. Taking into account the full width at half maximum (FWHM) of the reflections, the SnO_2 seems to consist of smaller crystallites than the intermediate phase, whereas the majority of the phase is amorphous. Nonetheless, with

proceeding reaction time, the reflection peaks become sharper, indicating crystal growth of the SnO_2.

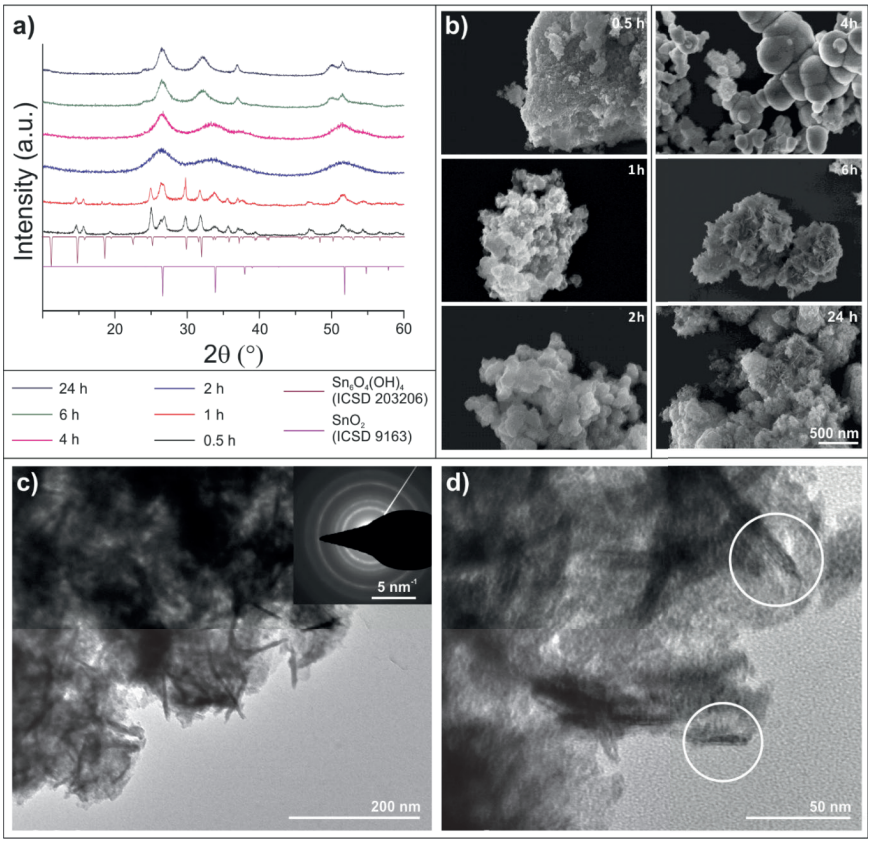

Figure 3: a) PXRD pattern of the obtained SnO_x product and its corresponding morphology in a SEM micrograph as a function of reaction time. The respective reaction time shown in the top left corner corresponds to the point where the reaction was interrupted by removing the autoclave from the furnace. A corresponding TEM micrograph to a time of 6 h is displayed in c) as an overview with its corresponding selected area diffraction pattern displayed as inset, and in d) a high magnification micrograph is presented. The white circles indicate crystalline needle-shaped particles.

Besides the change in phase indicted from PXRD data, corresponding SEM micrographs (**Figure 3b**) provide information about the evolution of the material's morphology. By comparison of the micrographs it can be concluded that initially, crystals of $Sn_6(OH)_4O_4$ are present, which then convert into predominantly amorphous particles after 2 to 4 h. A reaction time of 6 h finally shows enhanced crystallinity, which becomes even more pronounced after 24 h. In addition, it can be seen that all these nanoparticles form secondary particles in the micrometer range agglomerates. This agglomeration most likely occurs during washing and drying of the product due to strong surface interactions. To find out the structure and crystallinity of the primary particles, a closer inspection of such a secondary particle was carried out by transmission electron microscopy (TEM). **Figure 3c** displays that needle-like shapes are present, which indicates that anisotropic growth takes place after 6 h of the reaction time. Their crystalline structure is visible on higher magnification TEM image, as marked by white circles in **Figure 3d**. The inset of the diffraction pattern in **Figure 3c** is in agreement with the diffraction pattern obtained using PXRD in **Figure 3a**. Additionally, it indicates the presence of an amorphous phase, due to the strong diffuse scattering of the primary beam, observed on the sides of the beam stopper. A corresponding Raman investigation is available in **Supplementary Figure S2**.

As the part of the phase (6h) is amorphous, phase purity was verified by chemical analysis. Inductive coupled plasma - optical emission spectroscopy (ICP-OES) and combustion analysis was used to determine the amount of tin, oxygen and hydrogen. We found a chemical composition of 74.9 ± 0.8 wt.% tin, 24.1 ± 0.3 wt.% oxygen and 0.53 ± 0.01 wt.% hydrogen. This composition does not suit to stoichiometric SnO_2, therefore it is assumed that a phase mixture of SnO_2 and $Sn_6(OH)_4O_4$ are coexisting, analog to the observations of Wang *et al*..[26] This is further supported when taking a closer look at the diffractions pattern obtained for reaction times longer than 6 h (**Figure 3a**). A slight shift of the reflections $2\vartheta = 33°$ and $2\vartheta = 37°$ is observed indicating the presence of the crystallized precursor phase $Sn_6(OH)_4O_4$.Wang *et al*.[26] reported that 13 % of the Sn(II) cations were not oxidized to Sn(IV) cations because of the lack of oxygen present in the autoclave, yielding SnO_{2-x} nanosheets. In contrast, in our case it appeared that by adjusting the filling level of the autoclave and excluding the influence of any residual oxygen, we were able to increase the amount of Sn(II) in a way that the precursor phase is still present after reaction in the final product, guiding the path towards SnO.

Recently, it was found that single atomic layers of SnO can be synthesized on top of a carbon cloth by a hydrothermal method, whereas the presence of ammonia (or urea) appeared to impeded the oxidation of Sn(II) to Sn(IV)[8]. We hypothesized that by adjusting the Sn(II)/NH_3 ratio, a further stabilization of Sn(II) can be achieved, yielding stable SnO. Therefore, in the second attempt of parameter study, the focus was set on the amount of ammonia, which serves as mineralizer, while keeping the reaction time constant at 6 h. The reaction time of 6h was chosen because no changes were observed after a reaction time of 6 h (see **Figure 3a**). In general, the reaction sequence from $SnCl_2$ to SnO *via* the intermediate formation of $Sn_6(OH)_4O_4$ can be expressed by equation [1] and [2], involving ammonia as weak reducing agent.

$$6\ SnCl_2 + 12\ NH_4OH \xrightarrow{RT} Sn_6(OH)_4O_4 + 12\ NH_4Cl + 4\ H_2O \quad [1]$$

$$Sn_6(OH)_4O_4 \xrightarrow{\Delta T} 6\ SnO + 2H_2O \quad [2]$$

In order to confirm the hypothesis, different tin chloride and ammonia ratios, thus Sn(II)/NH_3 ratios, were investigated, as listed in **Supplementary Table S1**. The structure of these products fabricated by different ratios was investigated using PXRD. The recorded pattern of the ratios 2.2 to 0.5 mainly showed the presence of nanocrystalline SnO_2 (**Figure 4a**). However, after further decreasing the ratio, meaning adding more ammonia, a drastic change in the PXRD pattern was obtained. In contrast to our expectations, the new arising sharp peaks indicate a crystalline material, which can be entirely matched with the simulated pattern of SnO (ICSD CARD Nr. 15516).

Analog to the previous attempt, the products were structurally investigated by SEM, as displayed in **Figure 4b**. It can be seen, that an assembly of nanoparticles to larger agglomerates for the high Sn(II)/NH_3 (ratio 1.11) ratios is present. Decreasing the ratio lead to the formation of nanosheets (ratio 0.55), similar to the nanosheets observed in **Figure 3b**. Importantly, it can be seen that a further decrease in the Sn(II)/NH_3 ratio to 0.37 finally supported the formation of SnO crosses.

The first reported SnO crosses were produced by thermal decomposition at 310 °C of tetraphenyltin,[28] which require significantly more energy than our synthesis approach (120 °C *vs* 310 °C),[8,28] highlighting the advantage of ammonia as structuring agent for the fabrication of such crosses. Furthermore, they investigated in detail the crystal formation and found, that

an initial core is formed upon decomposition with an intersection on the (112) plane. According to the results from the PXRD study of our products (**Figure 4a**), the intensity ratio of the reflections at 2ϑ = 19.3° and 2ϑ = 37.1° of samples obtained from ratio 0.37 deviated from the simulated pattern. This indicates the presence of a preferred growth along the (1-10) and (112) planes, in accordance to Xu *et al.*.[28] Upon further decreasing the Sn(II)/NH_3 ratio, the intensity ratio approaches the one of the simulated pattern of SnO (ICSD 15516), letting the texturing vanish, indicating further isotropic growth of the SnO – structures, resulting in thicker crosses (**Figure 4b**). Additionally, we have included a Raman investigation as **Supplementary Figure S3**.

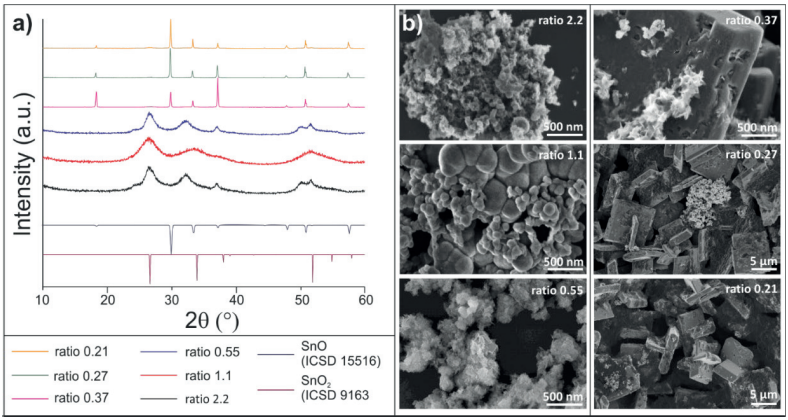

Figure 4: a) PXRD pattern of the obtained SnO_x of the final product obtained from different Sn(II)/NH_3 ratios. b) Corresponding SEM micrographs showing the morphology of the different products. It is visible that crosses are formed for ratios below 0.37 Sn(II)/NH_3.

Above mentioned SnO nanosheets, fabricated on carbon cloth as template, are synthesized with similar fabrication conditions to ours, but at a higher temperature (200 °C).[8] Contrary, our approach uses a lower reaction temperature and the formation of the SnO structures occurs template-free. This reveals that the absence of a template lead to homogeneous nucleation of crosses (**Figure 4b**), which are formed by an initial core and then grow anisotropically along 110 planes according to Xu *et al.*.[28]

An alternative description for the formation of such SnO crosses was proposed by Wang *et al*.[26] by applying different cooling rates. It was assumed that shock cooling of the autoclave would yield only SnO_2 sheets, but it was not proved. However, they found that slow cooling at room temperature, instead of water cooling, lead to an increase in yield of the SnO byproduct. We hypothesized that this was probably caused by residual gaseous ammonia (NH_3) going back into dissolution at lower temperatures. Based on all these findings, the data collected in our study goes along the chemical reaction pathway of Zhang *et al.*[8] using ammonia as stabilizing agent, supported by low temperature as shown by Wang *et al*..[26] As given by equation [2] adding more ammonia results in a lower Sn(II)/NH_3 ratio, which helps to stabilize divalent Sn(II) and leads to the formation of SnO crosses in accordance with the mechanism published by Xu *et al.*.[28]

Investigation of the formation mechanism of SnO crosses was done by repeating the reaction time dependent synthesis analog to the formation of SnO_2, but with the adjusted Sn(II)/NH_3 ratio of 0.27. The PXRD patterns indicate the formation of crystalline SnO_2 after 30 minutes (**Figure 5a**). The sharp reflections fitting to the simulated pattern of SnO (ICSD 15516) observed for a reaction time of 1 h reveal the favorable formation of a crystalline SnO as dominant phase, since reflections for SnO_2 are barely visible.

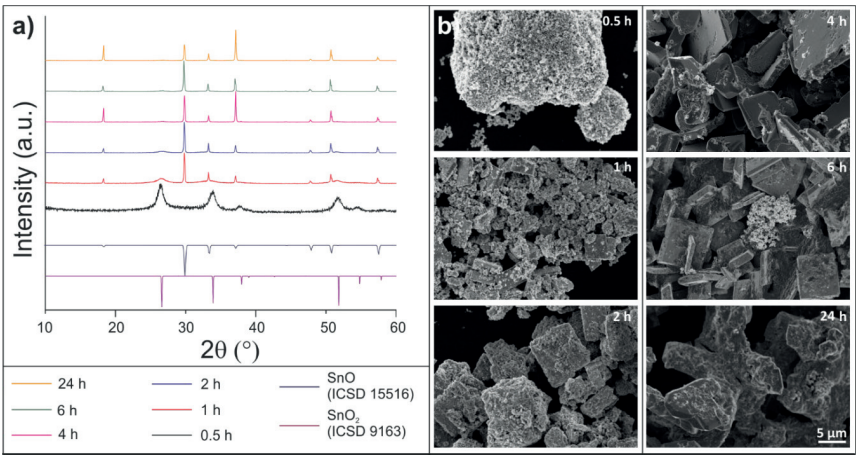

Figure 5: a) PXRD patterns during SnO cross formation as a function of time for a Sn(II)/NH_3 ratio of 0.27. b) Corresponding SEM micrographs.

The corresponding SEM investigation reveals that the SnO initially exists in a rather cubic shape, which is covered with some amorphous or nanocrystalline second phase (**Figure 5b**). After 4 h, micrometer-sized plates could be detected, from which basal planes branching occurs, upon further increasing the reaction time. After a reaction time of 6 h, the crosses were fully formed and nearly no second phase was present. For a reaction time of 24 h, strong precipitation on the surface of the crosses is visible. A Raman investigation corresponding to our time study at a ratio of 0.27 is presented in **Supplementary Figure S4**.

A different form of crosses was reported by Cui *et al*., using KOH as a mineralizer resulting in cross-shaped structures.[29] However, these structures were strongly damaged by the corrosive character of the KOH, resulting in very rough edges and partially formed crosses. Contrary, our adjusted chemically softer synthesis parameters in comparison to Cui *et al*.[29] (NH_3 instead of KOH) allowed for the formation of well-defined SnO crosses, because the corrosive decomposition is heavily suppressed and nearly perfect crosses are obtained.

2.3 Ice-templating Artificial Sponges

In a final step, the obtained SnO crosses were mixed with PVP aqueous solution at a ratio of 2:1. The dispersion was instantly frozen in the liquid nitrogen, with the aim to design an open-porous structure, which resembled that of a calcareous sponge. The formed ice was removed by freeze drying, resulting in a lamellar microstructure as shown in **Figure 6a**. Hereby, the grown ice crystals have transported the PVP/SnO material to their interface/surfaces, leaving upon sublimation voids behind, whereas the PVP/SnO forms wall-like structures.

It can be seen that microstructure of this artificial sponge is composed of regularly aligned lamellas with different orientations. The lamellas distance and orientation depends on the freezing rate and solution concentration. Upon closer inspection, the crosses are evenly distributed in the sponge and embedded into lamellas as displayed in **Figure 6b** and **c**. Therefore, they embody a similar backbone in the PVP matrix as the cross-like spicule in the calcareous sponges (**Figure 1**). Moreover, the crosses embedded into the lamella walls, might impede mechanical collapse, when immersing the sponge in a liquid medium. Such feature is therefore especially important for the sponges' mechanical integrity and accessibility.

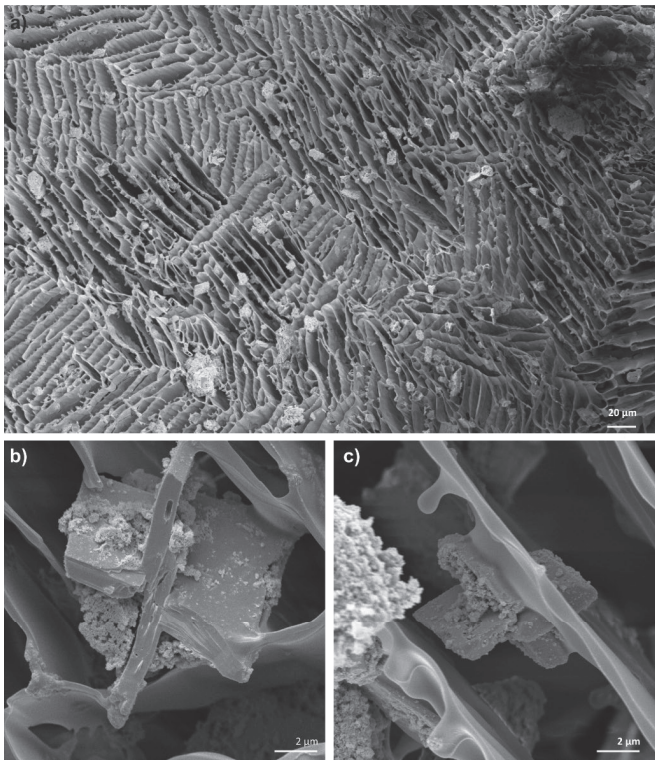

Figure 6: SEM micrographs of the artificial sponge reinforced by SnO crosses. a) microstructure composed of lamellas with different orientation and uniform distribution of the SnO crosses. b) and c) closer inspection of the microstructure reveals that crosses are embedded in the lamellas.

2.4 Conclusion

In this work we were able to replicate the structural principle of calcareous sponges in a two-step fabrication process. Analog to the sponges' ability to control the grow of cross-like spicules made of $CaCO_3$, we take advantage of ammonia as structuring agent or mineralizer to obtain SnO crosses *via* a hydrothermal process. Using an intricate control over mineralizer concentration and reaction time, we were able to fine-tune the SnO crosses. This procedure yields artificial sponges, in which the SnO crosses are evenly distributed in the walls of the highly porous PVP sponge. Thus, they embody a similar backbone structure as obtained in the natural

calcareous sponges. In particular, for applications based on liquid flow, the crosses are envisioned to defeat a collapse of the soft organic scaffold, which could happen when immersing the sponge into a liquid. Moreover, these porous structures can likewise find applications in filtering, as damping materials, as well as mechanically stable matrix for other functional materials than SnO.

2.5 Experimental Set-up

Tin oxide was synthesized by a hydrothermal method, starting with 6 mmol $SnCl_2$ (Sigma Aldrich) · 2 H_2O in an ethanol/water (1:1) mixture as initial reagent. After 10 minutes of vigorously stirring at RT to dissolve the tin(II) chloride (a clear solution is formed), ammonia was added as mineralizer (6 – 60 ml 0.45 M $NH_{3(aq)}$ (Sigma Aldrich, 32 %, p.a.)), which turned the solution opaque. The dispersion was then transferred to a Teflon-lined autoclave **(Figure S1)** (V = 25 ml) and treated at 120 °C for 0.5 to 24 h. It was washed three times with ethanol and three times with MilliQ water and centrifuged at 3000 RPM after each step, respectively. After washing, the precipitate was dried and poured into a glass beaker. For further measurements the material was prepared accordingly:

For SEM investigation the material was drop casted onto a Si wafer from an aqueous dispersion, SEM investigations were conducted on a Zeiss Ultra 55 with a FEM cathode. Raman investigations were performed after the powder was pressed with a boron silicate glass plate onto a silicon wafer. The Raman spectra were measured using an argon laser with a wave length of 488 nm under ambient conditions, with a power of 10 mW. The microscope image was taken on a high resolution light microscope, whereas the calcareous sponge *Cl. Clathrus* was stored in ethanol and prepared between to glass plates (Carl Roth GmbH).

For PXRD investigations the sample was placed in the aluminum sample holder and the surface flattened with a boron silicate glass plate and the measurements were carried out in $\vartheta/2\vartheta$ Bragg-Brentano geometry on a Smart-Lab X-Ray Diffractometer from Rigaku Corporation with Cu-K_α radiation. Cu-K_β radiation was filtered by a thin Ni foil (~90 % efficiency).

The chemical analysis was performed using ICP-OES in order to investigate the tin content while combustion analysis was performed to determine the oxygen and hydrogen amount, (with nitrogen and helium as carrier gas, respectively).

In order to fabricate the artificial sponge, ice templating approach was used. The aqueous SnO crosses solution was made of 0.54 g SnO powder (0.27 ratio, 6h) mixed with 0.254 g Polyvinylpyrrolidone (Sigma Aldrich, m_w = 55000 g mol^{-1}) and then dispersed in 0.5 ml deionized H_2O. Such obtained solution then was poured into a precooled (77 K) cylindrical elastomer moulds, with a diameter of 8 mm and a height of 10 mm and immersed for 5 minutes in liquid nitrogen. Subsequently, the mould was transferred to a climate chamber at 248 K (Vötsch VC 7018) and stored for 7 minutes, in order to remove the sample from the mould. Such obtained freestanding frozen sample was transferred to a freeze drier (P4K Peter Piatkowski) and freeze-dried over 22 hours. The foam was removed after drying and sputtered (SCD 40) with gold to ensure sufficient conductivity to perform SEM investigations.

2.6 Acknowledgements

The authors thank Achim Diem for proofreading and microscopy assistance as well as Kevin Hildebrand and Jonathan Link for experimental assistance, and Prof. Jürgen Weis, MPI-FKF Stuttgart Nanostructuring Lab, for providing access to the Light Microscope. We further would like to thank Dr. Efi Hadjixenophontos, Institute for Material Science, University of Stuttgart, for providing access to the TEM and Prof. Joachim Spatz, MPI for Medical Research, University of Heidelberg, for providing access to the SEM.

2.7 References

1. Ogo Y, Hiramatsu H, Nomura K, Yanagi H, Kamiya T, Hirano M, Hosono H. 2008 p-channel thin-film transistor using p-type oxide semiconductor, SnO. *Appl. Phys. Lett.* 93, 032113. (doi:10.1063/1.2964197)

2. Gaggiotti G, Galdikas A, Kačiulis S, Mattogno G, Šetkus A. 1994 Surface chemistry of tin oxide based gas sensors. *Journal of Applied Physics* 76, 4467–4471. (doi:10.1063/1.357277)

3. Chiu I, Li Y, Tu M, Cheng I. 2014 Complementary Oxide–Semiconductor-Based Circuits With n-Channel ZnO and p-Channel SnO Thin-Film Transistors. *IEEE Electron Device Letters* 35, 1263–1265. (doi:10.1109/LED.2014.2364578)

4. Li Y, Xin Q, Du L, Qu Y, Li H, Kong X, Wang Q, Song A. 2016 Extremely Sensitive Dependence of SnO_x Film Properties on Sputtering Power. *Scientific Reports* 6, 36183.

(doi:10.1038/srep36183)

5. Seal S, Shukla S. 2002 Nanocrystalline SnO gas sensors in view of surface reactions and modifications. *JOM* 54, 35–38. (doi:10.1007/BF02709091)

6. Moseley PT. 1992 Materials selection for semiconductor gas sensors. *Sensors and Actuators B: Chemical* 6, 149–156. (doi:10.1016/0925-4005(92)80047-2)

7. In press. Microstructure, optical, and electrical properties of p-type SnO thin films: Applied Physics Letters: Vol 96, No 4. See https://aip.scitation.org/doi/abs/10.1063/1.3277153 (accessed on 8 March 2019).

8. Zhang F, Zhu J, Zhang D, Schwingenschlögl U, Alshareef HN. 2017 Two-Dimensional SnO Anodes with a Tunable Number of Atomic Layers for Sodium Ion Batteries. (doi:10.1021/acs.nanolett.6b05280)

9. Su D, Xie X, Wang G. 2014 Hierarchical Mesoporous SnO Microspheres as High Capacity Anode Materials for Sodium-Ion Batteries. *Chemistry – A European Journal* 20, 3192–3197. (doi:10.1002/chem.201303702)

10. Li H, Huang X, Chen L. 1999 Structure and electrochemical properties of anodes consisting of modified SnO. *Journal of Power Sources* 81–82, 335–339. (doi:10.1016/S0378-7753(99)00212-8)

11. Yu DYW, Prikhodchenko PV, Mason CW, Batabyal SK, Gun J, Sladkevich S, Medvedev AG, Lev O. 2013 High-capacity antimony sulphide nanoparticle-decorated graphene composite as anode for sodium-ion batteries. *Nature Communications* 4, 2922. (doi:10.1038/ncomms3922)

12. van der Vliet DF, Wang C, Tripkovic D, Strmcnik D, Zhang XF, Debe MK, Atanasoski RT, Markovic NM, Stamenkovic VR. 2012 Mesostructured thin films as electrocatalysts with tunable composition and surface morphology. *Nature Materials* 11, 1051–1058. (doi:10.1038/nmat3457)

13. Chirilă A *et al.* 2013 Potassium-induced surface modification of $Cu(In,Ga)Se_2$ thin films for high-efficiency solar cells. *Nature Materials* 12, 1107–1111. (doi:10.1038/nmat3789)

14. Iqbal MZ, Wang F, Zhao H, Rafique MY, Wang J, Li Q. 2012 Structural and electrochemical properties of SnO nanoflowers as an anode material for lithium ion batteries. *Scripta*

Materialia 67, 665–668. (doi:10.1016/j.scriptamat.2012.07.010)

15. Iqbal MZ, Wang F, Feng T, Zhao H, Rafique MY, Din R ud, Farooq MH, Javed Q ul ain, Khan DF. 2012 Facile synthesis of self-assembled SnO nano-square sheets and hydrogen absorption characteristics. *Materials Research Bulletin* 47, 3902–3907. (doi:10.1016/j.materresbull.2012.07.002)

16. Hewitt RA. 1975 Analysis of aragonite from the cuttlebone of Sepia officinalis L. *Marine Geology* 18, M1–M5. (doi:10.1016/0025-3227(75)90033-X)

17. Jackson A. P., Vincent Julian F. V., Turner R. M., Alexander Robert Mcneill. 1988 The mechanical design of nacre. *Proceedings of the Royal Society of London. Series B. Biological Sciences* 234, 415–440. (doi:10.1098/rspb.1988.0056)

18. Uriz M-J. 2006 Mineral skeletogenesis in sponges. *Can. J. Zool.* 84, 322–356. (doi:10.1139/z06-032)

19. In press. An Acidic Matrix Protein, Pif, Is a Key Macromolecule for Nacre Formation | Science. See http://science.sciencemag.org/content/325/5946/1388 (accessed on 8 March 2019).

20. Klautau M, Valentine C. 2003 Revision of the genus *Clathrina* (*Porifera, Calcarea*). *Zoological Journal of the Linnean Society* 139, 1–62. (doi:10.1046/j.0024-4082.2003.00063.x)

21. Hooper J, Soest RWM van, editors. 2002 *Systema Porifera: A Guide to the Classification of Sponges*. Springer US. See https://www.springer.com/de/book/9780306472602.

22. Sethmann I, Wörheide G. 2008 Structure and composition of calcareous sponge spicules: A review and comparison to structurally related biominerals. *Micron* 39, 209–228. (doi:10.1016/j.micron.2007.01.006)

23. Li G, Ciston S, Saponjic ZV, Chen L, Dimitrijevic NM, Rajh T, Gray KA. 2008 Synthesizing mixed-phase TiO_2 nanocomposites using a hydrothermal method for photo-oxidation and photoreduction applications. *Journal of Catalysis* 253, 105–110. (doi:10.1016/j.jcat.2007.10.014)

24. Ni Y, Wei X, Hong J, Ye Y. 2005 Hydrothermal preparation and optical properties of ZnO nanorods. *Materials Science and Engineering: B* 121, 42–47. (doi:10.1016/j.mseb.2005.02.065)

25. Meskin PE, Ivanov VK, Barantchikov AE, Churagulov BR, Tretyakov YD. 2006 Ultrasonically

assisted hydrothermal synthesis of nanocrystalline ZrO_2, TiO_2, $NiFe_2O_4$ and $Ni_{0.5}Zn_{0.5}Fe_2O_4$ powders. *Ultrasonics Sonochemistry* 13, 47–53. (doi:10.1016/ j.ultsonch.2004.12.002)

26. Wang C, Du G, Ståhl K, Huang H, Zhong Y, Jiang JZ. 2012 Ultrathin SnO_2 Nanosheets: Oriented Attachment Mechanism, Nonstoichiometric Defects, and Enhanced Lithium-Ion Battery Performances. *J. Phys. Chem. C* 116, 4000–4011. (doi:10.1021/jp300136p)

27. Papargyri S, Tsipas DN, Papargyris DA, Botis AI, Papargyris AD. 2005 Review on the Production and Synthesis of Nanosized SnO_2. *Solid State Phenomena* 106, 57–62. (doi:10.4028/www.scientific.net/SSP.106.57)

28. Xu X, Ge M, Ståhl K, Jiang JZ. 2009 Growth mechanism of cross-like SnO structure synthesized by thermal decomposition. *Chemical Physics Letters* 482, 287–290. (doi:10.1016/ j.cplett.2009.10.012)

29. Cui Y, Wang F, Iqbal MZ, Li Y, Toufiq AM, Wang Z, Wang Z, Ali S. 2015 Synthesis of nanoflakes-based self-assembling crossed structure of stannous oxide and photocatalysis property. *Crystal Research and Technology* 50, 210–214. (doi:10.1002/crat.201400202)

30. Deuerling S, Kugler S, Klotz M, Zollfrank C, Van Opdenbosch D.2018 A Perspective on Bio-Mediated Material Structuring, *Advanced Materials*, 30, 19, Page 1703656. (DOI: 10.1002/adma.201703656)

2.8 Supporting Information

Table S1. Concentration of reagent ions in solution.

Concentration of tin ions [mol·l^{-1}]	**Concentration of ammonia [mol·l^{-1}]**	**Sn(II)/NH_3 ion ratio**
0.23	0.10	2.22
0.18	0.16	1.11
0.13	0.24	0.55
0.10	0.28	0.37
0.08	0.31	0.27
0.075	0.35	0.21

Figure S1: Experimental setup for the hydrothermal synthesis. A chemical autoclave with a Teflon lining was used and placed in the furnace at 120 °C.

Raman measurement were conducted in order to obtain information about the oxidation state of the product at each reaction time. The displayed Raman shifts are correlated to the PXRD data shown in **Figure 3**. In general, a Raman shift is occurring, when a vibration mode in the crystal lattice is activated. This means, that the number of shifts depends on the number of possible Raman active vibration modes, the crystallinity of the material and the size of the unit cell. In detail, SnO_2 is crystallizing in the rutile type and has 18 vibration modes in the unit cell.[1] According to Diéguez *et al.*[1] four modes are RAMAN active, of which 3 can be recognized in the spectrum, namely at 638 cm^{-1} (A_{1g}), at 782 cm^{-1} (B_{2g}) and 476 cm^{-1} (E_g).

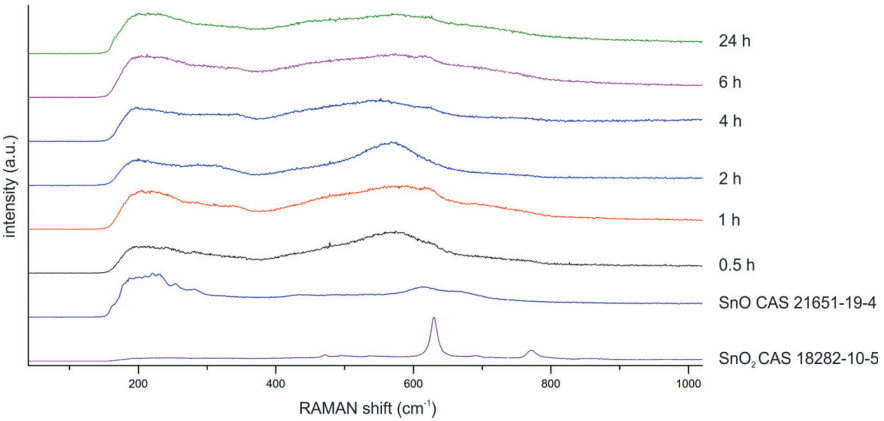

Figure S2: Raman spectra for products obtained after different reactions times for a 0.55 Sn(II)/NH_3ratio. As reference, commercially available SnO (Sigma Aldrich, CAS 21651-19-4) and SnO_2 (Sigma Aldrich, CAS 18282-10-5) was measured.

In the spectrum (**Figure S2**), only very broad peaks can be recognized, namely a peak in the region 580 and a small shoulder around 620. They belong mainly to SnO_2, resulting from disorder activation of additional bands, as reported by Diéguez *et al.*[1] for the study of not calcined SnO_2 nanoparticle powders. This goes in accordance with the data obtained by TEM and PXRD, indicating a high degree of crystalline disorder, i.e. an amorphous phase. However, the shoulder observed at 620 cm^{-1} can be related to the formation of a crystalline SnO_2 phase, which is in agreement with the data obtained by PXRD (**Figure 3a**). The peaks observed at 180 – 270 cm^{-1} can be related to the formation of SnO and their partial oxidation to SnO_2, as reported by Eifert *et al.*[2] for tin oxide intermediate structures.

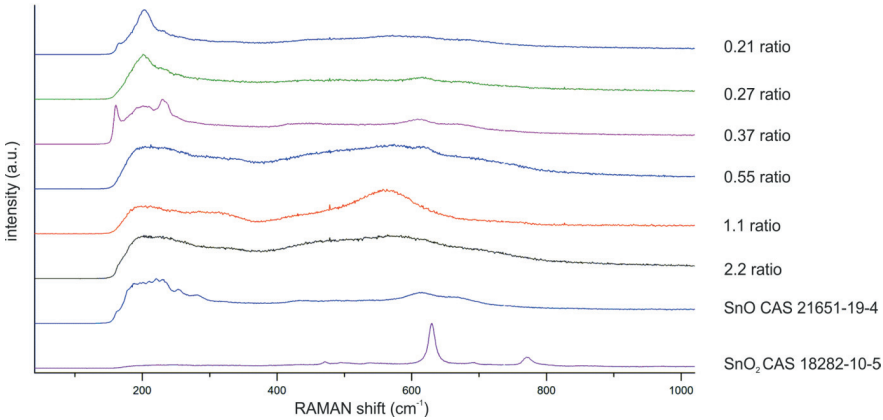

Figure S3: Raman spectra of the products with different Sn(II)/NH_3 ratios. As reference, commercially available SnO (Sigma Aldrich, CAS 21651-19-4) and SnO_2 (Sigma Aldrich, CAS 18282-10-5) was measured.

In order to determine the oxidation state of the obtained product, Raman measurements were conducted. In **Figure S3** the measurements supporting the data shown in **Figure 4a** are displayed. The transition from the precursor phase to the crystalline SnO phase is observed for Sn(II)/NH_3 ratio below 0.37 as the peak in the region around 580 – 620 cm^{-1} is disappearing and a strong peak around 210 cm^{-1} is present. The 3 peaks at 185 cm^{-1}, 210 cm^{-1} and 240 cm^{-1}, we observe for the ratio 0.37 belong to SnO (210 cm^{-1}) and an intermediate tin oxide (Sn_2O_3 and Sn_3O_4) phase,[2] which might be formed due to lack of oxygen in the autoclave. However, in the

respective PXRD diffraction pattern (0.37 Sn(II)/NH_3 ratio) there are no corresponding reflections present, most probable because their reflections are covered by the highly crystalline SnO.

For the Sn(II)/NH_3 ratio 0.27 and lower ratios only the peak belonging to SnO is present (210 cm^1). The difference to the obtained reference pattern of SnO (SnO CAS 21651-19-4) is most likely due to the morphology of the SnO crosses, leading to {001} and {110} top facets, resulting in very distinct raman modes and as such very distinct peaks.[3]

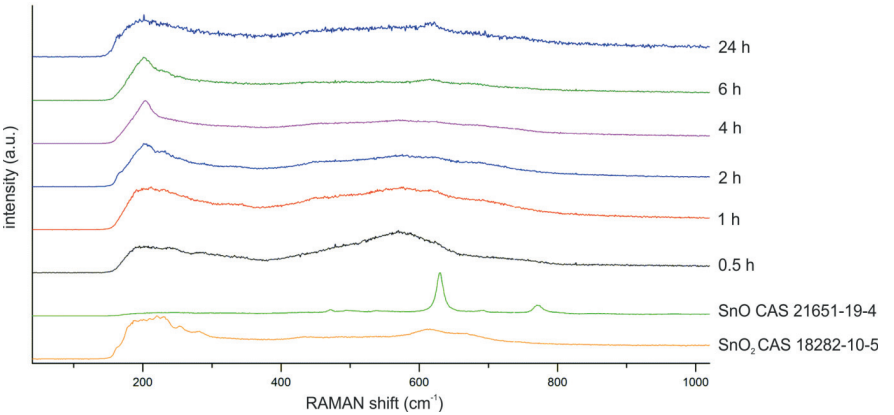

Figure S4: Raman spectra of the products obtained by a time resolved study of a 0.27 Sn(II)/NH_3 ratio is presented (in correlation to **Figure 5a**). As reference, commercially available SnO (Sigma Aldrich, CAS 21651-19-4) and SnO_2 (Sigma Aldrich, CAS 18282-10-5) was measured. The spectrum for 24 h was taken at a lower resolution, resulting in a larger background and lower peaks.

Using Raman, we have been able to show a clear formation of first SnO_2 structures according to ref.[1] and over time different SnO morphologies. Hereby, the peak which is clearly visible at 0.5 h around 580 cm^{-1} is disappearing with prolonged reaction times, whereas a peak appears and constantly increasing at 210 cm^{-1}, proving the formation of a crystalline SnO phase.[3] However, upon a reaction time of 24 hours, when the cross structures are not clearly visible anymore (**Figure 5b** at 24 h)**,** the peak at 210 cm^{-1} is becoming, in accordance with the morphology changes observed by SEM, diffuse.

References

1. Diéguez A, Romano-Rodríguez A, Vilà A, Morante JR. 2001 The complete Raman spectrum of nanometric SnO_2 particles. *Journal of Applied Physics* 90, 1550–1557. (doi:10.1063/1.1385573)

2. Eifert B, Becker M, Reindl CT, Giar M, Zheng L, Polity A, He Y, Heiliger C, Klar PJ. 2017 Raman studies of the intermediate tin-oxide phase. *Physical Review Materials* 1. (doi:10.1103/PhysRevMaterials.1.014602)

3. Geurts J, Rau S, Richter W, Schmitte FJ. 1984 SnO films and their oxidation to SnO_2: Raman scattering, IR reflectivity and X-ray diffraction studies. *Thin Solid Films* 121, 217–225. (doi:10.1016/0040-6090(84)90303-1)

3. Coalescence in Hybrid Materials – The Key to High Capacity Electrodes

(Reprinted with permission of the American Chemical Society.)

Timotheus Jahnke, Andrea Knöller, Stefan Kilper, Dirk Rothenstein, Marc Widenmeyer, Zaklina Burghard, Joachim Bill*

Abstract

The rising demand for flexible electronic devices requires the development of bendable lithium-ion batteries (LIBs), in which paper-like electrodes exhibit a high electrochemical storage capacity coupled with excellent mechanical flexibility. Along this line, this work proposes a novel fabrication method for self-supporting paper-like anodes, which are exclusively made from active materials. Metastable $SnCl_x(OH)_yO_z$ precursor particles and graphene oxide (GO) sheets are assembled in a facile and low-cost way, leading to paper-like hybrid materials. Subsequent annealing at 500 °C under argon atmosphere reduces the GO simultaneously with the transformation of the metastable precursor to tin dioxide (SnO_2) *via* a direct oxygen transfer mechanism between the two components. This oxygen transfer is accompanied by the anchoring of the SnO_2 particles onto the reduced GO (rGO) sheets, yielding in an excellent synergy between mechanical stability, electrical conductivity and electrochemical capacity of the hybrid material. The latter reaches values of up to 700 mAh g^{-1} due to the coalescence of two components during the fabrication process. These findings qualify this novel fabrication strategy to be also transferred to other electrochemically active systems, which simultaneously require mechanical stability and high storage capacity.

3.1 Introduction

One of the main tasks in the research field of energy storage media, such as batteries, is the development of durable, high capacity electrodes, which meet current demands for electronic devices.[1–5] Commercial electrodes consist of three main components, namely an electrochemically active material, a binder, and conductive carbon black. Processed to slurry, the components are coated onto a current collector, which also serves as mechanical support. Upon charging and discharging, the active material expands and contracts due to the intercalation and deintercalation of ions, respectively. The charge-discharge cycles therefore induce mechanical stresses in the matrix made of binder and carbon black. Initially, these stresses are partially compensated by the used binder.[4] However, upon repeated charging and discharging, such electrodes gradually lose their structural integrity. Consequently, delamination of the active material from the conductive matrix occurs, which results in a continuous fading of the electrochemical performance.[6–8]

In recent years, advances in the field of electrode design have been made using different strategies, which specifically address the problem of electrode material disintegration. Choi *et al.*[9] customized conventional binders by adding polyrotaxanes. These polyrotaxanes act as flexible pulleys, which strongly bind with one side to the active material and with the other side to the binder matrix, establishing a strong, but flexible bond between them. The flexible pulleys, working similar to a rubber band, fully compensate the stress during the charge-discharge cycles. Although this strategy provides promising results concerning conventional electrodes, a large amount of electrochemically inactive additives (20 wt.%[10]) reduces the capacity per weight fraction (gravimetric capacity) of the electrodes. Binder-free alternatives are based on embedding the active material in different carbon (nano)structures, such as carbon nanotubes or graphene.[10–12] Especially graphene sheets have been in the research focus due to their good mechanical stability and high electrical conductivity.[13–15] In addition, when the single graphene sheets are being stacked, ions can intercalate between the sheets similarly as in graphite, which is a typical anode material with a theoretical capacity of 372 mAh g^{-1}.[16] Even though graphene sheets appear to be promising candidates to fabricate binder-free electrodes, the strong tendency of the sheets to form agglomerates hinders their processability. Alternatively, processing graphene oxide (GO) sheets instead of graphene sheets suppresses the agglomeration of them.[17,18] Specifically, GO is usually fabricated as a stable aqueous suspension stabilized by the oxygen-containing functional groups located at the surface and

edges of the sheets.[19] These functional groups also promote the assembling of the GO sheets during water removal, which leads to a flexible, paper-like material.[20] The controlled assembled GO sheets can then be subsequently annealed, yielding reduced GO (rGO) sheets with good electrical conductivity.[18] For example, Wang *et al.*[21] by reduction of GO paper at 500 °C achieved a conductivity of ~ 50 S cm^{-1}.

While being electrically conducting and mechanically stable, such graphene-based electrodes exhibit inferior theoretical capacities in comparison to other active materials, including silicon (4200 mAh g^{-1})[22] or tin dioxide (782 mAh g^{-1})[23]. However, the latter two are typically only available in the form of loose powder with poor electrical conductivity. Combining silicon or SnO_2 nanoparticles with GO is a promising approach to increase the theoretical capacity along with preserving the mechanical stability and electrical conductivity of the graphene-based electrodes.[24,25] Gao *et al.*[14] embedded commercially available SnO_2 particles into a GO matrix by simple vacuum filtration of the mixed suspension. Subsequent chemical reduction of the GO using hydrobromic acid ($HBr_{(aq)}$) yielded free-standing paper-like electrodes (capacity ~ 600 mAh g^{-1} after 100 cycles). Although the graphene sheets tightly wrapped the SnO_2 particles, there was no chemical interconnection between both components leading to capacity losses due to delamination of the active material, analog to the conventional slurry-based electrodes. Alternatively, Zhu *et al.*[26] electro-spun a phase mixture of SnO_2, SnO, and Sn_3O_4 (SnO_x) with polyvinyl pyrrolidone into fibers. Subsequent annealing at 500 °C, led to the formation of ultrafine SnO_x nanocrystals on amorphous carbon fibers. While the interconnection between the SnO_x nanocrystals and the carbon matrix was improved, the accessibility of the active material was hindered by the compact structure of the carbon matrix, leading to a capacity of about 600 mAh g^{-1}. Therefore, the challenge is to fabricate a hybrid electrode, which features both, a good interconnection between the constituents and sufficient accessibility for lithium ions. Along this line, Ye *et al.*[27] proposed an approach, which involved a laser ablation in liquid technique and subsequent oxidation/reduction of the SnO_x particles on GO sheets for 7 days. During this oxidation/reduction process, nanosized SnO_2 particles grow on GO sheets, while the GO is simultaneously reduced, yielding a powder-like product. In contrast, Wang *et. al.*[28] synthesized SnO_2-decorated GO sheets, using an *in situ* hydrolysis approach. Stirring of the decorated GO sheets at 120 °C and subsequent vacuum filtration yielded a GO/SnO_2 composite paper. Analog to the finding of Zhu *et al.*[26], the resulting electrode material appeared to be too compact to allow sufficient lithium diffusion. Only by subsequent multiple folding of the papers, they were able to highly enhance the LIB

performance of this composite electrode material. However, this method is very time consuming, as it requires multiple folding steps.

Here we propose a novel strategy to fabricate a paper-like hybrid material made of reduced GO sheets and SnO_2 nanocrystals. We used metastable $SnCl_x(OH)_yO_z$ precursor particles and GO sheets and combine them in a facile and low-cost co-assembly process, followed by a thermal treatment step. The obtained sophisticated paper-like SnO_2/rGO electrodes exhibit an ideal balance between interconnection of both components and good accessibility for lithium ions, enabling high electrochemical capacity and good durability.

3.2 Results & Discussion

The metastable $SnCl_x(OH)_yO_z$ precursor particles, were fabricated by using a modified hydrothermal method with tin(II) chloride dihydrate and aqueous ammonia solution as initial reagents.[23] This synthesis route led to platelet-shaped alkaline tin oxychloride ($SnCl_x(OH)_yO_z$) particles (**Supplementary Figure S1**). GO sheets, were fabricated by a modified Hummers method,[19] which resulted in an aqueous suspension containing single-layered sheets with a height of about 1.5 to 2 nm and several micrometers in lateral dimension (**Supplementary Figure S2**). Owing to the high sheet concentration, alongside with the presence of oxygen-containing functional groups at the sheets' basal planes and edges, a stabilizing hydrogen bond (H-bond) network is formed in the suspension.[29] After adding the $SnCl_x(OH)_yO_z$ particles to the suspension and thoroughly mixing both components, the H-bond network likewise stabilizes the $SnCl_x(OH)_yO_z$ particles within the suspension, thus guaranteeing a homogenous distribution (**Figure 1a**).[29,30] Upon slow water evaporation, the suspension turns into a gel, in which the GO sheets align predominantly parallel to the substrate surface, and the precursor particles are located between these GO layers. Further water removal compresses this layered arrangement, resulting in dried hybrid papers with thicknesses of about 4 µm and excellent mechanical flexibility (**Figure 1b**), which is even preserved after the final thermal treatment (**Figure 1c**).

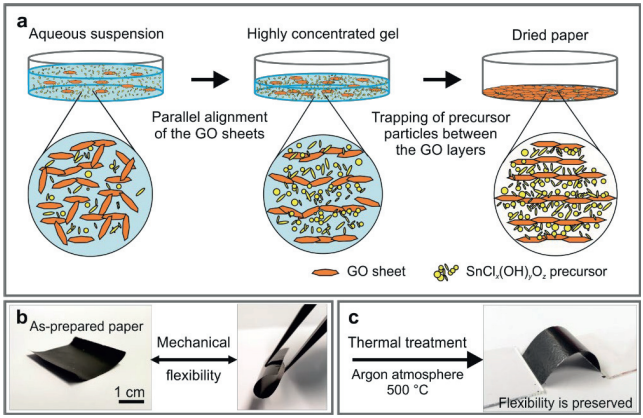

Figure 1. (a) Schematic of the co-assembly process, involving GO sheets and $SnCl_x(OH)_yO_z$ precursor particles from an aqueous suspension. Slow water evaporation leads to gelation, whereat the GO sheets begin to align horizontally. The complete removal of water yields a hybrid thin-film, in which the $SnCl_x(OH)_yO_z$ precursor particles are trapped between layers of GO sheets. (b) Photograph of the formed paper-like hybrid material, displaying excellent mechanical flexibility, which (c) is preserved upon annealing.

Scanning electron microscopy (SEM) investigations of the films' surface and cross section confirmed the layered arrangement of the GO sheets, in which the $SnCl_x(OH)_yO_z$ particles were embedded (**Figure 2a and b**). The microstructure of the hybrid materials was investigated as a function of the composition ($SnCl_x(OH)_yO_z$ to GO weight ratio) to determine the maximum $SnCl_x(OH)_yO_z$ content at which the respective particles were still homogenously distributed in the GO matrix (**Supplementary Figure S3**), without applying any surfactants or binder during the assembly process. Such additives are typically used to improve the material's homogeneity and mechanical integrity but could impair the LIB performance. The microstructure appeared to be predominantly homogeneous, i.e. well distributed particles between and on top of single GO sheets, in the case of a 1:2 ratio of $SnCl_x(OH)_yO_z$ to GO (**Supplementary Figure S3a**). In contrast, increased ratios to 1:1 and 2:1, respectively, led to agglomeration of the $SnCl_x(OH)_yO_z$ particles and an increasing tendency towards phase separation (**Supplementary Figure S3b and c**). Consequently, it can be assumed that for lower precursor to GO ratios, single $SnCl_x(OH)_yO_z$ particles were surrounded predominantly by GO sheets, between which they can be confined and finally trapped. However, increasing the precursor concentration increased the probability to have neighboring precursor particles, promoting agglomeration. In order to

impede the formation of these agglomerates and to ensure evenly distributed particles in the microstructure, only the 1:2 ratio was further considered.

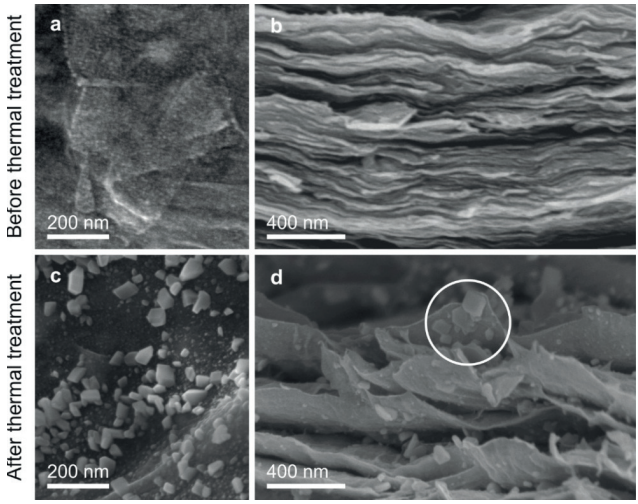

Figure 2. SEM images of (a) the surface and (b) the cross section of a hybrid paper before the thermal treatment. The GO sheets are stacked and tightly trap the $SnCl_x(OH)_yO_z$ nanoparticles. Subsequent thermal treatment at 500 °C induces pronounced structural changes, as depicted in the SEM images of (c) the surface and (d) the cross section, which shows the presence of nanosized crystals on top of the hybrid paper as well as within the between the sheets (white circle).

Thermally post-treating the initial $SnCl_x(OH)_yO_z$/GO hybrid papers at 500 °C in argon atmosphere finally yielded the desired SnO_2/rGO hybrid papers. During this process, a noticeable structural change occurred (**Figure 2c and d**). Although structural changes were observed on a micro scale, the composite paper still retained its flexible nature, as displayed in Figure 1 The slow heating (4 $Kmin^{-1}$) to 500 °C enables a successive release of the evolving gases (see also **Figure 4**), minimizing the risk of microcracks, thus preserves the structural integrity. Moreover, the originally platelet-shaped precursor particles (**Supplementary Figure S1**) turned into nanocrystals, which have a size distribution in the range of a few to several hundred nanometers. These nanocrystals are anchored to the adjacent rGO sheets (**Figure 2d**, white circle) and will function as electrochemical intercalation sites as well as space holders between

the rGO sheets. The latter function not only opens diffusion paths, but also provides the rGO sheets with additional freedom to move upon external stress, enabling macroscopic flexibility of the hybrid paper. This flexibility was not observed in case of the pure rGO, which exhibited a pronounced brittleness, making such papers hard to process into disk-shaped electrodes. In contrast, the hybrid papers could be easily punched out, yielding suitable electrode disks (**Supplementary Figure S4**).

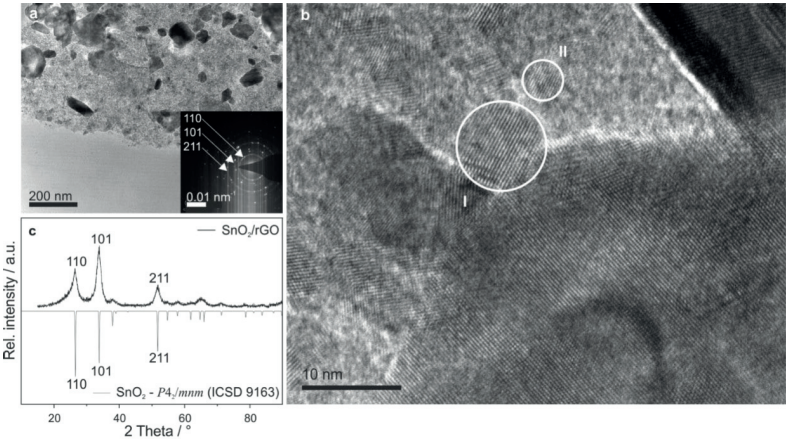

Figure 3. (a) TEM micrograph of SnO_2 crystals covering a single rGO sheet. The inset in (a) displays the electron diffraction pattern of specific crystals grown on the rGO sheet. (b) A higher magnification image displays the crystalline structure, including the lattice plane distance of two nanosized crystals (white circles). The crystal marked by circle I appears to have a larger lattice plane distance than the one labelled by circle II, implying different crystal orientations, (c) Complementary, the PXRD pattern of the hybrid film displays an increase in intensity of the (101) peak, which corresponds to the lattice plane distance of the particle highlighted by circle I in (b).

The defined morphology of the arising nanocrystals with their sharp edges indicated a high degree of crystallinity. The latter was verified using transmission electron microscopy (TEM), complemented by diffraction measurements (**Figure 3**). The selected area electron diffraction pattern (**Figure 3a**, inset) is in accordance with the diffraction pattern of a general rutile type structure, in which the observed diffraction rings belong to the (110), (101), and (211) lattice planes of SnO_2 in the out-of-plane direction.[31] Complementary, different lattice plane distances

were observed on different nanocrystals, *e.g.* the lattice plane distances of the nanocrystal labelled by circle I, was determined to be 3.40 ± 0.08 Å, while the nanocrystal marked by circle II has smaller lattice plane distances of 2.54 ± 0.09 Å (**Figure 3b**). The identified lattice plane distances of 3.4 Å and 2.5 Å correlate well with the distances of the (110) and (101) lattice planes, respectively, of rutile-type SnO_2 (ICSD Card Nr. 9163).[30] The complementary powder X-ray diffraction (PXRD) pattern of the annealed hybrid papers displayed in **Figure 3c** verifies the presence of these reflections. However, compared to the reference pattern (ICSD Card Nr. 9163), a broadening is observed for all reflections, which is a direct result of the small crystallite size calculated by the Scherrer equation (~ 4 – 10 nm), which is in good agreement with the crystallize sizes obtained by HRTEM images (**Figure 3c**). Additionally, an alteration in the intensity of the most pronounced reflections 110 at 2ϑ = 26.5° and 101 at 2ϑ = 33.8° is visible, implying a preferred orientation of the anchored nanocrystals. Furthermore, TEM investigation confirms the same texturing (**Supplementary Figure S5**). More nanocrystals with an out-of-plane lattice plane distance of 3.40 ± 0.08 Å (analog to circle I) are identified, which correlates to the in-plane texturing of the 2.54 ± 0.09 Å lattice plane distance in the tetragonal crystal structure.

Alongside the transition of the $SnCl_x(OH)_yO_z$ precursor to phase pure SnO_2, the applied thermal post-treatment at 500 °C in argon is also known to reduce GO.[18] The conductivity of the reduced paper-like film is ~ 40 Scm^{-1}, which is similar to values obtained by Wang *et al.* for the reduction of GO bucky papers at 500 °C.[21] This finding indicates that the reduction of the GO paper has occurred, including the removal of hydroxyl- and epoxy groups. To investigate the reduction of GO in detail, thermogravimetric analysis (TGA) of the hybrid papers was performed under argon. The thermal treatment led to an initial mass loss of about 15.3 wt.% between 110 °C and 260 °C (**Supplementary Figure S6**). This mass loss was related to the removal of gaseous HCl (originating from the $SnCl_x(OH)_yO_z$ precursor), physisorbed humidity and partially to the removal of the epoxy- and hydroxyl groups from the GO sheets, following the results published by Acik *et al.*.[33] A further increase of the temperature accelerated the reduction of GO,[18,33] which resulted in a mass loss to 27.4 wt.%. This total mass loss is noticeably lower than the one of similar materials, which is typically in the range of 40 to 50 wt.%.[14] Such discrepancy can be explained by the direct oxygen transfer between the GO sheets and the $SnCl_x(OH)_yO_z$ precursor. The immediate uptake of the released oxygen by the precursor, thus its oxidation, counteracts the mass loss.

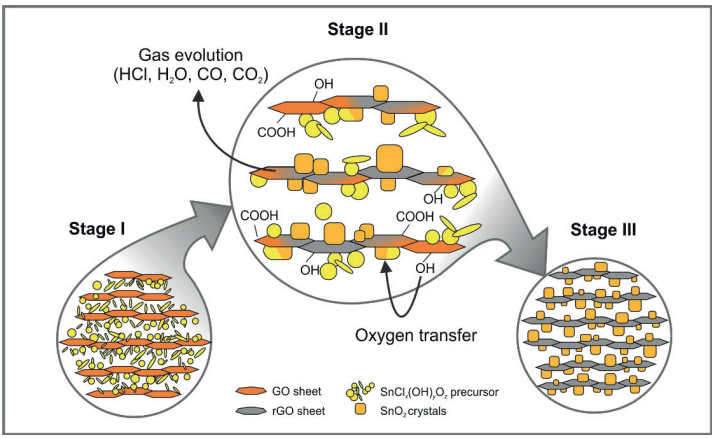

Figure 4. Schematic of the redox reaction during the thermal treatment. Stage I displays the structure of the hybrid papers in the initial state, with the metastable precursor embedded between single GO sheets. During heating (Stage II), the GO sheets are reduced, and the metastable precursor is partially oxidized to SnO_2. Hereby, a direct oxygen transfer from the GO sheets to the metastable precursor takes place. During the reduction of GO the gas evolution takes place preferably at the edges of the GO sheets.[33] Stage III displays the final product, in which a complete conversion of the precursor to SnO_2 is accomplished, and the nanosized crystals are anchored onto the basal planes of the rGO sheets.

The direct oxygen transfer mechanism from GO sheets to the precursor particles is schematically depicted in **Figure 4**. As shown in Stage II, the removal of epoxy- and hydroxyl groups from the GO led to the formation of hydroxyl radicals,[33] which can react with the $SnCl_x(OH)_yO_z$ precursor particles to form SnO_2 *via* initial release of gaseous HCl, followed by gaseous H_2O. The formation of HCl is assumed to be promoted, as the Sn-Cl (D_0 = 406 kJ mol^{-1} [37]) bonds break prior to Sn-O (D_0 = 548 kJ mol^{-1} [37]) bonds, when being thermally treated. In addition, at 500 °C a partial decomposition of GO led to an additional gas evolution, namely of CO and CO_2, which was assumed to be the main origin for the observed mass loss at higher temperatures (T > 260 °C).[33] The direct oxygen transfer was confirmed by comparing the conversion of the metastable $SnCl_x(OH)_yO_z$ precursor in the absence and the presence of GO upon thermal treatment in argon. In the absence of GO a disproportionation of the $SnCl_x(OH)_yO_z$ precursor into spherical Sn particles and SnO_2 agglomerates (**Supplementary Figure S7**) was observed and confirmed by SEM/energy dispersive X-ray spectroscopy (EDX) and PXRD. A similar effect was previously observed by Moreno *et al.* for SnO.[34] While the absence of oxygen

led to the disproportionation of SnO into metallic Sn and SnO_2, the thermal treatment in air led to complete conversion of SnO to SnO_2. Concerning our hybrid material, the GO sheets served as oxygen source for the conversion of the metastable $SnCl_x(OH)_yO_z$ precursor to phase pure SnO_2. The presence of a direct oxygen transfer was seemed to promote the textured growth of the SnO_2 nanocrystals and was likewise responsible for their anchoring onto the rGO sheets, yielding a strong coalescence in this type of hybrid material. This coalescence, which is visualized in **Figure 2c** and **d**, was also verified by Fourier-transform infrared spectroscopy (FTIR) measurements (**Supplementary Figure S8**). The bands typical for rGO have also appeared in the SnO_2/rGO hybrid material. In particular, the increased intensity of the band at 1594 cm^{-1}, which refers to the C=C stretching, is characteristic for the reduction of GO to rGO.[34] The bands at 1022 cm^{-1} and 1120 cm^{-1} belong to SnO_2, thus indicate Sn-O vibrations and Sn-O lattice stretching, respectively.[36] Complementary, a sharp band at 668 cm^{-1} arose after thermal treatment, which is not characteristic for rGO or pristine SnO_2. The latter exhibits a band between 605 and 630 cm^{-1} attributed to the asymmetric O-Sn-O stretching.[37] This SnO_2 band appears to be shifted to even higher wavenumbers (668 cm^{-1}) in the presence of rGO, confirming the coalescent growth process of crystalline SnO_2 particles on rGO.

Owing to the gas evolution and oxygen transfer upon thermal treatment, the initial weight ratio of the two components shifted from 1:2 ($SnCl_x(OH)_yO_z$ to GO) towards about 2:1 (SnO_2 to rGO), as obtained by subsequent TGA of the already thermally treated hybrid material in air (**Supplementary Figure S9**). This amount of SnO_2 (68.9 wt.%) in the rGO matrix is among the highest SnO_2 loads reported for such type of hybrid materials for battery applications.[35] This high load could only be achieved by the strong anchoring and the high density loading of SnO_2 crystals on top of the rGO sheets, as shown in **Figure 2**. Using a coalescent process, we were able to increase the SnO_2 loading (68.9 wt.% SnO_2) compared to the work of Liang *et al*.[35] (63 wt.% SnO_2) and Gao *et al*.[14] (53 wt.% SnO_2).

To investigate the electrochemical performance of these hybrid papers as free-standing electrodes, 8 mm discs were cut out and used directly as the anode in a Li half-cell. Such a free-standing material can be incorporated without any auxiliary current collector or additional preparation steps. **Figure 5** displays the evolution of the charging-discharging cycles as a function of charging rates and the corresponding measured capacities (**Figure 5b**). The hybrid papers exhibit a high initial capacity of 1730 mAh g^{-1} for the first discharge cycle whereas a significant drop in capacity for subsequent cycles was observed. Such drop in capacity was also

observed for similar materials and is caused by the formation of the solid electrolyte interface (SEI)[14] as well as due to the remaining free surface groups of not completely reduced graphene oxide. These surface groups undergo an irreversible reaction with the lithium, forming Li_2O, thus reduce the GO beyond the thermal treatment, which leads to a further increase in the material's electrical conductivity. This effect is confirmed by electrical impedance measurements (EIS), of which the Nyquist plot of cycle 1 indicates a larger resistance than the plots of the following cycles (**Figure 5c**). Complementary, the formation of the SEI is verified by CV analysis for 3 cycles (**Supplementary Figure S10**). Hereby, a large peak at 0.1 V indicates the formation of the SEI. During the first three cycles this peak is decreasing, demonstrating the irreversible nature of the SEI formation process.

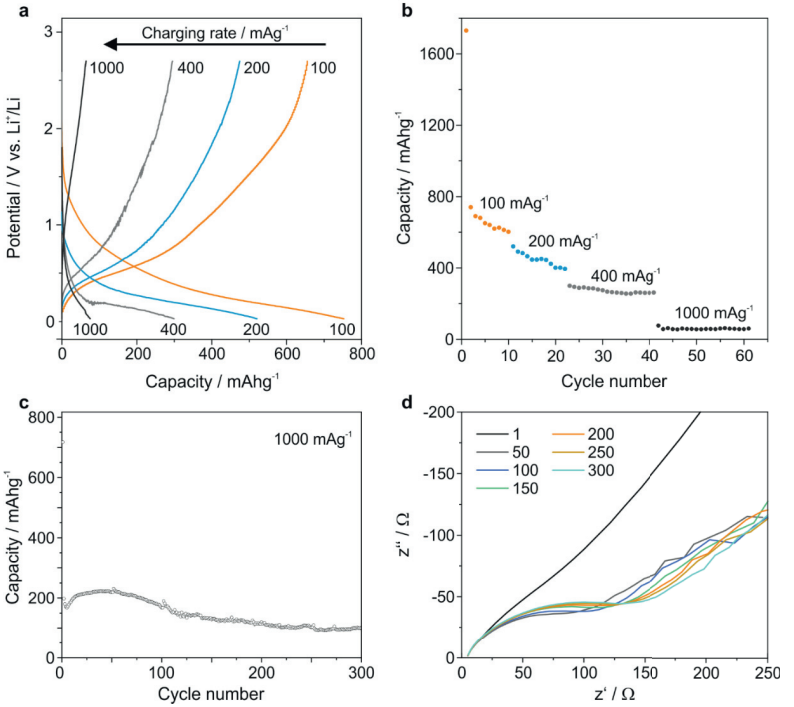

Figure 5. (a) Charge and discharge curves of the hybrid paper-like electrode for different charge/discharge rates (b) The discharge rate capability of the hybrid paper-like electrode for different charge/discharge rates for Li^+ battery cells. (c) 300 charge-discharge cycles of the paper-like hybrid material at a charging rate of 1000 mAg^{-1}, illustrating its stability and (d) the corresponding AC impedance measurements every 50th cycle

After the first cycle, consequent charging-discharging with a current rate of 100 mAg^{-1} yielded capacity values between 740 and 612 mAh g^{-1}. Increasing the charging rate, causes a decrease in capacity, as the latter is coupled to the diffusion kinetics of the Li^+ ions. However, even a four-fold increase in current led to a constant capacity of 300 mAh g^{-1}.

As not only the maximum capacity but also the cycling stability plays a major role for the hybrid materials application in LIBs, a 50 cycle charging/discharging measurement at a charging rate of 200 mAh g^{-1} was conducted (**Supplementary Figure S11**). It revealed a predominantly stable capacity over the 50 tested cycles with only a slight decrease. Although the SEM cross-section images of the hybrid papers before and after cycling do not exhibit significant structural changes, this decrease in capacity is most likely related to (i) formation and growth of the SEI and (ii) irreversible reactions on the rGO sheets and the SnO_2 nanoparticles.[4,28] In order to evaluate the long term stability of the hybrid electrode, we performed a charge/discharge measurement with a current rate of 1000 mAg^{-1}. The measurement revealed that the capacity of around 200 mAh g^{-1} is reached after five cycles and was retained over 100 cycles (**Figure 5c**), which demonstrates that even at such extremely high charging rates the material is electrochemically stable. The electrochemical stability is further confirmed by the EIS measurements conducted after every 50^{th} cycle. The Nyquist plot of the first cycle does not show a half cycle, indicating a significant resistance, whereat for the following cycles a half cycle was present. From the 50^{th} to the 300^{th} cycle, a stable performance of the electrode was observed with a slight increase in resistance after the 100^{th} cycle. This correlates well with the charge/discharge measurements, displayed in **Figure 5c**, indicating a decreasing capacity after 100 cycles. This decrease seems to be related to an increase in resistance for the electrode.

Only a limited number of groups reported comparable values of similar hybrid materials. Liu *et al.*[17] fabricated porous SnO_2/rGO nanocomposites, which exhibit good accessibility for Li^+ ions on the nanoscale. Excellent accessibility for Li^+ ions is present in the hybrid papers in our study, exhibiting a layered microstructure composed of rGO sheets separated by SnO_2 nanoparticles. However, the main difference of the material fabricated by Liu *et al.* and our materials is the electrode preparation. While Liu *et al.* needed to mix the porous SnO_2/rGO nanocomposites with carbon black and binder to obtain electrically conductive and mechanically stable conventional slurry, the hybrid papers can be directly used as an electrode, making further processing redundant. Compared to the values published by Liang *et al.*[35] obtained for the binder-free electrodes using commercial SnO_2 nanoparticles (average size of 50 nm) embedded

in rGO, the capacity of our hybrid papers was increased by nearly 20 %, from 500 mAh g^{-1} to 600 mAh g^{-1}. The strong interconnections between the SnO_2 nanocrystals and the rGO matrix support the electron transport throughout the complete volume of the electrode, which was responsible for the increased capacity. The latter also applies for SnO_2/rGO papers reported by Gao *et al.*[14] They achieved similar capacity values using a direct reaction of both components during the hydrothermal process. However, their fabrication procedure includes the chemical reduction of GO with $HBr_{(aq)}$ at elevated temperatures. In contrast, our method is not only facile, but also less toxic, due to the chemicals involved in the process, further underscoring the advantage of our hybrid papers.

3.3 Conclusions

Our research herein demonstrates the positive impact of coalescence in hybrid materials on their mechanical integrity and electrochemical performance. Sophisticated paper-like hybrid electrode can be fabricated by co-assembling $SnCl_x(OH)_yO_z$ precursor particles and GO sheets in a layered fashion and subsequent thermal treatment. The resulting paper comprises a matrix of rGO sheets with anchored SnO_2 nanocrystals. These nanocrystals have a size of up to 50 nm and act not only as electrochemical intercalation sites, but also as space holder between single rGO sheets, allowing the Li^+ ions to freely pass through the whole electrode. Simultaneously, the excellent interconnection between SnO_2 crystals and rGO sheets enables a fast transport of electrons. Both features enable the complete electrode material to partake in the electrochemical process, yielding capacities of up to 740 mAh g^{-1}. Additionally, the SnO_2 nanocrystals suppress the formation of multilayer rGO sheets during the reduction process at lower temperatures, preserving the mechanical flexibility of the papers. These identified key design principles can be further transferred to other hybrid electrode materials, which then are able to display good mechanical stability and flexibly in combination with excellent LIB performance.

3.4 Materials and Methods

Synthesis of the $SnCl_x(OH)_yO_z$ Precursor:

For the hydrothermal synthesis of $SnCl_x(OH)_yO_z$, $SnCl_2 \cdot 2\ H_2O$ (Sigma Aldrich, 6 mmol) was dissolved in 20 ml of a 1:1 water/ethanol mixture. The opaque white mixture was then stirred for 10 min and 39.5 ml of $NH_{3(aq)}$ (0.8 mol) were slowly added. The addition of ammonia led to a change in color from white to yellowish. After stirring the dispersion for additional 10 min, it was transferred to a PTFE (Teflon®) lined autoclave. Subsequently, the mixture was thermally treated for 6 h at 120 °C. The sample was taken out of the furnace after 24 h in total and transferred to a glass beaker. The subsequent washing steps included, (i) dispersing the product in a solvent (either MilliQ water or ethanol), (ii) centrifugation of the dispersed product in 50 ml flasks using an Eppendorf Centrifuge at 4000 rpm, (iii) decanting the respective solvent from the sedimented solid material and repeating steps (i) to (iii) whilst alternating the solvents (MilliQ water and ethanol) three times each.

Synthesis of the Graphene Oxide:

A modified Hummers' method[19] was employed to synthesize graphene oxide. Hereby, 0.5 g of graphite (NGS Naturgraphit GmbH) and 0.6 g KNO_3 (Sigma Aldrich) were mixed with 23 ml of concentrated H_2SO_4 (98 %) in a three-neck round bottom flask. The flask was kept for 10 min in an ice-bath at constant stirring. Subsequently, 3 g of $KMnO_4$ (Sigma Aldrich) was added, after which the mixture was heated to 35 °C and stirred for 6 h. After stirring, 40 ml of deionized water was added, the temperature increased to 80 °C, and held constant for 30 min under stirring. The oxidation of the intermediate formed graphene sheets was finally interrupted by slowly adding 100 ml deionized water and 3 ml of H_2O_2 (28 %) to the dispersion.

In order to increase the pH of the highly acidic (pH < 1) dispersion it was further diluted with deionized water and segregated with a high-speed centrifuge. 50 ml flasks were placed into an ultracentrifuge (Beckman-Coulter L-80 X) and spun at 15000 rpm for 10 min. Afterwards water and graphene oxide showed a visible phase separation, upon which the water was decanted. This procedure was repeated until a desired pH > 4 was reached. The residual acidic character of the GO dispersion is attributed to the remaining acidic surface groups on the single GO sheets.

Paper fabrication & Thermal Treatment:

The $SnCl_x(OH)_yO_z$ precursor powder was placed in a glass rosette cell and mixed in the respective ratio with an aqueous GO dispersion (6 mg ml^{-1}). This rosary cell was then exposed to ultrasound for 10 min with a pulse frequency of 0.5 Hz and a power of ~160 W (40 % of maximum power) using a sonotrode (Branson Sonifier 450). After pouring the dispersion into a 100 ml glass beaker and drying the sample over several days at room temperature, a paper-like hybrid material was removed from the bottom by pulling it off the bottom of the beaker. The paper-like hybrid material was thermally treated in argon atmosphere in a quartz tube furnace. A heating ramp of 4 $Kmin^{-1}$ was applied from room temperature (25 °C) to 500 °C. After the heating ramp the temperature was held for 2 hours and subsequently cooled with approximately 5 $Kmin^{-1}$ to 25 °C.

Structural Investigation:

Atomic force microscopy in tapping mode (AFM, Digital Instruments Multimode 9 with a NanoScope 5 controller) was used to image the structure of GO sheets. Scanning electron microscopy (SEM) was done on a Zeiss Ultra 55 Microscope at 5 kV. The samples were coated beforehand with 2 nm iridium to ensure proper conductivity. TEM investigations on single rGO sheets with SnO_2 nanocrystals were done on a Philips Electronic CM200 Microscope at 200 kV. Hereby, 0.215 mg of thermally treated paper-like material were placed into 20 ml ethanol and subsequently sonicated for 10 min. 1 ml of the dispersed paper-like material in ethanol was directly drop cast onto a TEM sample holder (Cu grid). XRD investigations were carried out in $\vartheta/2\vartheta$ Bragg-Brentano geometry on a RigakuSmartLab X-ray diffractometer with Cu-$K\alpha_{1,2}$ radiation. Cu-K_β radiation was filtered by a thin nickel foil (~90 % efficiency). TGA investigations were performed on NETZSCH STA 449F3 (SiC furnace) in flowing argon atmosphere with a heating rate of 4 K min^{-1} and in air with a heating rate of 30 K min^{-1} to determine the tin oxide content. All measurements were corrected for buoyancy effects. The FTIR spectra were recorded with a spectral resolution of ±2 cm^{-1} using a Bruker Tensor II spectrometer equipped with an ATR sensor. The data was handled using the spectroscopy software “OPUS”.

Electrochemical & Electrical Investigations:

The electrochemical investigations were performed on a Swagelok® cell with a CH Instruments Model 660C workstation (CHI software version 8.17) and a VSP-300 Module equipped with an impedance function on a BioLogic SAS system (software version V11.21). The electrode was

fabricated by punching an 8 mm diameter disk out of the thermally treated paper-like composite. As counter electrode Li-foil (99.8 wt.%, Sigma Aldrich), punched out in 8 mm diameter disk shape, and 1M $LiClO_4$ in 1:1 EC:DMC (ethylene carbonate:dimethyl carbonate) was used as the electrolyte. The assembly of all components and the consequent wetting with the electrolyte was done in an argon filled Glovebox (MBraun). Electrical conductivity was determined using a 4-point resistance measurement setup. Hereby, four gold contacts with a distance of 3 mm were sputtered onto the paper-like hybrid material using a mask. The resistance measurement was executed on a Keithley 2400 sourcemeter.

3.5 Acknowledgments

The authors are grateful to Department Spatz of the Max-Planck Institute for Intelligent Systems in Stuttgart, Germany, for providing access to SEM equipment. Additionally, we thank Efi Hadjixenophontos and the IMW II chair of the Institute for Materials Science at the University of Stuttgart for providing access to TEM equipment and Madu Batuwangala for his helpful corrections.

3.6 References

1. Armand, M.; Tarascon, J.-M. Building Better Batteries. *Nature,* 2008, *451*, 652–657.

2. Lu, L.; Han, X.; Li, J.; Hua, J.; Ouyang, M. A Review on the Key Issues for Lithium-Ion Battery Management in Electric Vehicles. *J. Power Sources,* 2013, *226*, 272–288.

3. Cooper, D. R.; D'Anjou, B.; Ghattamaneni, N.; Harack, B.; Hilke, M.; Horth, A.; Majlis, N.; Massicotte, M.; Vandsburger, L.; Whiteway, E.; Yu, V. Experimental Review of Graphene. *Int. Sch. Res. Not.,* 2012, *2012*, e501686.

4. Barré, A.; Deguilhem, B.; Grolleau, S.; Gérard, M.; Suard, F.; Riu, D.A. Review on Lithium-Ion Battery Ageing Mechanisms and Estimations for Automotive Applications. *J. Power Sources,* 2013, *241*, 680–689.

5. Goodenough, J. B.; Park, K.-S. The Li-Ion Rechargeable Battery: A Perspective. *J. Am. Chem. Soc.,* 2013, *135*, 1167–1176.

6. Jeong, M.-G.; Du, H. L.; Islam, M.; Lee, J. K.; Sun, Y.-K.; Jung, H.-G. Self-Rearrangement of Silicon Nanoparticles Embedded in Micro-Carbon Sphere Framework for High-Energy and Long-Life Lithium-Ion Batteries. *Nano Lett.,* 2017.

7. Alaf, M.; Gultekin, D.; Akbulut, H. Electrochemical Properties of Free-Standing Sn/SnO_2/Multi-Walled Carbon Nano Tube Anode Papers for Li-Ion Batteries. *Appl. Surf. Sci.,* 2013, *275*, 244–251.

8. Fujihara, S.; Maeda, T.; Ohgi, H.; Hosono, E.; Imai, H.; Kim, S.-H. Hydrothermal Routes To Prepare Nanocrystalline Mesoporous SnO_2 Having High Thermal Stability. *Langmuir,* 2004, *20*, 6476–6481.

9. Choi, S.; Kwon, T.; Coskun, A.; Choi, J. W. Highly Elastic Binders Integrating Polyrotaxanes for Silicon Microparticle Anodes in Lithium Ion Batteries. *Science,* 2017, *357*, 279–283.

10. Hoshide, T.; Zheng, Y.; Hou, J.; Wang, Z.; Li, Q.; Zhao, Z.; Ma, R.; Sasaki, T.; Geng, F. Flexible Lithium-Ion Fiber Battery by the Regular Stacking of Two-Dimensional Titanium Oxide Nanosheets Hybridized with Reduced Graphene Oxide. *Nano Lett.,* 2017, *17*, 3543–3549.

11. Chen, K.-S.; Xu, R.; Luu, N. S.; Secor, E. B.; Hamamoto, K.; Li, Q.; Kim, S.; Sangwan, V. K.; Balla, I.; Guiney, L. M.; Seo, Y.W.T.; Yu, X.; Liu, W.; Wu, J.;Wolverton, C., Dravid, V.; Barnett, S.; Lu, J.; Amine, K.; Hersam, M.C. Comprehensive Enhancement of Nanostructured Lithium-Ion Battery Cathode Materials *via* Conformal Graphene Dispersion. *Nano Lett.,* 2017, *17*, 2539–2546.

12. Demirocak, D. E.; Srinivasan, S. S.; Stefanakos, E. K. A Review on Nanocomposite Materials for Rechargeable Li-Ion Batteries. *Appl. Sci.,* 2017, *7*, 731.

13. Ranjbartoreh, A. R.; Wang, B.; Shen, X.; Wang, G. Advanced Mechanical Properties of Graphene Paper. *J. Appl. Phys.,* 2011, *109*, 014306.

14. Gao, T.; Huang, K.; Qi, X.; Li, H.; Yang, L.; Zhong, J. Free-Standing SnO_2 Nanoparticles@graphene Hybrid Paper for Advanced Lithium-Ion Batteries. *Ceram. Int.,* 2014, *40*, 6891–6897.

15. Guo, P.; Song, H.; Chen, X. Electrochemical Performance of Graphene Nanosheets as Anode Material for Lithium-Ion Batteries. *Electrochem. Commun.,* 2009, *11*, 1320–1324.

16. Zhang, W.-J. A Review of the Electrochemical Performance of Alloy Anodes for Lithium-Ion Batteries. *J. Power Sources,* 2011, *196*, 13–24.

17. Liu, C.; Wang, P.; Du, C.; Li, L.; Yin, G.; Zuo, P.; Cheng, X. Hydrothermal Self-Assembly Synthesis of Porous SnO_2/Graphene Nanocomposite as an Anode Material for Lithium Ion Batteries. *J. Nanosci. Nanotechnol.,* 2017, *17*, 1877–1883.

18. Pei, S.; Cheng, H.-M. The Reduction of Graphene Oxide.*Carbon,* 2012, *50*, 3210–3228.

19. Hummers, W. S.; Offeman, R. E. Preparation of Graphitic Oxide. *J. Am. Chem. Soc.,* 1958, *80*, 1339–1339.

20. Dikin, D. A.; Stankovich, S.; Zimney, E. J.; Piner, R. D.; Dommett, G. H. B.; Evmenenko, G.; Nguyen, S. T.; Ruoff, R. S. Preparation and Characterization of Graphene Oxide Paper. *Nature,* 2007, *448*, 457–460.

21. Wang, X.; Zhi, L.; Müllen, K. Transparent, Conductive Graphene Electrodes for Dye-Sensitized Solar Cells. *Nano Lett.,* 2008, *8*, 323–327.

22. Zuo, X.; Zhu, J.; Müller-Buschbaum, P.; Cheng, Y.-J. Silicon Based Lithium-Ion Battery Anodes: A Chronicle Perspective Review. *Nano Energy,* 2017, *31*, 113–143.

23. Deng, Y.; Fang, C.; Chen, G. The Developments of SnO_2/Graphene Nanocomposites as Anode Materials for High Performance Lithium Ion Batteries: A Review. *J. Power Sources,* 2016, *304*, 81–101.

24. Huang, Z.-D.; Zhang, K.; Zhang, T.-T.; Liu, R.-Q.; Lin, X.-J.; Li, Y.; Feng, X.-M.; Mei, Q.-B.; Masese, T.; Ma, Y.-W.; Huang, W. Binder-Free Graphene/Carbon Nanotube/Silicon Hybrid Grid as Freestanding Anode for High Capacity Lithium Ion Batteries. *Compos. Part Appl. Sci. Manuf.,* 2016, *84*, 386–392.

25. Prabakar, S. J. R.; Hwang, Y.-H.; Bae, E.-G.; Shim, S.; Kim, D.; Lah, M. S.; Sohn, K.-S.; Pyo, M. SnO_2/Graphene Composites with Self-Assembled Alternating Oxide and Amine Layers for High Li-Storage and Excellent Stability. *Adv. Mater.,* 2013, *25*, 3307–3312.

26. Zhu, J.; Lei, D.; Zhang, G.; Li, Q.; Lu, B.; Wang, T. Carbon and Graphene Double Protection Strategy to Improve the SnO_x Electrode Performance Anodes for Lithium-Ion Batteries. *Nanoscale,* 2013, *5*, 5499–5505.

27. Ye, Y.; Wang, P.; Dai, E.; Liu, J.; Tian, Z.; Liang, C.; Shao, G. A Novel Reduction Approach to Fabricate Quantum-Sized SnO_2 -Conjugated Reduced Graphene Oxide Nanocomposites as Non-Enzymatic Glucose Sensors. *Physical Chemistry Chemical Physics,* 2014, *16*, 8801–8807.

28. Wang, B.; Ryu, J.; Choi, S.; Song, G.; Hong, D.; Hwang, C.; Chen, X.; Wang, B.; Li, W.; Song, H.-K.; Park, S.; Ruoff, R.S. Folding Graphene Film Yields High Areal Energy Storage in Lithium-Ion Batteries. *ACS Nano,* 2018, *12*, 1739–1746.

29. R. Dreyer, D. Park, S.; W. Bielawski, C.; S. Ruoff, R. The Chemistry of Graphene Oxide. *Chem. Soc. Rev.,* 2010, *39*, 228–240.

30. Jalili, R.; Aboutalebi, S. H.; Esrafilzadeh, D.; Shepherd, R. L.; Chen, J.; Aminorroaya-Yamini, S.; Konstantinov, K.; Minett, A. I.; Razal, J. M.; Wallace, G. G. Graphene Oxide: Scalable One-Step Wet-Spinning of Graphene Fibers and Yarns from Liquid Crystalline Dispersions of Graphene Oxide: Towards Multifunctional Textiles (Adv. Funct. Mater.43/2013). *Adv. Funct. Mater.,* 2013, *23*, 5344–5344.

31. Wang, B.; Su, D.; Park, J.; Ahn, H.; Wang, G. Graphene-Supported SnO_2 Nanoparticles Prepared by a Solvothermal Approach for an Enhanced Electrochemical Performance in Lithium-Ion Batteries. *Nanoscale Res. Lett.* 2012, *7*, 215.

32. Baur, W. H.; Khan, A. A. Rutile-Type Compounds. IV. SiO2, GeO_2 and a Comparison with Other Rutile-Type Structures. *Acta Crystallogr. B,* 1971, *27*, 2133–2139.

33. Acik, M.; Lee, G.; Mattevi, C.; Pirkle, A.; Wallace, R. M.; Chhowalla, M.; Cho, K.; Chabal, Y. The Role of Oxygen during Thermal Reduction of Graphene Oxide Studied by Infrared Absorption Spectroscopy. *J. Phys. Chem. C,* 2011, *115*, 19761–19781.

34. Moreno, M. S.; Punte, G.; Rigotti, G.; Mercader, R. C.; Weisz, A. D.; Blesa, M. A. Kinetic Study of the Disproportionation of Tin Monoxide. *Solid State Ion.,* 2001, *144*, 81–86.

35. Liang, J.; Zhao, Y.; Guo, L.; Li, L. Flexible Free-Standing Graphene/SnO_2 Nanocomposites Paper for Li-Ion Battery. *ACS Appl. Mater. Interfaces,* 2012, *4*, 5742–5748.

36. Gao W. The Chemistry of Graphene Oxide, *Springer* 2015*, Cham*

37. A. Ayeshamariam, S. Ramalingam, M. Bououdina, M. Jayachandran, Preparation and characterizations of SnO_2 nanopowder and spectroscopic (FT-IR, FT-Raman, UV–Visible and

NMR) analysis using HF and DFT calculations, *Spec. chim. Acta A: Molecular and Biomolecular Spectroscopy,* 2014, 118, 1135

38. John A. Dean, Lange's Handbook of Chemistry, 15th ed., McGraw-Hill Inc., New York, 1999.

3.7 Supporting Information

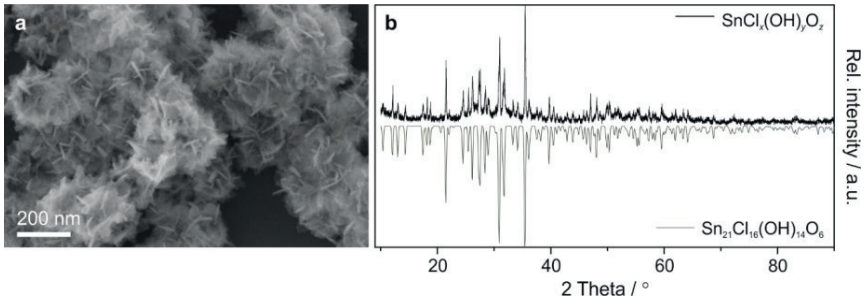

Figure S1. (a) SEM image showing small platelets of $SnCl_x(OH)_yO_z$ together with (b) a measured XRD pattern of $SnCl_x(OH)_yO_z$ (top) and simulated pattern (bottom) of $Sn_{21}Cl_{16}(OH)_{14}O_6$ (ICDD Ref Code.: 00-039-0314).

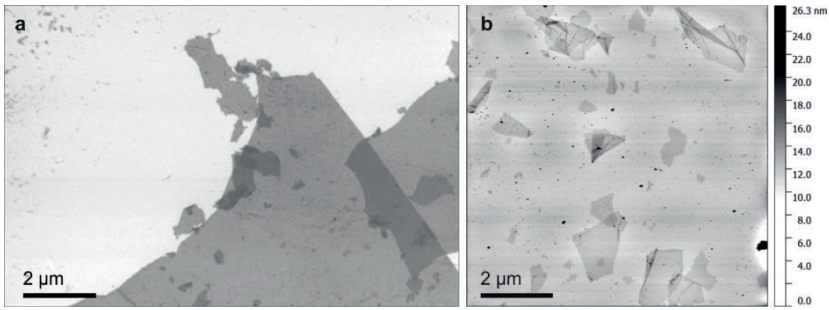

Figure S2. (a) SEM and (b) AFM images of single rGO nanosheets deposited on a Si wafer.

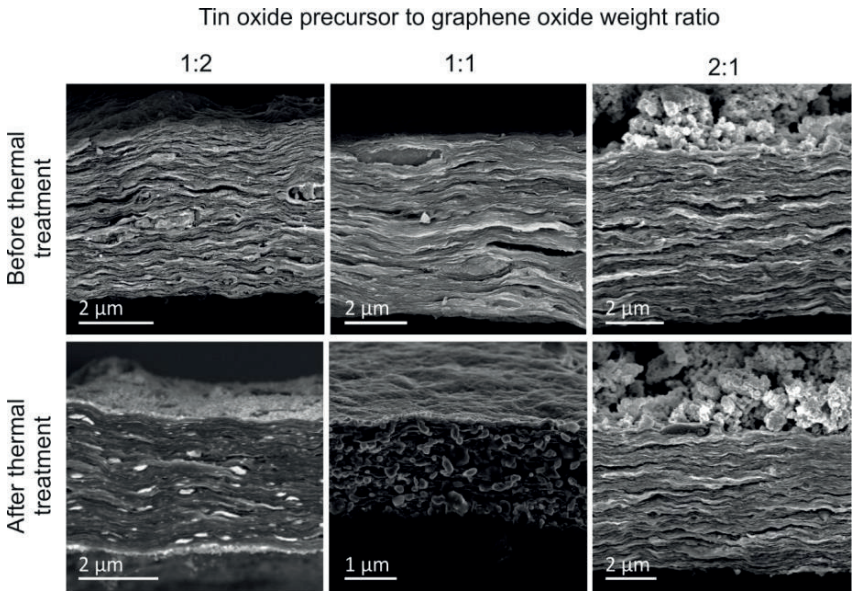

Figure S3. SEM images of hybrid papers with different compositions before and after thermal treatment.

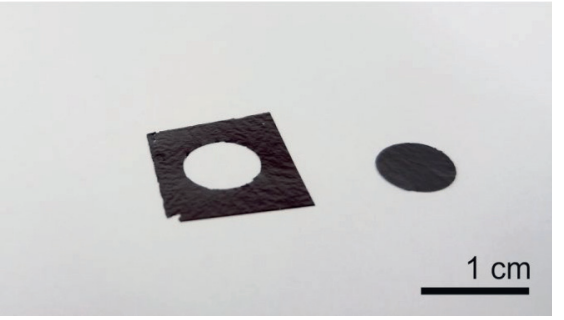

Figure S4. An 8 mm in diameter punched out disk of the electrode without any structural damages. This electrode is used as it is as binder-free anode in the Swagelok cell.

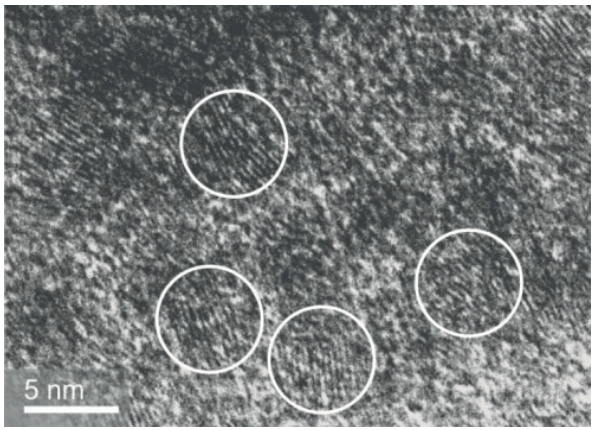

Figure S5. HRTEM image of crystals (white circle) with preferred texture on a sheet of rGO. Crystals with a size of up to 10 nm were observed.

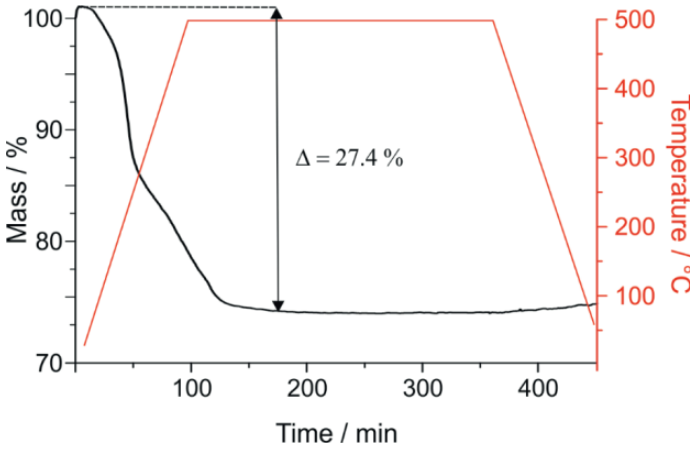

Figure S6. TGA curve displaying the annealing of the $SnCl_x(OH)_yO_z$/GO hybrid papers under argon atmosphere.

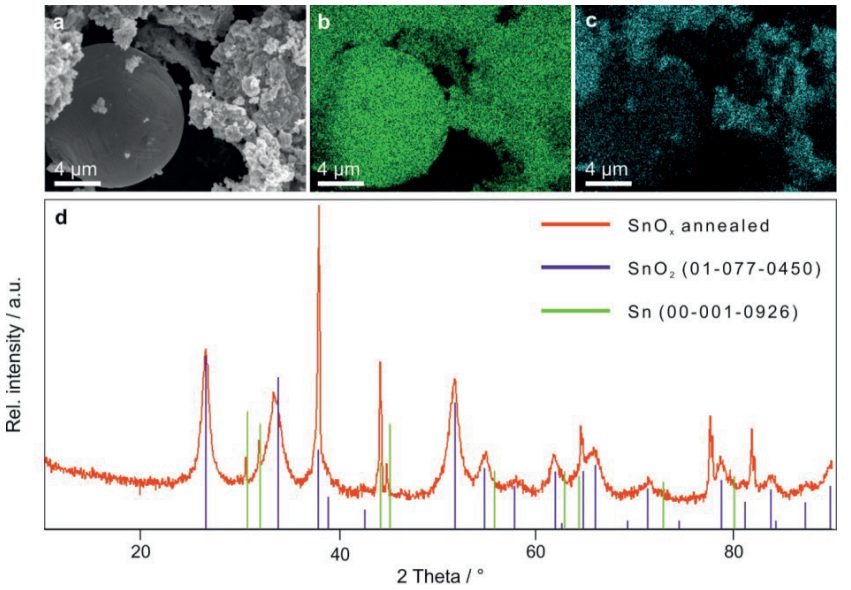

Figure S7. (a) SEM image of a selected sample area of the $SnCl_x(OH)_yO_z$ precursor, which was annealed in the absence of GO. A disproportionation of the precursor is clearly visible by comparing the EDX tin mapping (b, green) with the oxygen mapping (c, cyan). The spherical particle appears to contain only Sn, whereas increased oxygen content is observed for the surrounding agglomerates. (d) The disproportionation was additionally confirmed by the collected PXRD data, showing the presence of Sn and SnO_2. The respective ICDD data set numbers of the reference patterns are stated in the figure.

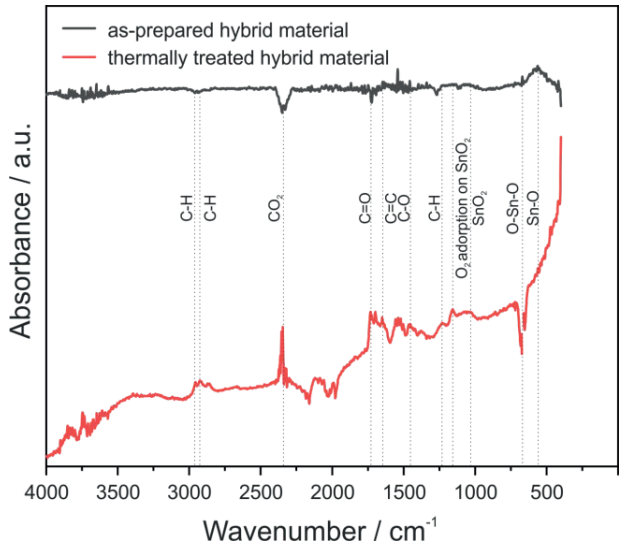

Figure S8. FTIR spectra of the hybrid paper before and after thermal treatment.

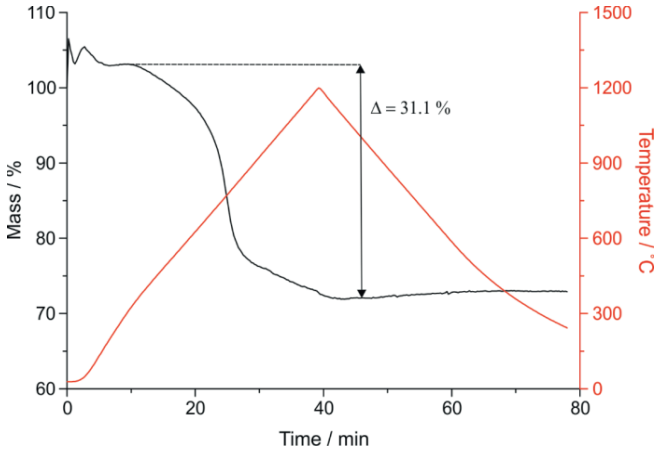

Figure S9. TGA curve displaying the annealing of the SnO_2/rGO hybrid papers in air. The measured mass loss allows calculating the final weight ratio of the two constituents.

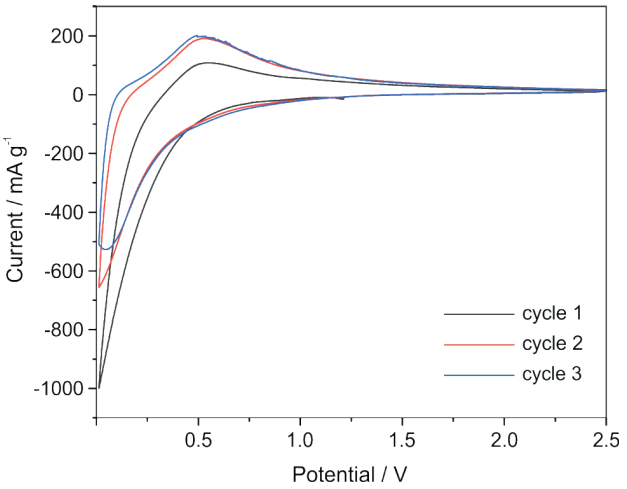

Figure S10. CV analysis of the SnO_2/r-GO paper-like hybrid material, displaying the irreversible processes occurring during the first cycles.

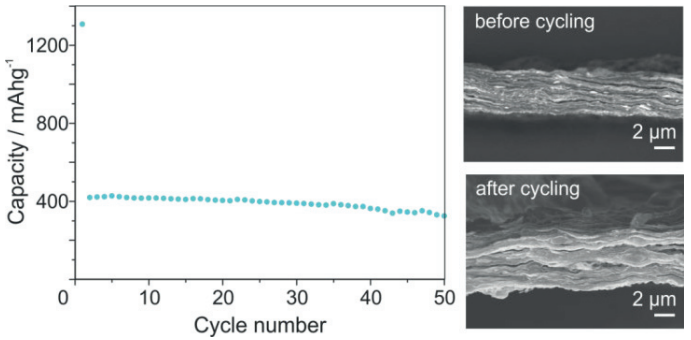

Figure S11. Measured capacity of the SnO_2/rGO electrode measured using a current rate of 200 mAh g^{-1} and a voltage window of 0.125 V and 2.7 V.

4. Highly Porous Free-standing rGO/SnO_2 Pseudocapacitive Cathodes for High-Rate and Long-Cycling Al-Ion Batteries

(reprinted with permission of MDPI 2020)

Timotheus Jahnke, Leila Raafat, Daniel Hotz, Andrea Knöller, Achim Max Diem,

*Joachim Bill, Zaklina Burghard**

Abstract

Establishing energy storage systems beyond conventional lithium ion batteries requires the development of novel types of electrode materials. Such materials should be capable of accommodating ion species other than Li^+, and ideally, these ion species should be of multivalent nature, such as Al^{3+}. Along this line, we introduce a highly porous aerogel cathode composed of reduced graphene oxide, which is loaded with nanostructured SnO_2. This binder-free hybrid not only exhibits an outstanding mechanical performance, but also unites the pseudocapacity of the reduced graphene oxide and the electrochemical storage capacity of the SnO_2 nanoplatelets. Moreover, the combination of both materials gives rise to additional intercalation sites at their interface, further contributing to the total capacity of up to 16 mAh cm^{-3} at a charging rate of 2 C. The high porosity (99.9 %) of the hybrid and the synergy of its components yield a cathode material for high-rate (up to 20 C) aluminium ion batteries, which exhibit an excellent cycling stability over 10 000 tested cycles. The here proposed electrode design has a great potential to meet future energy- and power density demands for advanced energy storage devices.

4.1 Introduction

Electrochemical energy storage systems based on lithium ions are nowadays a well-established concept, which enables the application of a broad spectrum of technologies, ranging from microelectronics over portable electronic devices to even electrical cars. Such lithium ion batteries (LIBs) offer an excellent energy density and long-term stability. However, the limited lithium resources paired with its high cost and safety hazards make LIBs only a medium-term solution. In the long term, sustainable alternatives, *e.g.* other metal ion batteries,[1] are more favorable. Researchers have been investigating monovalent ion batteries, like sodium and potassium based electrochemical systems as alternatives,[2,3] due to the high abundance and cost efficiency of these elements. However, larger monovalent ions usually have a sluggish diffusivity and lower intercalation voltages at similar energy densities (one electron per ion transfer). In order to improve the energy density of an active material, electrochemical systems based on multivalent ion exchange have been in discussion among researchers.[4,5] Among them, aluminum-based electrochemical systems have become one of the most promising candidates, owing to the aluminum's natural abundance, low cost and inherent safety.[6–9] Moreover, the three-valent aluminum could significantly boost the energy storage capacity compared to the single-valent lithium.[10]

Establishing aluminum ion batteries (AIBs) requires the development of suitable electrolytes and tailored electrode materials. Imidazole-based ionic-liquids have already been identified as suitable electrolytes, as they exhibit a low inner resistance, high solubility of the aluminum salt $AlCl_3$ and good electrochemical stability.[11] The search for cathode materials, however, is still ongoing and among the most discussed current topics in this field.[7,12] One fundamental requirement for such a material is its capability to intercalate Al^{3+} ions or chloroaluminate ions at a relatively high operating potential.[7] In this respect, a promising candidate is graphite, with its layered structure that facilitates the access of intercalating ions and provides sufficient space for them. Specifically, it was demonstrated that graphite based materials immersed in an imidazole-based electrolyte deliver storage capacities of up to 60 mAh g^{-1} at a high current density of up to 2 A g^{-1}.[13] Other carbon-based materials, such as carbon nanotubes or graphene /reduced graphene oxide (rGO), have been likewise tested as electrode material for AIBs.[7,8,14–17] A storage capacity between 60 to 150 mAh g^{-1} could be achieved due to the reversible intercalation of chloroaluminate ions. Regarding rGO electrodes, electrochemical characterization further revealed an extremely high charging capability of up to 20 A g^{-1},

delivering capacities stable over thousands of cycles.[16] This enhanced electrochemical performance could be ascribed to the material's pseudocapacitive behavior,[18] which arises from the adsorption of chloroaluminate ions onto its surface. The micro/mesoporosity and large specific surface area promote thereby the pseudocapacity, thus enable a full charging process in minutes or even seconds.

A substantial advantage of pseudocapacitive materials, such as rGO, is that the main contribution to their energy storage capability is attributed to the ion adsorption rather than the bulk ion-diffusion, i.e. de-/intercalation. However, in comparison to LIBs, the intercalation or adsorption of negatively charged aluminum complexes in graphitic materials is still relatively low concerning their gravimetric capacity (< 150 mAh g^{-1}) and the energy density (< 0.3 Wh g^{-1}).[16] In addition to graphitic materials, electrochemically active materials, such as sulphur,[19,20] sulphides,[21-25] and oxides,[26–28] were investigated for their applicability in AIBs. Even though they showed great potential in terms of their electrochemical storage capacity, they often lacked in cycling stability or electrical conductivity, leading to capacity fading and short cycle life.[12] Among the oxides, tin oxide (SnO_2) stands out due to its high specific capacity (434 mAh g^{-1}),[28] good electrical conductivity (1 – 100 Ω^{-1} cm^{-1}),[29, 30] and wide availability though, has been sparsely investigated. Nevertheless, the combination of carbon based materials and SnO_2 has been reported and investigated for LIBs.[31,32] The integration of SnO_2 nanostructures into a flexible carbon based matrix has an essential impact of the electrodes performance and can be achieved for example by thermal post treatment.[33]

In order to unite the main properties of pseudocapacitors with those of batteries, thus fast charging rates and good cycling stability with a high storage capacity, the fabrication of hybrid electrodes presents great potential. Moreover, tailoring the hybrid electrode's microstructure to maximize the specific surface area and shorten the diffusion paths could further boost the synergy of ion adsorption and intercalation. In this work, we therefore united pseudocapacitive rGO nanosheets with electrochemically active SnO_2 nanoplatelets in highly porous, binder-free aerogel electrodes. Their applicability as cathodes in novel AIBs was tested with respect to their mechanical and electrochemical performance. This work shows that tailoring the porosity and surface area of carbon-based electrode materials in combination with an electrochemically active material, enhances the mechanical stability and the pseudocapacitive performance in AIB.

4.2 Materials and Methods

Fabrication of the single components

Graphene oxide was synthesized employing a modified Hummers method.[34] Here, 0.5 g graphite flakes (NGS Naturgraphit GmbH) and 0.6 g KNO_3 (Sigma Aldrich) were added to 23 ml of H_2SO_4 (Sigma Aldrich, 98 %) in a three-neck, round bottom flask, which is placed in an ice bath. Constant stirring for 10 minutes was applied to ensure a good dispersion of the graphite flakes in the H_2SO_4, whereas afterwards 3 g $KMnO_4$ (Sigma Aldrich) was added, and the temperature adjusted to 35 °C and held for 6 h, whilst continuing the stirring. Subsequently, 40 ml of dd-H_2O was dropwise added, the temperature rose to 80 °C and was held for 30 minutes. The reaction was interrupted by adding slowly 100 ml dd-H_2O and 3 ml H_2O_2 to the dispersion.

In order to remove the residual reagents and increase the highly acidic pH (< 1), the GO dispersion was centrifuged (SORVALL RC6) for 10 minutes at 17 000 relative centrifugal force. The transparent portion in the flask was decanted after centrifugation, dd-H_2O added, shortly stirred up and then centrifuged again. This process was repeated at least 10 times, until the pH was above four. The small GO sheets where obtained from IoLiTec with an initial concentration of 5 mg ml^{-1}.

The SnO_2 nanoparticles were synthesized using a common hydrothermal approach with $SnCl_2$ salt and ammonia as initial reagents.[35] 1.36 g $SnCl_2$*$2H_2O$ were dissolved in 10 ml dd-H_2O and 10 ml Ethanol (Sigma Aldrich, p.a.) for 10 minutes. Subsequently, 24 ml of 0.55 M ammonia solution was added slowly mixture, which turns opaque-yellow upon the addition of ammonia. Consequently, the mixture was transferred to a 25 ml Teflon-lined autoclave and hydrothermally treated for 6 hours at 120 °C. The material was finally washed alternatingly three times with ethanol and 3 times with dd-H_2O to obtain a clean powder.

Ice-templating and annealing

In order to obtain the hybrid composed of rGO and SnO_2, an aqueous dispersion of the respective GO sheets (66.6 wt.%) was mixed with SnO_2 nanoparticles (33.3 wt.%) and sonicated for 10 minutes in an ultrasonic bath with a 90 W power supply. The dispersion was then transferred into a PTFE mold, which was placed beforehand on the cold finger, and frozen by applying a unidirectional temperature gradient of 18.5 K mm^{-1} in z-direction. To this end, self-supporting aerogels, with a radius of 4 mm and a height of 8 mm and a porosity of > 99.9 %

were obtained. These self-supporting aerogels were transferred into the freeze drier (L10E, Dieter Piatkowski), which was cooled down to - 50 °C before evacuation. After the removal of the ice crystals, the aerogels were reduced in a quartz tube furnace in Argon (99.95 Ar), ramping with 4 K min^{-1} to 500 °C, at which they were kept for two hours. The obtained hybrid aerogels had a 41 wt.% rGO to 59 wt.% SnO_2 weight ratio and a weight around 1.55 mg ± 0.03 mg, whereas the pure rGO aerogels had a weight of 0.748 mg ± 0.002 mg, obtained from weight measurements on three samples each.

Microstructural characterization

For microstructural investigations, scanning electron microscopy (Zeiss Ultra 55) was used. X-ray diffraction was performed on a Bruker D8 system using copper K_α radiation in the range of 10-90° with 0.01° as step size. The crystallite size was calculated using Scherrers equation with a form factor of 1 and a Full-Width-Half-Maximum of 1.87 theta around a Bragg Angle of 26.59 deg. Brunauer-Emmett-Teller (BET) tests were performed on a physisorption analyser (Quantachrome Instruments Autosorb iQ3).

Mechanical characterization

The mechanical measurements were conducted on a Bose Electroforce, specifically the 3220-AT Serie III Model, equipped with a 5 mN load cell. In order to investigate the porous foams, glass plates were glued on the bottom and the cross head and the sample was placed between them. The measurement was performed first with a compression step with a strain rate of 0.015 mm s^{-1} up to 75 % compression, followed by a release-step with the strain rate of 0.015 mm s^{-1} down to 0 % compression.

Electrochemical characterization

The cell assembly was performed in an argon filled glovebox (Labmaster SP, MBraun) and VWR connections made of PTFE with an inner diameter of 10.5 mm were used as cell housing. In order to avoid corrosion on the contacts, molybdenum rods were milled from pure molybdenum (99.95 wt.% Mo) rods to until they had a diameter of 10.5 mm and fit tightly into the housing. Additionally, the contacts were wrapped with PTFE sealing tape, to exclude any influence of oxygen. The respective aerogel was placed on one side of the contact and six glass fiber separators (Grade 934-AH, Whatman) with a diameter of 11 mm on top. 1-Ethyl-3-methylimidazolium chloride mixed with aluminum chloride in the ratio of 1:1.3 (IoLiTec, Ionic Liquid Technologies) was determined to be a suitable electrolyte. The separators and the

aerogel were soaked with electrolyte (0.2 ml) and compressed using the other Mo contact as stamp. As counter electrode aluminum foil (99.99 at.% Al) was used. Galvanostatic charge/discharge tests were performed at a current density of 100, 1000 and 2000 mA g^{-1} in the voltage range of 0.2-2.0 V for the composite and 0.2 to 2.2 V for the rGO aerogel. Prior to testing, the cells sat for at least two hours to completely saturate the aerogel with electrolyte. Cyclic voltammetry was performed in a voltage window of 0.02-2.2 V, with a sweep rate of 0.1, 1, 10, 20, 50 and 100 mV s^{-1} for both aerogels. All measurements were performed on electrochemical test stations (VMP300, Biologic).

4.3 Results and Discussion

Fabrication of the porous, binder-free rGO/SnO_2 aerogels

Graphene oxide (GO) sheets were fabricated using a modified Hummers method,[34] resulting in sheet sizes ranging from 2 to 20 µm (**Supporting Figure S1a**). The SnO_2 nanoplatelets were synthesized by a hydrothermal approach.[35] Their dimensions were determined by scanning electron microscopy (SEM), revealing a thickness of a few nanometers and a lateral dimension of several tens of nanometers, with a tendency to form agglomerates with a size of 100 nm (**Supporting Figure S1b**).

The hybrid electrode was fabricated by adding SnO_2 nanoplatelets to an aqueous dispersion of the GO sheets, thereby soft sonication treatment was performed to ensure a homogenous distribution (**Figure 1**) and exfoliation of GO sheets. Subsequently, the components were co-assembled by an ice-templating process. Ice crystals propagate thereby in a unidirectional manner along the applied temperature gradient in z-direction and thus restrict the solid load between them (**Supporting Figure S2**). Their subsequent sublimation, i.e. freeze-drying, leaves a highly porous, channel-like microstructure behind, in which the columnar pores are the replica of the removed ice crystals.[36] Such an ice-templating technique enables aligned, continuous channels throughout the whole height of the cylindrical aerogel. For the performance evaluation, aerogels composed solely of GO were fabricated, using the same concentration of GO in aqueous dispersion as that used for the hybrid electrode aerogel.

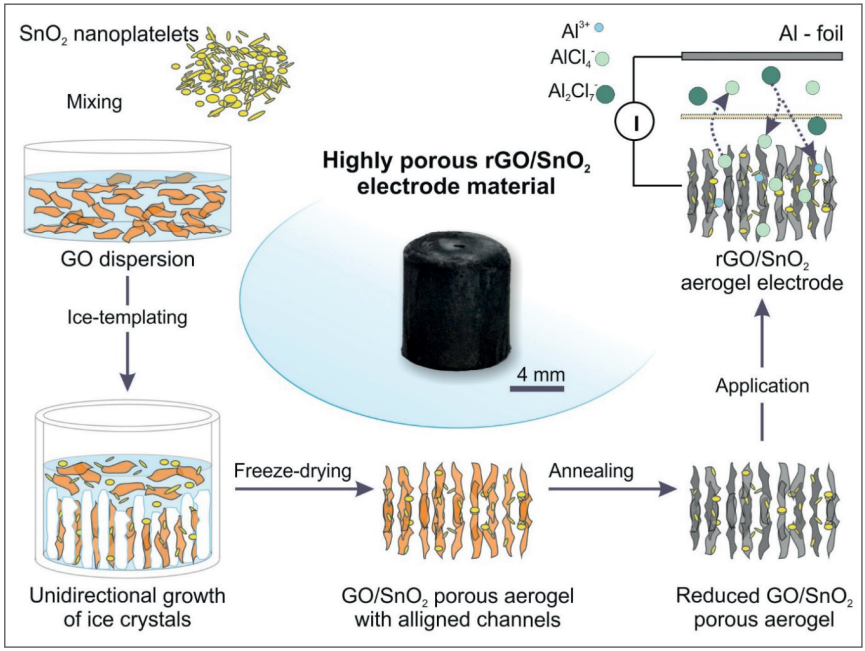

Figure 1. Schematic illustration of the fabrication process of free-standing highly porous rGO/SnO_2 aerogels and their application as a cathode material in AIBs.

The final step towards the fabrication of rGO/SnO_2 hybrid electrodes for AIBs (**Figure 1**) is annealing the aerogel to thermally reduce the GO. In this step, it is crucial to choose a slow heating rate to avoid fast gas evolution, which would lead to structural damages. To verify the structural preservation after annealing of the aerogels, pristine and hybrid, the microstructure was investigated by SEM in its original (**Supporting Figure S3**) and reduced state (**Figure 2**). To that end, a honeycomb-like pore structure is observed at the cross-section of the as-prepared and reduced aerogels (**Figure 2a,d** and **Supporting Figure S3a,d**), with a pore width in the range of 20 to 40 µm. From the longitudinal cross sections, the aligned pore channels are notable and a wall porosity in the range of tens of micrometers is revealed (**Figure 2b,e** and **Supporting Figure S3b,c,e**). The latter arises from local inhomogeneities of solid load between the ice-crystals,[37] coupled with the lateral size of the GO sheets, which is up to one magnitude smaller than the diameter of the ice crystals / channels. Moreover, a connection between the channels

is observed in the longitudinal section (**Figure 2c**). The microstructural features identified for the aerogels are typical for ice-templated carbon materials.[38–40] Additionally, regarding the hybrid, agglomerates of SnO_2 nanoplatelets could be detected, which are wrapped between the GO sheets, asserting the co-assembly of both materials (**Figure 2f** and **Supporting Figure S3f** and **S4**). The striking similarity of the as-prepared and reduced aerogels' microstructure assured therefore the minimal impact of the thermal treatment.

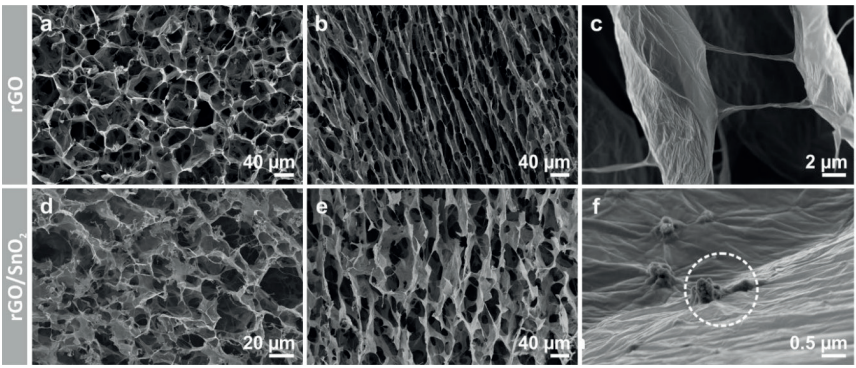

Figure 2. SEM images of the microstructures of rGO and rGO/SnO_2 aerogels (a, d) top view and (b, e) side view of the channels. Detailed view of the (c) GO walls and (f) the SnO_2 nanoplatelets embedded in the walls.

However, upon thermal treatment a weight loss of 26 % occurred, which is assigned to the removal of oxygen-containing functional groups and their reaction to gaseous CO and CO_2.[41] A hybrid composition of 41 wt.% rGO and 59 wt.% SnO_2 is thereby obtained as deducted from thermogravimetric analysis (**Supporting Figure S5**). Moreover, highly conductive rGO is achieved due to the restoration of the sp2-hybridization characteristic of graphene.[42] The removal of the oxygen-containing functional groups is further accompanied by a decrease in interlayer distance of neighboring sheets.[43] The powder X-ray diffraction (XRD) patterns of the hybrid aerogels, as-prepared and reduced, revealed a shift of the reflection at 11° for GO to 24° for rGO (**Figure 3a, b**). The reflection at around 11° originates from stacked GO, as it correlates with the pristine GO material. The shift therefore corresponds to a decrease in interlayer distance from 0.8 nm to 0.4 nm, which is close to the value of the interlayer distance in graphite (0.33 nm).[44] This correlates to the results obtained by Raman, where an increase in the D- to G-band ratio is observed (**Supporting Figure S6**). Additionally, a peak broadening is observed

for rGO, which correlates to a small crystallize size in the sheets.[16] Similarly, the same shift upon reduction is observed for the hybrid as a shoulder at 24° next to the reflection of SnO_2, indicating a decrease in layer distance of overlapping rGO sheets, which are located in the walls of the aerogel. However, the intensity of the shoulder is significantly lower and broader, compared to SnO_2, indicating a smaller diffracted crystal volume of rGO stacks as schematically presented in **Figure 3b**. This reduction in intensity is correlated with the decreased number of stacked rGO sheets, because SnO_2 particles are embedded between them hindering the restacking of rGO single sheets during removal of oxygen containing surface groups (see schematic in **Figure 3b**). XRD analysis shows that the SnO_2 nanoplatelets are nanocrystalline and exhibit a rutile structure, known as a good intercalation host.[36,45–47] After reduction, these rutile reflections of SnO_2 become more pronounced, indicating a crystal growth of the originally agglomerated nanostructured platelets into larger crystals (**Supporting Figure S4**). The crystallite size of the SnO_2 nanostructures was calculated using Scherrer's equation as 6.33 nm.

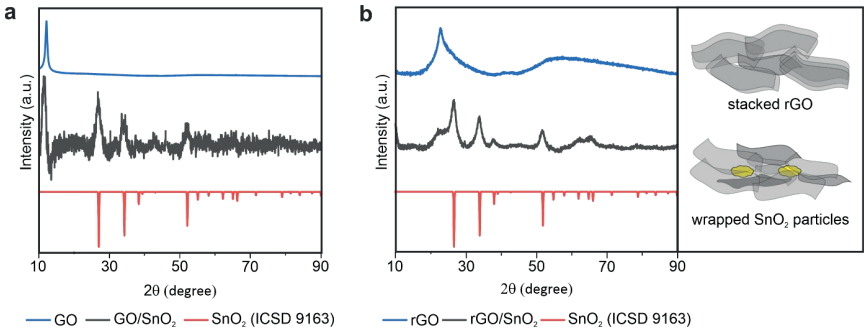

Figure 3. XRD pattern of the (a) GO/SnO_2 and (b) rGO/SnO_2 hybrid aerogel with a schematic presentation of rGO sheets arrangement with and without SnO_2 particles.

Brunauer-Emmett-Teller (BET) measurements were performed on the pristine as well as the hybrid aerogels to determine their surface area and mesoporosity, as these features are known to highly influence the electrochemical performance of the active material.[16] A large surface area of 221.3 $m^2\ g^{-1}$ in case of the hybrid rGO/SnO_2 was thereby determined, 60 % of that of the pristine rGO aerogel (367.9 $m^2\ g^{-1}$). The presence of mesoporosity was also verified by the obtained N_2 adsorption-desorption isotherms, exhibiting a hysteresis form (**Supporting Figure S7**).[48] This result is in good agreement with the presented microstructure (**Figure 2b,e**), revealing the location of the mesopores within the cell walls. However, the mesoporosity of the

pristine aerogels is almost 2-fold of the hybrid aerogels, as concluded from the cumulative pore volume of 0.47 $cm^3 g^{-1}$ in case of the pristine and 0.24 $cm^3 g^{-1}$ in case of the hybrid aerogel (**Supporting Figure S7b**). However, considering the significantly higher density of the hybrid aerogel (5.0 g cm^{-3}) an even larger cumulative pore volume fraction is achieved. Furthermore, the overall porosity $P = 1 - \rho_s/\rho * 100$ % is estimated to 99.9 % for both aerogels, pristine and hybrid based on the density of carbon[44] ρ = 2.26 g cm^{-3} and that of the aerogel ρ_s. The scaffold structure, with its channel-like pores, is the major contributor to this high porosity. Notably, the tailored microstructure of the rGO/SnO_2 aerogels, combining the channel-like network of pores (macroporosity) with the cell wall mesoporosity, is promising. Specifically, the latter facilitates ion diffusion and enables the access to an increased number of intercalation and adsorption sites, while a homogenous distribution of the electrolyte throughout the electrode along the applied potential gradient is assured by the macroporosity.[49]

Mechanical performance of the rGO/SnO_2 aerogels

The aerogels need to be compressed, when implementing them in the battery cell as a free-standing cathode material. Mechanical testing of the aerogels is thereby conducted by means of compression, to assure their structural integrity upon cell assembly and electrochemical analysis. The density and microstructure of the aerogels, specifically the degree of ordering and the alignment of the rGO sheets, play thereby a crucial role, defining the mechanical response. To this end, the size of the rGO sheets contributes immensely to the elastic mechanical performance. Sheets larger than 20 µm provide structural recovery upon deformation and a strength one order of magnitude higher than those smaller than 2 µm.[38] However, the size of the sheets also influences the electrochemical performance, whereas for smaller edge-rich sheets an increased capacity in AIBs is obtained due to the additional intercalation sites at the edges.[50] Therefore, an optimal sheet size with sufficient mechanical stability and optimal electrochemical performance is crucial. The investigation of the rGO and rGO/SnO_2 aerogels (**Supporting Figure S8**), with an initial GO sheet size smaller than 2 µm, revealed a poor mechanical performance (**Supporting Figure S9**). Therefore, rGO and rGO/SnO_2 aerogels fabricated with a sheet size larger than 20 µm were investigated. Specifically, they would provide high elasticity and mechanical stability, similar to elastomeric materials, and yet sufficient edges for facilitated ion de-/intercalation. In particular, the continuous packing of the rGO within a cell wall and their interconnection promote their strength and superelasticity.[38]

The shape of the obtained compressive stress-strain curves of the aerogels, whether pristine or hybrid (**Figure 4a**), indicate four typical deformation stages of cellular materials.[51,52] Specifically, stage I (strain < 5 %) correlates to the elastic deformation, stage II (strain up to 50 %) to cell wall buckling and stage III (strain up to 75 %) to the densification of the aerogels.[53] Stage IV represents the recovery of the aerogels referring to the flexibility of the structure with the rGO sheets. The macroscopic deformation of the aerogels is displayed in **Figure 4b** through digital images representative of the different stages (**Supporting Movie S1** and **S2**). The elastic deformation of the aerogels is characterized by a Young's modulus similar for both aerogels, 0.41 ± 0.06 kPa for the pristine and 0.42 ± 0.09 kPa for the hybrid aerogel, with a slight increase in the compressive strength (**Supporting Table S1**). Considering that the presented aerogels exhibit a porosity of ~ 99,9 %, these values are in good agreement to those obtained for other graphene/graphene oxide aerogels.[53]

Notably, the rGO/SnO_2 aerogels show a superior recovery of 95.5 % compared to pristine rGO aerogels (53.3 %) (**Figure 4a** and **Supporting Movie S3**), allowing a reversible compression over a wide strain range with only a slight (3.5 %) permanent deformation (**Figure 4b**). The latter is ascribed to defects in the aerogels' cell walls, such as micro-cracks,[38] while the high recovery is attributed to the flexibility of the rGO sheets as well as the tailored structure-design, allowing significant energy absorption. The superior recovery of the hybrid aerogels is assumed to originate from the wrapping, or anchoring, of the SnO_2, which interconnects neighboring rGO sheets and interlock upon proceeding mechanical deformation. Such performance renders these hybrid aerogels as an ideal electrode material with a high mechanical stability, which maintains its flexibility and a certain porosity even under very high compression states. The accommodation of larger ions is thereby possible while the structural integrity of the electrodes is preserved.

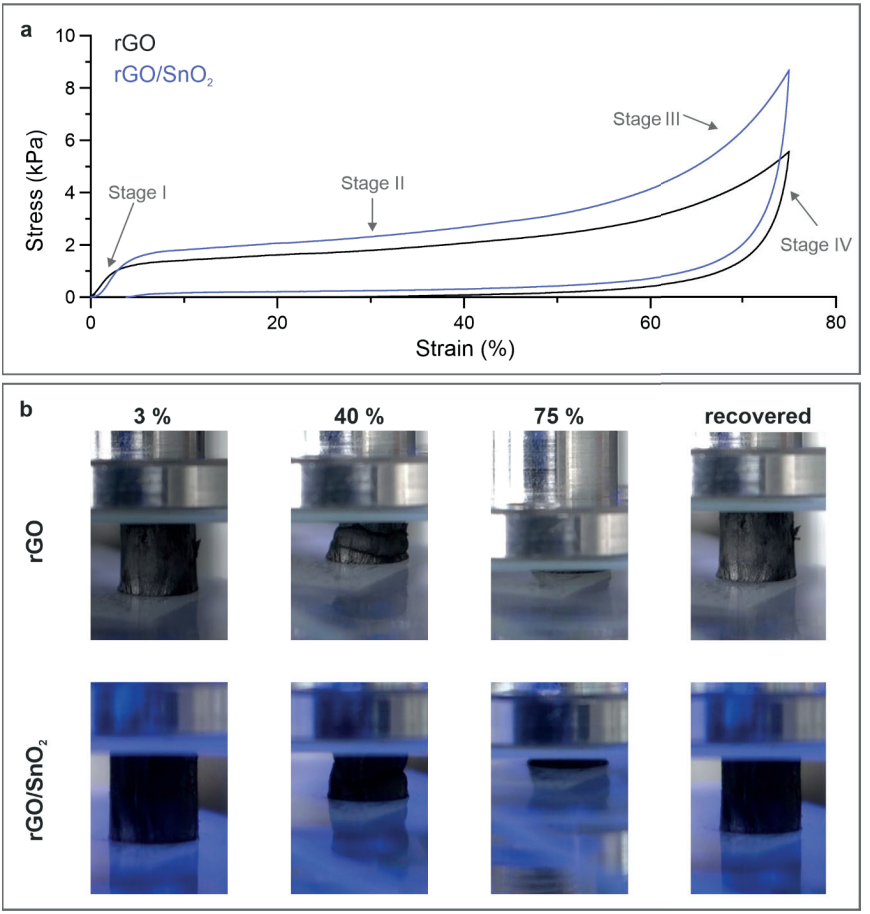

Figure 4. Mechanical performance of the rGO and rGO/SnO_2 aerogels under compression. (a) The compressive stress-strain curve with (b) the corresponding *in-situ* images of the different compression states.

Electrochemical performance of the rGO and rGO/SnO_2 aerogels

The ultra-light, free-standing and binder-free rGO and rGO/SnO_2 aerogels were electrochemically tested by directly soaking them with electrolyte and compressing them into discs upon cell assembly. The impact of additives used in conventional slurry-based electrodes on the electrochemical performance is thereby excluded, allowing to investigate the individual contribution of rGO and SnO_2 within the hybrid material. The electrodes were evaluated in the

voltage window between 0.2 V and 2.2 V vs Al/Al^{3+}. **Figure 5a** shows the corresponding cyclic voltammetry (CV) curves. For the pristine rGO aerogel, a plateau between 0.15 V and 1.7 V is observed.[54] This current-voltage behavior, where the current is predominantly linearly proportional to the voltage rate, is typical for non-Faradaic energy storage. In contrast, the hybrid rGO/SnO_2 electrode displays an anodic and a corresponding cathodic peak around 0.5 V (peak A), which is correlated to the de-/intercalation of Al^{3+} in SnO_2.[28] Upon intercalation of the Al^{3+} into the rutile crystal structure of SnO_2, the tetra-valent Sn(IV) is reduced to divalent Sn(II), resulting in Al_xSnO_2.[28] Whereat, the amount of intercalated Al^{3+} ions, denoted as x, reaches a maximum of 0.6. Interestingly, the CV curves of the hybrid electrode exhibits an additional anodic peak at 1.8 V and a corresponding cathodic peak at 1.3 V (peak B), not related to the intercalation into SnO_2. The origin of the peak is hypothesized to be the de/intercalation of $AlCl_4^-$ at the interface between the SnO_2 particles and the rGO sheets.

This hypothesis is supported by results obtained for a freeze-dried rGO/SnS_2 composite.[23] They observed a peak with a large shift between positive and negative scan direction at a similar intercalation voltage.

Owing to the high surface area of the tailored aerogel electrodes, a large electrochemical double layer is formed. A significant capacitive contribution is thereby achieved analogous to the pristine rGO electrode (**Figure 5a**). The energy storage process is therefore a combination of de-/intercalation of the ions into SnO_2 as well as between rGO/SnO_2 and their adsorption on the rGO surface. Hence an interplay between Faradaic and non-Faradaic processes occurs during the charging and discharging processes, utilizing the active material to its utmost.

In order to define the contribution of the diffusion-controlled processes, from that of the pseudo-capacitive effect to the overall energy storage, CV measurements with scan rates ranging from 0.1 mV s^{-1} up to 100 mV s^{-1} were conducted (**Figure 5b**). At scan rates, up to 10 mV s^{-1}, the current peaks shift with a noticeable increase in peak separation. Upon increasing the scan rate to 100 mV s^{-1}, however, the peaks are not detectable anymore and the energy storage process shifts to a mainly non-Faradaic characteristic.

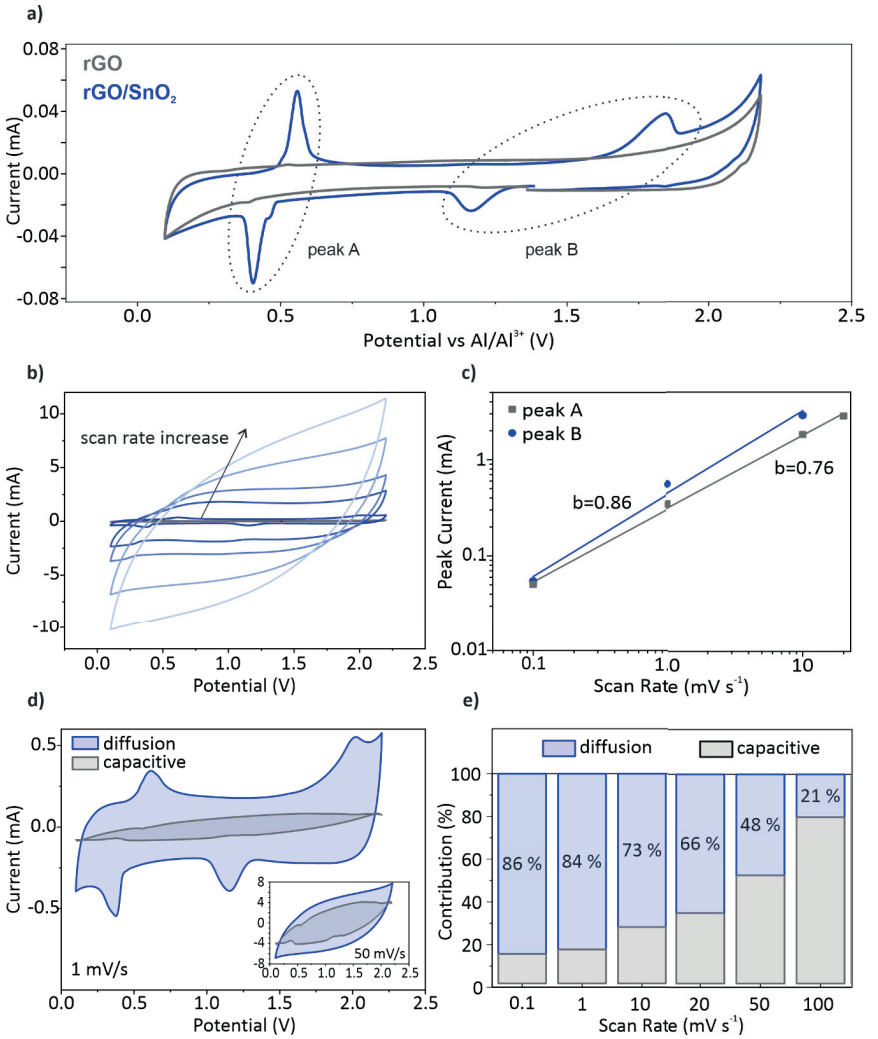

Figure 5. (a) Cyclic voltammograms (CV) of the rGO/SnO_2 hybrid electrode in comparison with the pristine rGO electrode at 0.1 mV s-1 (2nd cycle). (b) CVs at 0.1, 1, 10, 20, 50 and 100 mV s^{-1} for the rGO/SnO_2 hybrid electrode (2nd cycle). (c) Plot of the anodic peak current at the different scanning rates for b-value determination of peak A and peak B. (d) The contribution of the diffusion and capacitive controlled current response at 1 mV s^{-1} and 50 mV s^{-1} (inset). (e) The faradaic and non-faradaic contribution to the whole capacity (capacitive vs diffusion-controlled energy storage) of the rGO/SnO_2 composite for all scanning rates, ranging from 0.1 mV s^{-1} up to 100 mV s^{-1}.

By plotting the peak current against the scan rate in a double-logarithmic plot (**Figure 5c**), indication of the predominant process can be shown.[55] The slope b of the thereby obtained linear regression follows I = a νb, where I corresponds to the peak current, ν to the scanning rate and a to the y-intersect. Values for b approaching unity are characteristic for capacitance controlled processes, while values around 0.5 indicate diffusion-controlled processes.[56] The b-value is thereby determined to 0.76 for peak A and 0.86 for peak B, implying that both processes contribute. However, the higher value for peak B indicates a more capacitance-controlled process, denoting more surface-controlled kinetics. This additional peak arises therefore not only from intercalation of ions between SnO_2 and rGO, but mostly from their adsorption at the surface. To determine the contribution percentage of each process type, whether diffusion-controlled or surface-controlled, the corresponding current at different potential points is evaluated.[18] The cyclic voltammograms at 1 and 50 mV s^{-1} (**Figure 5d**) present the contribution of the different processes. A notable decrease of the capacitive current at the potential corresponding to the de-/intercalation processes, peak A and B, can be seen. Moreover, an increase of the capacitive contribution at the higher scan rate is apparent, comprising more than 50 % at 50 mV s^{-1}. The contribution of the diffusion and capacitive processes for the various scanning rates is shown in **Figure 5e**. That of capacitive ion adsorption onto the surface of the electrodes increases with the charging rates, as anticipated. Surprisingly, the contribution of diffusion-controlled processes is dominant at a scanning rate of up to 50 mV s^{-1}. This behavior unites the main properties of a capacitive-controlled supercapacitor and a diffusion-controlled battery, combining high power and energy densities. Compared to a recently published work about graphite-graphite dual ion batteries using the same electrolyte, the diffusion-controlled contribution for the hybrid aerogel at the same scanning rate of 1 mV s^{-1} is more than two-fold increased.[57] This significant increase results from the synergy of nanosized SnO_2 particles wrapped by rGO sheets and the tailored microstructure of the hybrid aerogel electrode. Due to the small size of the SnO_2 particles, de/intercalation is enabled at very high scanning rates of 100 mV s^{-1}, delivering a sizable contribution to the capacity (**Figure 5e**). The energy storage process is therefore optimized, exploiting simultaneously the large surface area of 221.3 m^2 g^{-1} induced by the tailored microstructure of the rGO-based aerogel electrode and the electrochemically active nanometer sized SnO_2 particles. The unidirectional channels, which originate from ice-templating, enable fast infiltration of electrolyte even at a compressed state. Additionally, they decrease the electron pathway and increase the high rate performance of the electrode.[58] This enables a supercapacitor-like performance at very high charging rates,

coupled with comparatively large capacity values, thus overcoming the limitation in either energy or power density, typically found in batteries or supercapacitors, respectively.

To further evaluate the rate performance of the hybrid aerogels in comparison to the pristine material, galvanostatic charge-discharge profiles with a charging rate of 2 C, 20 C and 40 C were conducted (**Figure 6**). A specific gravimetric capacity of the hybrid aerogel of 50 mAh g^{-1} was obtained for a current density of 100 mA g^{-1} (2 C). The impact of the SnO_2 nanoparticles addition on the electrochemical performance of the aerogels is concluded from the comparison of their volumetric capacities. The significant difference in gravimetric densities of the materials in question is thereby excluded.

From the charge-discharge profiles (**Figure 6a**) of the hybrid electrode a large plateau around 0.5 V is observed, which correlates to peak A (**Figure 5a**). By increasing the charging rate, the length of the plateau decreases, equivalent to our findings from the CV analysis. However, the less pronounced plateau, corresponding to peak B (**Figure 5a**), disappears at higher charging rates. Additionally, a pseudocapacitive behavior is observed for the hybrid electrode, analogous to the pristine electrode. These findings corroborate the results obtained from the cyclic voltammetry analysis, demonstrating the synergy of the energy storage processes present in the hybrid electrodes. The volumetric capacity delivered by the hybrid electrode is accordingly higher by 23 % than that of the pristine electrode. From the cell life investigation (**Figure 6b**), the same trend of the capacity evolution is observed for both electrodes. The increase of the capacities can therefore be attributed to the activation of the rGO and its subsequent reduction.[41] Furthermore, the initially high efficiency of 105 % supports this conclusion (**Supporting Figure S10**). Moreover, by increasing the charging rate lower capacities are attained, reaching a capacity of 16.1 mAh cm^{-3} at 2 C and only 8.9 and 6.4 mAh cm^{-3} at 20 and 40 C, respectively. Notably, the hybrid electrodes deliver higher volumetric capacities than the pristine rGO electrodes, over 30 % at the various charging rates. Compared to other cathode materials for AIBs the hybrid aerogel electrodes deliver adequate energy densities (20-50 Wh kg^{-1}) at notably high power densities (810-100 W kg^{-1}), as shown in the Ragone plot (**Supporting Figure S11**). On this basis, the benefit of the SnO_2 nanoparticle loading on the porous channel-like rGO aerogel is validated. Furthermore, the well-defined nanostructure of SnO_2 hinders the pulverization of the particles, leading to an excellent cycling stability over 10000 cycles.

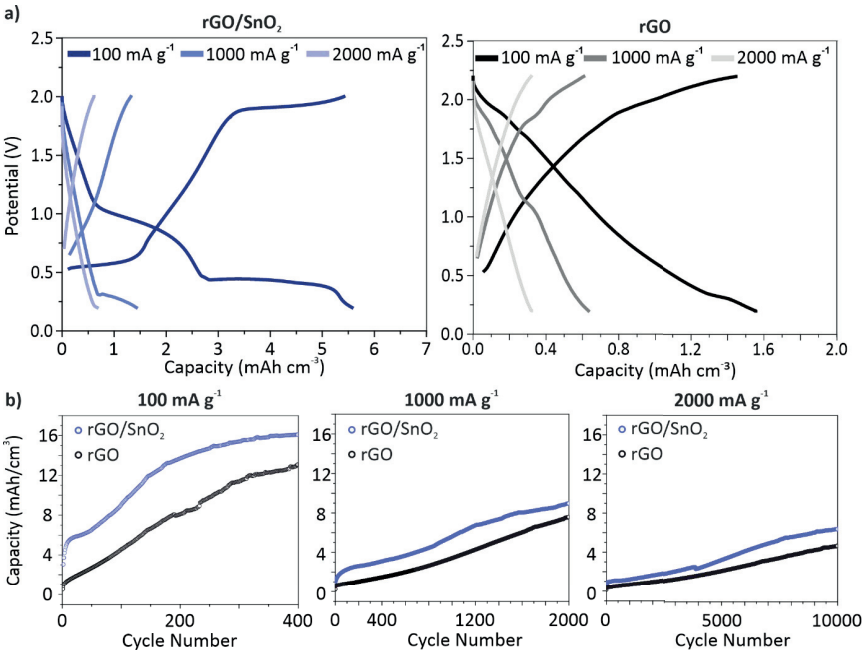

Figure 6. (a) Charge-discharge profiles of the hybrid rGO/SnO_2 (left) and pristine rGO (right) electrodes at the 10th cycle. (b) Rate performance of electrodes at a current density of 100, 1000 and 2000 mA g^{-1}. Their volumetric energy storage capacity was calculated for a compressed electrode with a thickness of 100 µm.

The here observed electrochemical performance of the hybrid electrodes can be attributed to three different energy storage mechanisms (**Figure 7**).

(i) The non-Faradaic contribution is partially correlated to the electrochemical double layer capacitance observed for rGO sheets with crystallite sizes below 10 nm.[16] The chloroaluminate anions are thereby adsorbed at the surface of rGO sheets.

(ii) Peak B is hypothesized to correlate to the intercalation of $AlCl_4^-$ between SnO_2 and rGO. The SnO_2 nanoparticles embedded in the rGO aerogel, provide sufficient space for intercalation, as they increase the cumulative pore volume fraction. When considering graphitic materials, intercalation involving $AlCl_4^-$ results in a characteristic peak around 2 V.[13,58] Additionally, the SnO_2 nanocrystals distort the graphitic structure, which could facilitate the intercalation and

thus lowers the voltage. This mechanism contributes further to the pseudocapacitive behavior of the hybrid aerogel electrode.

(iii) The Faradaic contribution entails the de/intercalation of Al^{3+} into SnO_2 (peak A), similarly observed for SnO_2/C cathodes.[28]

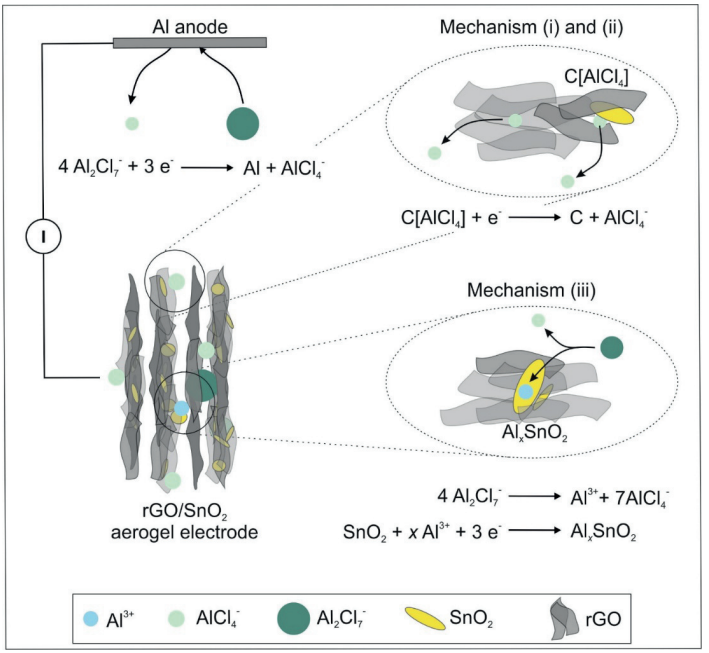

Figure 7. A schematic representation of the rGO/SnO_2 aerogel electrode in a half-cell configuration (left), where the three different energy storage mechanisms occurring at the cathode are presented with the corresponding simplified chemical reactions (right).

4.4 Conclusion

We fabricated a highly porous, free-standing rGO/SnO_2 aerogel as a binder-free cathode for AIBs. The tailored microstructure of these aerogels provides a synergy of mechanical stability and enhanced electrochemical performance. It is characterized by aligned channels, which walls comprise rGO sheets and embedded SnO_2 nanoparticles, resulting in high flexibility with a significant structural recovery upon mechanical compression, up to 95.5 %. Furthermore, the

here-achieved integration of nanosized SnO_2 particles into the rGO aerogel creates a synergistic effect, where pseudocapacitive and diffusion-controlled energy storage mechanisms contribute simultaneously to the deliverable capacity and prolong the battery life, over 10 000 cycles. An enhancement of the volumetric capacity by 23 % is thereby achieved, as opposed to its rGO aerogel counterpart. In addition, a notably high power density of 810 W kg^{-1} was achieved for the hybrid aerogels, comparable or superior to that of state of the art hybrid electrodes for AIBs. A step towards solving the current predicament in mobile energy devices is thereby made, as a combination of high power and high energy density, achievable by a single energy storage device, is attained. Our findings provide therefore new insights into the conceptual design of high-performance hybrid electrodes with pseudocapacitive behavior for AIBs.

4.5 Acknowledgments

We highly appreciate the financial and technical support from Prof. J. Spatz and his group from the Max Planck Institute for Medical Research, Gerd Maier performed XRD measurements, whereas Erik Farley and Wenzel Gassner supported with SEM measurements. Maximilian Hackner assisted in TGA investigations and Traugott Wörner aided in the construction of the ice-templating setup. The BET measurements were performed by Sebastian Emmerling from the Department of B. Lotsch at Max Planck Institute for Solid State Research in Stuttgart.

4.6 References

1. Y.Lu, Q. Zhang, L. Li, Z. Niu, J. Chen, *Chem* 2018, 4, 2786

2. Luo, W.; Shen, F.; Bommier, C.; Zhu, H.; Ji, X.; Hu, L. Na; *Acc. Chem. Res.* 2016, *49*, 231–240,

3. Valma, C.; Buchholz, D.; Passerini, S.; *Current Opinion in Electrochemistry* 2018, *9*, 41–48,

4. Li, M.; Lu, J.; Ji, X.; Li, Y.; Shao, Y.; Chen, Z.; Zhong, C.; Amine, K.; *Nature Reviews Materials* 2020, *5*, 276–294

5. Cui, L.; Zhou, L.; Kang, Y.-M.; An, Q.; *ChemSusChem* 2020, *13*, 1071–1092

6. S. K. Das, S. Mahapatra, H. Lahan, *Journal of Materials Chemistry A* 2017, 5, 6347.

7. S. K. Das, *Angewandte Chemie International Edition* 2018, 57, 16606.

8. G. A. Elia, K. Marquardt, K. Hoeppner, S. Fantini, R. Lin, E. Knipping, W. Peters, J.-F. Drillet, S. Passerini, R. Hahn, *Advanced Materials* 2016, 28, 7564.

9. T. Leisegang, F. Meutzner, M. Zschornak, W. Münchgesang, R. Schmid, T. Nestler, R. A. Eremin, A. A. Kabanov, V. A. Blatov, D. C. Meyer, *Front. Chem*. 2019, 7.

10. H. Yang, H. Li, J. Li, Z. Sun, K. He, H.-M. Cheng, F. Li, *Angewandte Chemie* 2019, 131, 12104.

11. M. Armand, F. Endres, D. R. MacFarlane, H. Ohno, B. Scrosati, *Nature Mater* 2009, 8, 621.

12. X. Zhang, S. Jiao, J. Tu, W.-L. Song, X. Xiao, S. Li, M. Wang, H. Lei, D. Tian, H. Chen, D. Fang, *Energy & Environmental Science* 2019, 12, 1918.

13. M.-C. Lin, M. Gong, B. Lu, Y. Wu, D.-Y. Wang, M. Guan, M. Angell, C. Chen, J. Yang, B.-J. Hwang, H. Dai, *Nature* 2015, 520, 324.

14. Y. Wu, N. Yi, L. Huang, T. Zhang, S. Fang, H. Chang, N. Li, J. Oh, J. A. Lee, M. Kozlov, A. C. Chipara, H. Terrones, P. Xiao, G. Long, Y. Huang, F. Zhang, L. Zhang, X. Lepró, C. Haines, M. D. Lima, N. P. Lopez, L. P. Rajukumar, A. L. Elias, S. Feng, S. J. Kim, N. T. Narayanan, P. M. Ajayan, M. Terrones, A. Aliev, P. Chu, Z. Zhang, R. H. Baughman, Y. Chen, *Nat Commun* 2015, 6, 1.

15. H. Chen, F. Guo, Y. Liu, T. Huang, B. Zheng, N. Ananth, Z. Xu, W. Gao, C. Gao, *Advanced Materials* 2017, 29, 1605958.

16. J. Smajic, A. Alazmi, N. Batra, T. Palanisamy, D. H. Anjum, P. M. F. J. Costa, *Small* 2018, 14, 1870251.

17. Y. Wu, M. Gong, M.-C. Lin, C. Yuan, M. Angell, L. Huang, D.-Y. Wang, X. Zhang, J. Yang, B.-J. Hwang, H. Dai, *Advanced Materials* 2016, 28, 9218.

18. V. Augustyn, P. Simon, B. Dunn, *Energy Environ. Sci.* 2014, 7, 1597.

19. K. Zhang, T. H. Lee, J. H. Cha, H. W. Jang, M. Shokouhimehr, J.-W. Choi, *Electron. Mater. Lett.* 2019, 15, 720.

20. T. Gao, X. Li, X. Wang, J. Hu, F. Han, X. Fan, L. Suo, A. J. Pearse, S. B. Lee, G. W. Rubloff, K. J. Gaskell, M. Noked, C. Wang, *Angewandte Chemie International Edition* 2016, 55, 9898.

21. S. Wang, S. Jiao, J. Wang, H.-S. Chen, D. Tian, H. Lei, D.-N. Fang, *ACS Nano* 2017, 11, 469.

22. X. Zhang, S. Wang, J. Tu, G. Zhang, S. Li, D. Tian, S. Jiao, *ChemSusChem* 2018, 11, 709.

23. Y. Hu, B. Luo, D. Ye, X. Zhu, M. Lyu, L. Wang, *Advanced Materials* 2017, 29, 1606132.

24. S. Wang, Z. Yu, J. Tu, J. Wang, D. Tian, Y. Liu, S. Jiao, *Advanced Energy Materials* 2016, 6, 1600137.

25. G. Cohn, L. Ma, L. A. Archer, *Journal of Power Sources* 2015, 283, 416.

26. X. Zhang, G. Zhang, S. Wang, S. Li, S. Jiao, *J. Mater. Chem. A* 2018, 6, 3084.

27. H. Wang, Y. Bai, S. Chen, X. Luo, C. Wu, F. Wu, J. Lu, K. Amine, *ACS Appl. Mater. Interfaces* 2015, 7, 80.

28. H. Lu, Y. Wan, T. Wang, R. Jin, P. Ding, R. Wang, Y. Wang, C. Teng, L. Li, X. Wang, D. Zhou, G. Xue, *J. Mater. Chem. A* 2019, 7, 7213.

29. T. Yamazaki, U. Mizutani, Y. Iwama, Jpn. *J. Appl. Phys.* 1983, 22, 454.

30. C.G. Fonstad, R.H. Rediker, *Journal of Applied Physics,* 1971 Vol 42, No 7.

31. Jahnke, T.; Knöller, A.; Kilper, S.; Rothenstein, D.; Widenmeyer, M.; Burghard, Z.; Bill, J.; *ACS Appl. Energy Mater.* 2018, *1*, 7085–7092

32. Kwon, O.H.; Oh, J.H.; Gu, B.; Jo, M.S.; Oh, S.H.; Kang, Y.C.; Kim, J.-K.; Jeong, S.M.; Cho, J.S, *Advanced Science* 2020, *7*, 2070093,

33. Cho, J.S.; Kang, Y.C.; *Small* 2015, *11*, 4673–4681, doi:10.1002/smll.201500940.

34. Preparation of Graphitic Oxide | *Journal of the American Chemical Society*.1958

35. C. Wang, G. Du, K. Ståhl, H. Huang, Y. Zhong, J. Z. Jiang, *J. Phys. Chem. C* 2012, 116, 4000.

36. Freezing as a Path to Build Complex Composites | *Science* 2006, Vol. 311, 5760, pp. 515 - 518.

37. S. Deville, In Freezing Colloids: Observations, Principles, Control, and Use: Applications in Materials Science, Life Science, Earth Science, Food Science, and Engineering; Deville, S., Ed.; *Engineering Materials and Processes*; Springer International Publishing: Cham, 2017; pp. 351–438.

38. N. Ni, S. Barg, E. Garcia-Tunon, F. M. Perez, M. Miranda, C. Lu, C. Mattevi, E. Saiz, *Sci Rep* 2015, 5, 1.

39. C. Zhu, T. Y.-J. Han, E. B. Duoss, A. M. Golobic, J. D. Kuntz, C. M. Spadaccini, M. A. Worsley, *Nat Commun* 2015, 6, 1.

40. A. Nieto, B. Boesl, A. Agarwal, *Carbon* 2015, 85, 299.

41. M. Acik, G. Lee, C. Mattevi, A. Pirkle, R. M. Wallace, M. Chhowalla, K. Cho, Y. Chabal, *J. Phys. Chem. C* 2011, 115, 19761.

42. Y. Chen, K. Fu, S. Zhu, W. Luo, Y. Wang, Y. Li, E. Hitz, Y. Yao, J. Dai, J. Wan, V. A. Danner, T. Li, L. Hu, *Nano Lett.* 2016, 16, 3616.

43. M. Acik, Y. J. Chabal, *JMSR* 2012, 2, p101.

44. N. Wiberg, A. F. Holleman, E. Wiberg, G. Fischer, Lehrbuch der Anorganischen Chemie; 102., stark umgearb. u. verb.; De Gruyter: Berlin New York, 2007.

45. Binding SnO_2 Nanocrystals in Nitrogen-Doped Graphene Sheets as Anode Materials for Lithium-Ion Batteries - Zhou - - *Advanced Materials*, 2013.

46. L. Noerochim, J.-Z. Wang, S.-L. Chou, D. Wexler, H.-K. Liu, Carbon 2012, 50, 1289.

47. S. M. Hwang, Y.-G. Lim, J.-G. Kim, Y.-U. Heo, J. H. Lim, Y. Yamauchi, M.-S. Park, Y.-J. Kim, S. X. Dou, J. H. Kim, *Nano Energy* 2014, 10, 53.

48. P. Schneider, *Applied Catalysis A: General* 1995, 129, 157.

49. Y. Hu, B. Luo, D. Ye, X. Zhu, M. Lyu, L. Wang, *Advanced Materials* 2017, 29, 1606132.

50. Q. Zhang, L. Wang, J. Wang, C. Xing, J. Ge, L. Fan, Z. Liu, X. Lu, M. Wu, X. Yu, H. Zhang, B. Lu, *Energy Storage Materials* 2018, 15, 361.

51. A. Knöller, S. Kilper, A. M. Diem, M. Widenmeyer, T. Runčevski, R. E. Dinnebier, J. Bill, Z. Burghard, *Nano Lett.* 2018, 18, 2519.

52. F. Ashby, R. F. M. Medalist, MTA 1983, 14, 1755.

53. L. Qiu, B. Huang, Z. He, Y. Wang, Z. Tian, J. Z. Liu, K. Wang, J. Song, T. R. Gengenbach, D. Li, *Advanced Materials* 2017, 29, 1701553.

54. H. Jiao, J. Wang, J. Tu, H. Lei, S. Jiao, *Energy Technology* 2016, 4, 1112.

55. V. Raju, J. Rains, C. Gates, W. Luo, X. Wang, W. F. Stickle, G. D. Stucky, X. Ji, *Nano Lett.* 2014, 14, 4119.

56. C. Chen, Y. Wen, X. Hu, X. Ji, M. Yan, L. Mai, P. Hu, B. Shan, Y. Huang, *Nat Commun* 2015, 6, 1.

57. Z. Li, J. Liu, B. Niu, J. Li, F. Kang, *Small* 2018, 14, 1800745.

58. Z. Zhao, M. Sun, W. Chen, Y. Liu, L. Zhang, N. Dongfang, Y. Ruan, J. Zhang, P. Wang, L. Dong, Y. Xia, H. Lu, *Advanced Functional Materials* 2019, 29, 1809196.

4.7 Supplementary Materials

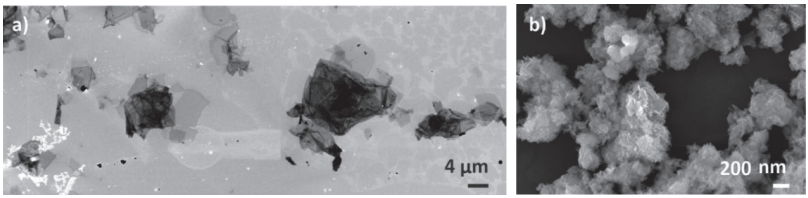

Figure S1. SEM images of (a) a GO sheet, prepared by the modified Hummers Method (size between 2 to 20 µm). (b) SnO_2 nanoplatelets, prepared by a hydrothermal approach.

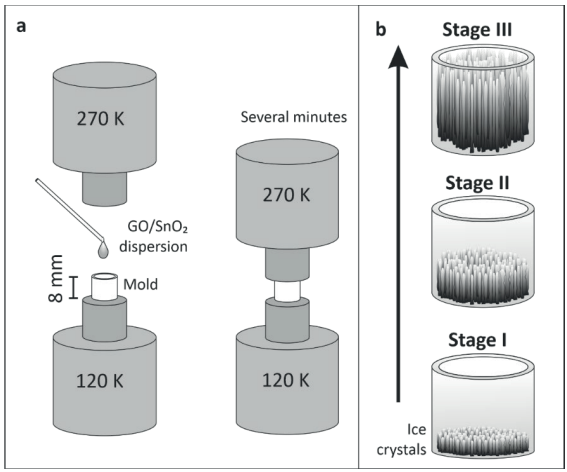

Figure S2. Schematic illustration of the (a) ice-templating setup and (b) the evolution of unidirectional ice crystal growth.

Ice-templating

In general, applying this technique enables the fabrication of highly porous, mechanically stable aerogels. When using the self-build setup schematically displayed in **Supporting Figure S2a**, the ice-templating process can be precisely controlled. The two copper cold fingers at the top and bottom of the mold are cooled with liquid nitrogen. As the cold fingers are equipped with heating rings, the temperature of each cold finger can be individually set, enabling the precise control over the temperature gradient in-between. A PTFE mold is placed between the cold fingers, allowing to fabricate cylindrical aerogels with a height and diameter of eight mm. When the desired temperature gradient is set, the dispersion can be filled into the mold and the upper cold finger will be lowered onto the mold.

The ice-templating process itself is schematically depicted in **Supporting Figure S2b**, where a freezing gradient of 150 K between both cold fingers induces a fast-unidirectional crystal growth, as soon as the liquid comes into contact with the cooled cold finger, (Stage I). Hereby, the ice crystals nucleate and grow along the gradient, whilst the solid dispersed material is expelled at the ice crystal interface. Due to the large gradient, the ice front is moving from the bottom to the top of the mold, yielding columnar ice crystals as a result. Such columns aligned along the freezing direction mechanically support the aerogel, which results in an increased Young's modulus, compared with foam frozen by different methods.[1] Upon further solidification (Stage II), the initial temperature gradient decreases, promoting the ice crystal growth perpendicular to the temperature gradient. In this stage the solid load between the ice crystals becomes compacted. Finally, in Stage III, the mold is completely frozen, ice crystals have grown to the top of the mold.

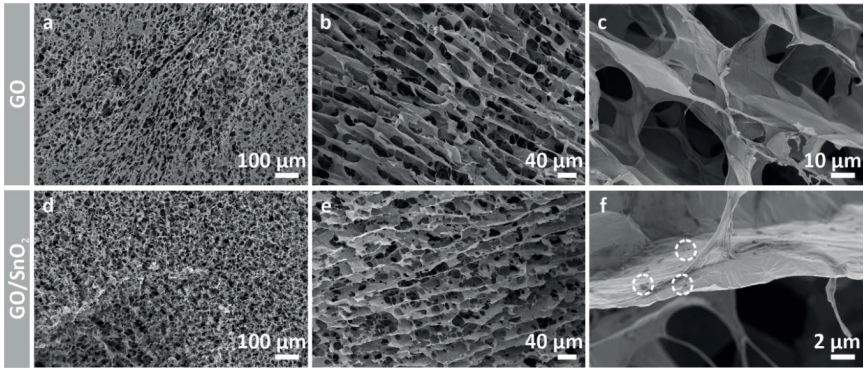

Figure S3. SEM images of the microstructures of GO and GO/SnO_2 aerogels (a,d) top view and (b,e) side view of the channels. Detailed view of the (c) GO walls and (f) the SnO_2 nanoplatelets embedded in the walls.

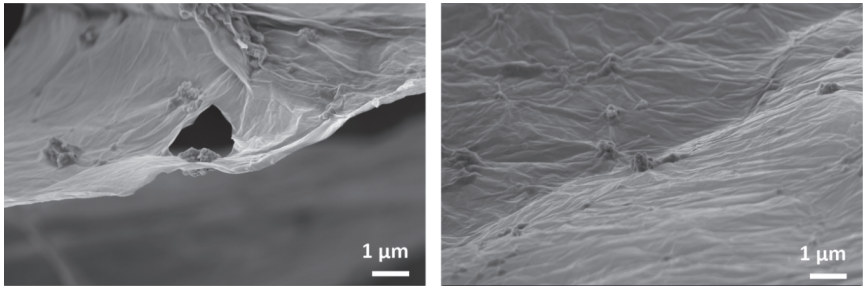

Figure S4. Highly magnified SEM images of the (a) GO/SnO_2 and (b) rGO/SnO_2 hybrid aerogel. In both cases, the sheets wrap the SnO_2 nanoplatelets and hold them in place.

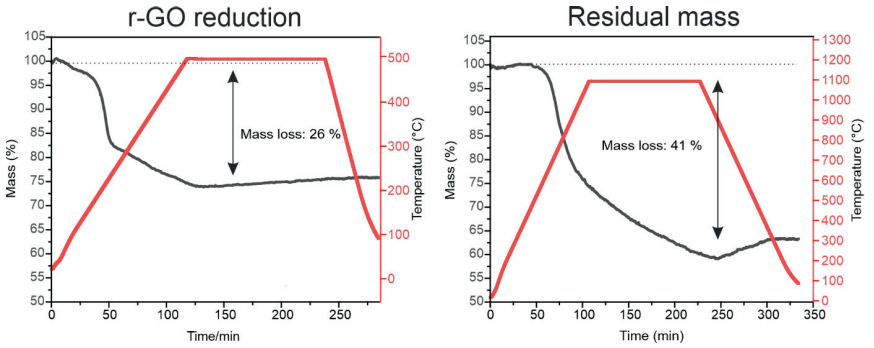

Figure S5. Thermogravimetric analysis of the annealing process at 500 °C in argon and its corresponding mass loss of 26 % and the determination of the rGO to SnO_2 ratio in synthetic air at 1100 °C, showing that 41 wt.% of the composite is comprised of rGO, whereas 59 wt.% is comprised of SnO_2.

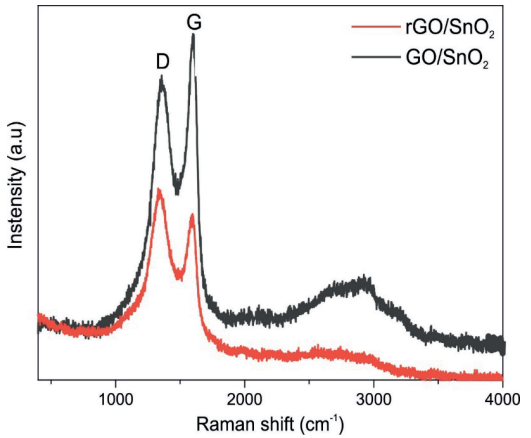

Figure S6. Raman Spectra of GO/SnO_2 (grey) and rGO/SnO_2 (red) samples, where the D- and G-bands are visible.

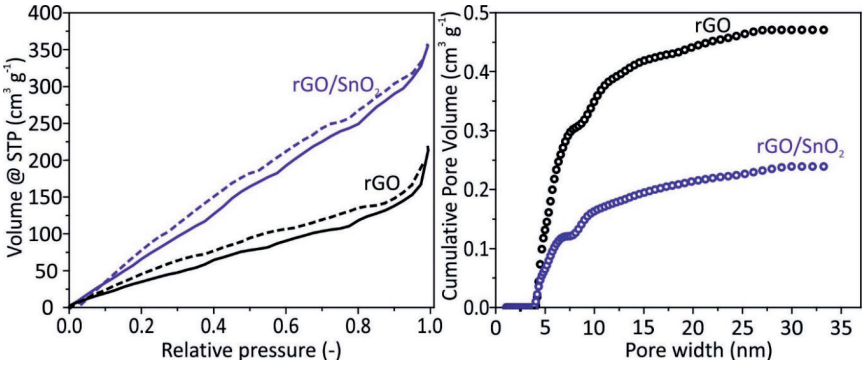

Figure S7. Isotherm obtained by N_2 adsorption and desorption curves of rGO and rGO/SnO_2 aerogels and their respective cumulative pore volume.

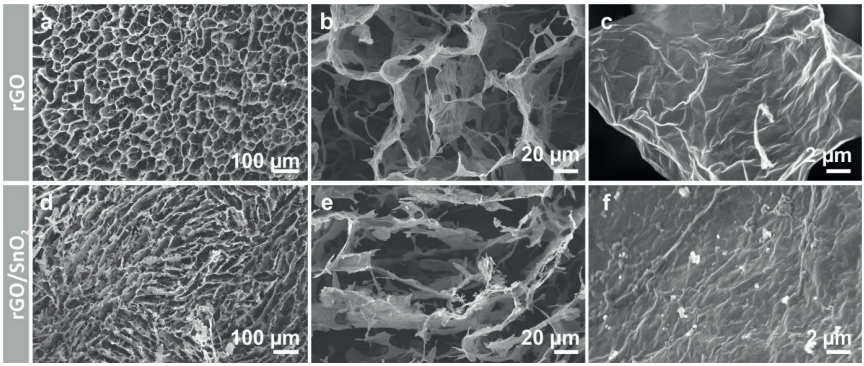

Figure S8. SEM images of the microstructures of rGO and rGO/SnO_2 aerogels, which were fabricated using a GO dispersion with much smaller sheet sizes. (a,d) Top view and (b,e) side view of the channels. Detailed view of the (c) GO walls and (f) the SnO_2 nanoplatelets embedded in the walls.

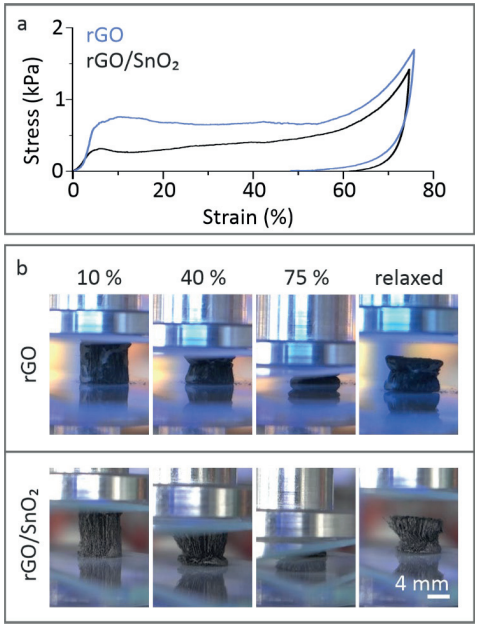

Figure S9. Mechanical performance of the rGO and rGO/SnO_2 aerogels, which were fabricated using a GO dispersion with smaller sheet sizes (< 2 µm), under compression. (a) The compressive stress-strain curve with (b) the corresponding *in-situ* images of the different compression states.

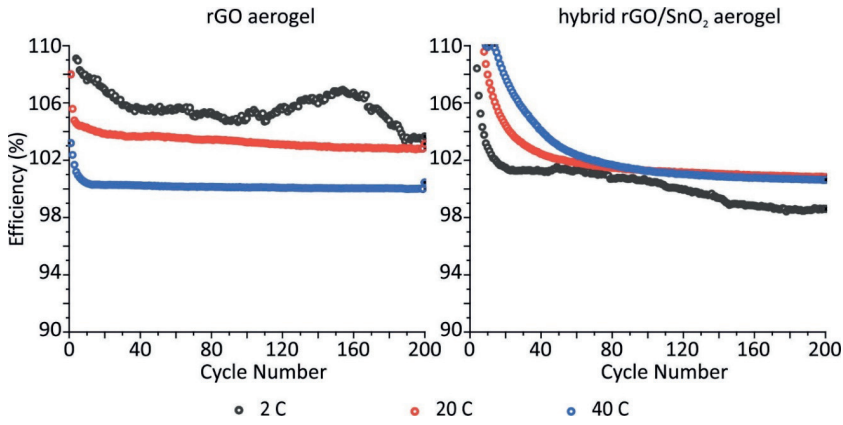

Figure S10. Efficiency plot of both the pristine and the hybrid aerogel.

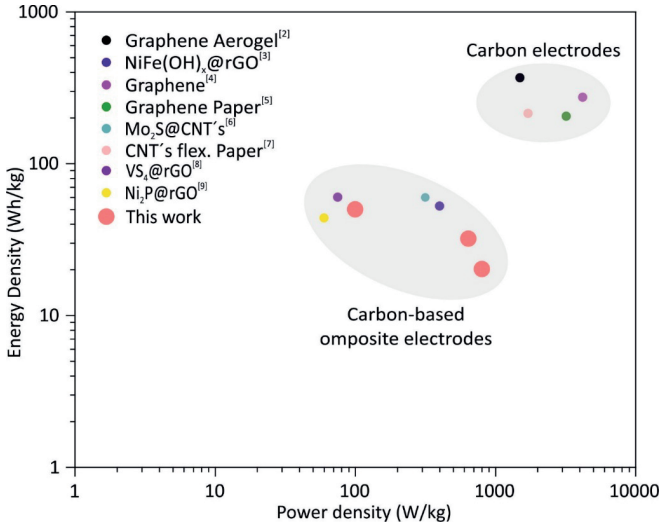

Figure S11. Ragone plot of the hybrid rGO/SnO_2 aerogel in comparison to the most recent literature in the field of AIB's.[2-9]

Supporting Table S1: Mechanical properties of rGO and rGO/SnO_2 aerogels.

	Young's modulus [kPa]	Compressive strength [kPa]	Recovery [%]
rGO	0.41 ± 0.06	1.39 ± 0.19	53.3
rGO/SnO_2	0.42 ± 0.09	1.55 ± 0.13	95.5

Supporting Table S2: Mechanical properties of rGO and rGO/SnO_2 aerogels, which were fabricated using a GO dispersion with much smaller sheet sizes (see also **Supporting Figure S1 b**).

	Young's modulus [kPa]	Compressive strength [kPa]	Recovery [%]
rGO	0.26 ± 0.14	1.06 ± 0.35	36
rGO/SnO_2	0.08 ± 0.03	0.31 ± 0.03	20

References

1. Z. Zhao, M. Sun, W. Chen, Y. Liu, L. Zhang, N. Dongfang, Y. Ruan, J. Zhang, P. Wang, L. Dong, Y. Xia, H. Lu, *Advanced Functional Materials* 2019, 29, 1809196.

2. H. Huang, F. Zhou, X. Shi, J. Qin, Z. Zhang, X. Bao, Z.-S. Wu, *Energy Storage Materials* 2019, 23, 664.

3. Y. Du, S. Zhao, C. Xu, W. Zhang, P. Li, H. Jin, Y. Zhang, Z. Wang, J. Zhang, *Energy Technology* 2019, 7, 1900649.

4. A. Ejigu, L. W. Le Fevre, K. Fujisawa, M. Terrones, A. J. Forsyth, R. A. W. Dryfe, ACS *Applied Material Interfaces* 2019, 11, 23261.

5. Q. Zhang, L. Wang, J. Wang, C. Xing, J. Ge, L. Fan, Z. Liu, X. Lu, M. Wu, X. Yu, H. Zhang, B. Lu, *Energy Storage Materials* 2018, 15, 361.

6. W. Yang, H. Lu, Y. Cao, B. Xu, Y. Deng, W. Cai, *ACS Sustainable Chemistry & Engineering* 2019, 7, 4861.

7. Y. Hu, S. Debnath, H. Hu, B. Luo, X. Zhu, S. Wang, M. Hankel, D. J. Searles, L. Wang, *Journal of Materials Chemistry A* 2019, 7, 15123.

8. X. Zhang, S. Wang, J. Tu, G. Zhang, S. Li, D. Tian, S. Jiao, *ChemSusChem* 2018, 11, 709.

9. J. Tu, M. Wang, X. Xiao, H. Lei, S. Jiao, *ACS Sustainable Chemistry & Engineering* 2019, 7, 6004.

Summary

The arising demand for mobile electronic devices requires the development of novel types of metal ion batteries, in which the electrodes have a high electrochemical storage capacity, high power density as well as a long cycle life. In order to achieve such battery performance, 4 major tasks were addressed in this thesis:

(i) Choosing and synthesizing suitable active materials, including their particle size and morphology, which renders the maximum uptake of metal ions and influences their intercalation as well as the compensation of the corresponding volume expansion. Here, tin oxide particles were synthesized in a hydrothermal approach, whereat different phases and morphologies could be achieved, depending on the used protocol. In addition, graphene oxide, which was fabricated by a modified Hummers method, was used as precursor for graphene/ SnO_2 hybrid electrodes. The oxygen-containing species promote the electrode fabrication, while a thermal post-treatment significantly increases the electrical conductivity of the material.

(ii) Combining the developed materials tin oxide and graphene oxide (or polyvinylpyrrolidone for proof-of-concept) in a bioinspired hierarchical fashion, yielding superior mechanical stability, similar to what is found in nature. Here, the choice of the assembling process allowed the tailoring of the microstructure. Using a facile drying process, predominantly dense layered paper-like materials can be obtained, resembling the microstructure of nacre. In contrast, co-assembling the materials *via* ice-templating results in highly porous sponges, similar to *Clathrina Clathrus.*

(iii) Thermally post-treating the obtained hybrid materials to achieve high electrical conductivity. Here, alongside the thermal reduction of graphene oxide, the released oxygen could be taken up by the co-assembled tin oxide phase, fully oxidizing it and anchoring it onto the reduced graphene oxide sheets. Such coalescence is crucial for ensuring good cycling stability and that both active materials partake in the electrochemical process.

(iv) Testing the resulting hybrid electrode material in metal ion batteries. Here, lithium ion- and aluminum ion batteries were investigated. In the first battery type, the electrode material functioned as anode, while in the latter, the hybrid material was used as cathode. In both cases the electrodes showed a promising electrochemical performance. Moreover, depending on the microstructure, additional effects, such as pseudocapacity, could be unlocked.

Zusammenfassung

Der steigende Bedarf an mobilen elektronischen Geräten erfordert die Entwicklung neuartiger Metallionenbatterien, bei denen die Elektroden eine hohe elektrochemische Speicherkapazität, eine hohe Leistungsdichte sowie eine lange Zyklenstabilität aufweisen. Um eine solche Batterieleistung zu erreichen, wurden in dieser Thesis 4 Aspekte der Elektrode verbessert:

(i) Auswahl und Synthese geeigneter Aktivmaterialien, einschließlich deren Partikelgröße und Morphologie, welche die maximale Einlagerung von Metallionen verbessern und die damit einhergehende Volumenausdehnung kompensiert. Hier wurden Zinnoxidpartikel in einem hydrothermalen Ansatz synthetisiert, wobei je nach verwendetem Protokoll unterschiedliche Phasen und Morphologien erreicht werden konnten. Darüber hinaus wurde Graphenoxid, welches durch eine modifizierte Hummers-Methode hergestellt wurde, als Präkursor für Graphen/SnO_2-Hybridelektroden verwendet. Die sauerstoffhaltigen funktionellen Gruppen des Graphenoxids fördern die Elektrodenherstellung, wobei gleichzeitig durch die thermische Nachbehandlung die elektrische Leitfähigkeit des Materials deutlich erhöht wurde.

(ii) Kombination der entwickelten Materialien Zinnoxid und Graphenoxid (auch Polyvinylpyrrolidon) in einer bioinspirierten hierarchischen Struktur, die, ähnlich wie in der Natur, eine überlegene mechanische Stabilität ergibt. Hier gestattete die Wahl des Assemblierungsprozesses die Anpassung der Mikrostruktur. Durch einen einfachen Trocknungsprozess können überwiegend dichte, geschichtete, papierartige Materialien erhalten werden, die an die Mikrostruktur von Perlmutt erinnern. Im Gegensatz dazu führt das Co-Assemblieren der Materialien über „ice-templating“ zu hochporösen Schwämmen, ähnlich z.B. *Clathrina Clathrus*.

(iii) Thermische Nachbehandlung der erhaltenen Hybridmaterialien, um eine hohe elektrische Leitfähigkeit zu erreichen. Hier konnte neben der thermischen Reduktion des Graphenoxids der freigesetzte Sauerstoff von dem koaggregierten Zinnoxidpräkursor aufgenommen, vollständig oxidiert und an den reduzierten Graphenoxidschichten verankert werden. Eine solche mechanische Verankerung ist entscheidend, um sicherzustellen, dass beide aktiven Materialien am elektrochemischen Prozess teilnehmen und eine gute Zyklenstabilität aufweisen.

(iv) Testen des resultierenden Hybridelektrodenmaterials in Metallionenbatterien. Hier wurden Lithium-Ionen- und Aluminium-Ionen-Batterien untersucht. Im ersten Batterietyp fungierte das Elektrodenmaterial als Anode, während im zweiten Typ das Hybridmaterial als Kathode verwendet wurde. In beiden Fällen zeigten die Elektroden eine vielversprechende elektrochemische Leistung.

Darüber hinaus konnten je nach Mikrostruktur zusätzliche Effekte, wie z. B. die Pseudokapazität, erschlossen werden.

Danksagung

An dieser Stelle möchte ich mich bei allen bedanken, dich mich während der Arbeit unterstützt haben. Mein Dank gilt zunächst einmal Herrn Prof. Dr. Bill als meinem Doktorvater, der mir die Möglichkeit gab, diese Arbeit in seiner Gruppe anzufertigen, die Zeit und Geduld die er meiner Arbeit widmete und mit dem ich viele Stunden zusammen Übungen, Praktika und Vorlesungen vorbereitet und besprochen habe. Herrn Prof. Dr. Schmauder danke ich für freundliche Übernahme des Mitberichts und Herrn Prof. Dr. Schleid für die Übernahme des Prüfungsvorsitzes.

Mein größter Dank geht an Frau Dr. Zaklina Burghard, meine Betreuerin. Wir verbrachten lange Stunden der fruchtbaren wissenschaftlichen Diskussion miteinander und ihre unermüdliche Unterstützung und Glauben an mich, ermöglichte erst die Fertigstellung dieser Arbeit. Sie unterstütze mich nicht nur bei Projektanträgen an die Vector GmbH und trug meine durchaus ausgefallenen Ideen mit, sondern passte auch mal auf meinen Sohn Alexander auf. Darüber hinaus stellte sie auch den Kontakt zu Prof. Dr. Spatz her, der unentgeltlich in großen Umfang Equipment und die technische Expertise seiner Abteilung zur Verfügung stellte.

An dieser Stelle möchte ich natürlich auch meiner Bürokollegin Dr. Andrea Knöller bedanken, für die mehr oder weniger freiwillige Aufgabe von allem Essbarem im Büro, ihre wissenschaftliche Unterstützung und fantastische Konferenzen. Hier will ich auch Leila Raafat, Dr. Achim Diem, Maximilian Hackner, Cora Bubeck und Dr. Stefan Kilper danken, mit denen ich bei geselligem Beisammensein meine Batterien wieder aufladen konnte und die mich alle tatkräftig mit Korrekturen und technischer Hilfe unterstützten. Wobei ich zusätzlich auf wissenschaftlicher Ebene die Ehre und das Vergnügen hatte, mit Stefan Kilper ein Projekt bei der Vector GmbH zu leiten und unsere wissenschaftlichen Mitarbeiter Kevin Hildenbrand, Alexandros Georgiadis, Jonathan Link, Vera Grohe, Tamara Krauss und Katharina Wiegers zu betreuen. In diesem Bunde möchte ich auch Daniel Hotz danken, der durch seine Gelassenheit, unermüdliche Unterstützung und seine starke Rückhand mich weitergebracht hat.

Unter meinen Kollegen sollen auch alle anderen, besonders Dr. Dirk Rothenstein, Dr. Petia Atanasova, Dr. Giulia Santomauro und die komplette Arbeitsgruppe Bill für die vielen wissenschaftlichen Gespräche, Ideen und Diskussionen nicht unerwähnt bleiben. Im Besonderen möchte in an dieser Stelle nochmals Leila Raafat danken, die mit sicherer Hand und

absoluter Souveränität die Lehre an dem Lehrstuhl übernommen und auf ein neues Niveau gehoben hat.

Des Weiteren bedanke ich mich für die Unterstützung durch die MPI-FKF und MPI-IS Infrastruktur, besonders bei der chemischen Analyse von Samir Hammoud, XPS Messung von Peter Schützendübel und Unterstützung am REM von Maritta Dudek und Hilda David.

Zu guter Letzt gebührt mein Dank an dieser Stelle auch meiner Familie, besonders Agnese mit unseren Kindern Alexander und Isabel, die alle große Geduld mit mir und der Erstellung dieser Arbeit bewiesen.